12-2022

X-Ray Interrogated Implantable Chemical and Strain Sensors for Monitoring Implant Associated Infections And Fracture Healing

Apeksha Rajamanthrilage
apekshr@g.clemson.edu

X-RAY INTERROGATED IMPLANTABLE CHEMICAL AND STRAIN SENSORS FOR MONITORING IMPLANT ASSOCIATED INFECTIONS AND FRACTURE HEALING

A Dissertation
Presented to
the Graduate School of
Clemson University

In Partial Fulfillment
of the Requirements for the Degree
Doctor of Philosophy
Chemistry

---

by
Apeksha C. Rajamanthrilage
December 2022

Accepted by:
Professor Jeffrey N. Anker, Committee Chair
Professor Joseph Kolis
Professor John Desjardins
Professor George Chumanov
Professor Tzuen-Rong Jeremy Tzeng

ABSTRACT

Bone fracture healing includes complex and sequence of dynamic events to restore the integrity and biomechanical properties of the bone. While most of the fractures heal without any problem, healing is sometimes compromised. Two significant fracture healing complications are orthopedic implant-associated infections and non-unions/delayed union. These can be interrelated causes as well. Implant-associated infection can cause implant loosening, and as a result, it can delay the fracture healing process. Herein, we describe two different types of sensors that can be used in monitoring biochemical and biomechanical processes of fracture healing using X-rays.

We developed a XELCI (X-ray Excited Luminescence Chemical Imaging) based biochemical sensor for monitoring implant-associated infections by decreasing pH due to acidic products of bacterial metabolism. High spatial resolution pH mapping of the intramedullary canal through bone and tissue was carried out with the XELCI imaging technique developed in our lab. Pre-pilot rabbit studies were carried out to monitor the pH variations in the intramedullary canal of the rabbit tibia by creating two infected rabbit models compared to a sterile control rabbit. We observed a pH drop in the intramedullary canal while using the pH-sensitive hydrogel-coated intramedullary rod.

Moreover, to monitor stiffness and biomechanical properties of the healing bone during fracture healing, we developed a biomechanical sensor with hydromechanical amplification read via plain radiography. The sensor was mounted on Sawbones tibia models (fractured and allograft repaired) and human cadaveric tibia and tested under cyclic

loading. The sensor displayed reversible and repeatable behavior with a slope of 0.096 mm/kg and fluid level noise of 50 to 80 micrometer (equivalent to 5-10 N).

While both these sensors will address the two major issues in fracture healing providing useful insight, they can be improved with future modifications. The proposed intramedullary rod design with wells can be machined in stainless steel to be a more robust sensor. Moreover, as we carried out this study as a pre-pilot study, we can extend it into a full study also combining it with antibiotic treatment in animal models. Chromoionophore III can be investigated as a potential dye for monitoring pH as well as other analytes of interest at the fracture site.

The fluidic sensor can be improved by miniaturizing the sensor components and designing it to attach to the side of the orthopedic implant plate where there's more room for sensor accommodation. In addition, the sensor can be applied in other types of fractures and implant plates as the senor was only studied on tibial implant plates.

.

ACKNOWLEDGEMENTS

First and foremost, I express my sincere gratitude to my advisor, and chair of the committee, Professor Jeffrey N Anker, for his continuous support throughout these years in his lab. I also would like to thank the rest of my committee: Prof. George Chumanov, Prof. Joe Kolis, Prof. John Desjardins, and Prof. Jeremy Tzeng, for their encouragement and insightful comments.

I would like to thank past and present members of Dr. Desjardins and Dr. Tzeng lab for collaborative work and lab mates in Anker group for providing valuable feedback, ideas, and collaborative work. Also, my sincere thanks go to all the dedicative staff at Godley Snell Research Center for their support while carrying out cadaver imaging and animal experiments. I would like to thank Department of Chemistry, Clemson University and all the funding sources supporting these projects.

I am fortunate to be a student at Clemson University and carry out my graduate studies. My sincere thanks to all the research facilities, machining and technical services, professional development opportunities, Clemson maker space, Clemson University Libraries etc. that Clemson University has to offer to be a victorious tiger.

Finally, I would like to thank my lovely family, my supportive husband, Hemal Liyanage, and my adorable daughter, Viheli Seyansa Liyanage, for standing by my side, especially when times are hard. I am grateful and want to express my indebtedness to my parents, Rajamanthri Rajamanthrilage and Yamuna Naotunna Badalge, for their unconditional love and support even though we are thousands of miles away during this wonderful journey of PhD.

TABLE OF CONTENTS

ABSTRACT……..2

ACKNOWLEDGEMENTS……..4

TABLE OF FIGURES…… 9

LIST OF TABLES……...22

CHAPTER 1. INTRODUCTION……23

1.1 Introduction to orthopedic implant-associated infections.....24

1.2 Biofilm formation and pH heterogeneity.....26

1.3 Light propagation through tissue.....35

1.3.1 Introduction to light propagation through tissue.....35

1.3.2 Wavelength dependent light propagation through tissue.....39

1.4 Different methods of detecting infection.....45

1.5 Introduction to biomechanical sensor.....48

1.6 Biocompatibility of the materials used.....50

1.6.1 Intramedullary rod sensor and implant plate sensor.....51

1.6.2 Hydromechanical sensor.....54

1.7 Introduction to thesis chapters.....55

1.8 References.....56

CHAPTER 2. HIGH SPATIAL RESOLUTION IMAGING OF IMPLANT-ASSOCIATED INFECTIONS WITH XELCI (X-RAY EXCITED LUMINESCENCE CHEMICAL IMAGING)……..70
2.1 Abstract.....70
2.2 Introduction.....71
2.3 Instrumentation.....76
2.4 Methods.....83
2.4.1 X-ray Dosage Experiment.....83
2.4.2 Comparison of XELCI technique with Plain radiography and Knife edge resolution experiment.....84
2.5 Results and Discussion.....85
2.5.1 X-ray dosage experiment.....85
2.5.2 Spatial Resolution.....85
2.6 Conclusions.....91
2.7 References.....92
CHAPTER 3. NON-INVASIVE IMAGING OF CHEMICAL CHANGES ASSOCIATED WITH INTRAMEDULLARY CANAL INFECTIONS VIA XELCI (X-RAY EXCITED LUMINESCENCE CHEMICAL IMAGING)……..97
3.1 Abstract.....97
3.2 Introduction.....98

3.3 In vitro imaging (Rabbit cadaver) of pH through tissue and bone 101
3.3.1 Fabrication of the rod sensor.....102
3.3.2 Preparing the rabbit cadaver for imaging.....103
3.3.3 Imaging through tissue and bone 103
3.4 Imaging pH through tissue and bone in live Rabbit model 104
3.4.1 Fabrication of the rod sensor.....105
3.4.2 Fabrication of the plate sensor 106
3.4.3 Growing bacteria on the rod sensor 108
3.4.4 Sensor insertion and rabbit surgery.....109
3.4.5 Imaging through bone and tissue 112
3.4.6 Postmortem studies and pH reversibility studies 113
3.4.7 Calibration curve for the rod sensor through tissue 113
3.4.8 Calibration curve for the plate sensor through tissue.....113
3.5 Results and Discussion 114
3.5.1 In vitro imaging (Rabbit cadaver) of pH through tissue and bone 114
3.5.2 In vivo imaging (Rabbit studies) of pH through tissue and bone 116
3.6 Conclusions and Future work 135
3.7 References.....139
CHAPTER 4. MEASURING ORTHOPEDIC PLATE STRAIN TO TRACK BONE HEALING USING A FLUIDIC SENSOR READ VIA PLAIN RADIOGRAPHY……..144
4.1 Abstract.....144

4.2 Introduction.....145
4.3 Device operating principle.....147
4.4 Device fabrication.....149
4.5 Sensor monitoring on the tibial implant plate.....150
4.6 Measuring fluid level under load in a composite sawbones tibial model.....151
4.7 Measuring fluid level under load in a fractured human cadaveric tibial specimen 155
4.8 Measuring fluid level at different angles and different magnifications.....160
4.9 Discussion.....167
4.9.1 Sensor range and precision 167
4.9.2 Comparison to other loaded X-ray techniques.....172
4.9.3 Fluidic length changes at different angles and magnifications.....175
4.10 Conclusions and future work 176
4.11 References.....177
CHAPTER 5. CONCLUSIONS AND FUTURE WORK……183
5.1 X-ray interrogated implantable biochemical sensor for monitoring implant associated infections 183
5.2 X-ray interrogated implantable biomechanical sensor for monitoring fracture healing.....193
5.3 References.....194
Appendix A 197
Appendix B 201

LIST OF FIGURES

Figure Page

1.1 Clinical, radiological, surgical, and nuclear imaging features of fracture- related infections a) Fistula which is a communication with the bone or implant b) Wound breakdown with exposed implant c) Plain radiograph showing a nonunion with implant failure, which is considered an FRI d) Intraoperative view of an infected nonunion with plate breakage e) CT image of a subacute intraosseous FRI after fracture treatment, known as Brodie's abscess f) FDG PET/CT image of an encapsulated sequestrum (piece of dead bone which often maintains an FRI) g) Schematic representation of the sequestrum surrounded by an abscess together with a sinus tract to the soft tissues and involucrum (periosteal bone formation caused by pus accumulation below the periosteum) of the bone h) WBC SPECT/CT image shows a hotspot at the fracture site after plate osteosynthesis for the distal tibial fracture i), j) Dual time point WBC scintigraphy with ^{99m}Tc-HMPAO-labelled autologous leucocytes showing (i) uptake in the early phase (j) increase in intensity in the late phase, which is a clear sign of infection[20] (Reproduced with the permission from Reference 20).....29

1.2 Lateral pH distribution within an intact microcolony. A) 2D schematic of distribution of the biofilm microcolonies pH gradient in the bottom, middle, and top layers. B) Ratiometric CLSM x,y cross-sectional images showing pH gradients within the

microcolonies of three individual 72h P. fluorescens biofilms (I-III) in the bottom, middle, and top layers, respectively. The pH was analyzed ratiometrically based on the FITC (sensor) and RITC (reference) images and is expressed as a false-colored rainbow spectrum. Scale bars represent 50 μm[23] (Reproduced with the permission from Reference 23). 33

1.3 Photos of text on a computer screen seen through increasingly scattering media: a) 100% water; b) 0.5% whole milk + 99.5% water; c) 1% whole milk + 99% water; d) 1.5% whole milk + 98.5% water; e) whole milk. 37

1.4 Red laser light diffusion through tissue. Red light can pass through the tissue, although it is attenuated. Importantly, while the laser starts as a small spot aiming in one direction, after passing through the finger, a large area of the finger illuminated preventing high resolution imaging of light sources.....39

1.5 Absorption spectra of the forearm of the volunteers with a thinner and a thicker fat layer. The superficial fat layer greatly makes the optical properties of the underlying tissue.[49] (Reproduced with the permission from Reference 49) 40

1.6 Typical scattering spectra of the abdomen, the female breast, forearm, and forehead.[49] (Reproduced with the permission from Reference 49). 42

1.7 The graph of calculated Transmittance (T) vs Tissue penetration depth (cm). 43

2.1 Characteristics of the XELCI imaging System. A) Three key features of XELCI. B) Comparison of XELCI imaging to other techniques. (Reproduced with the permission from Reference Rajamanthrilage et al, High Spatial Resolution Chemical Imaging of Implant-Associated Infections with X-ray Excited

Luminescence Chemical Imaging Through Tissue. J. Vis. Exp. (Pending Publication), e64252, In-press (2022)) 73

2.2 Schematic showing principle of XELCI imaging a) Schematic showing implant irradiated with focused X-ray beam and luminescence collected for detection; b) zoomed-in view of the scintillator and pH-sensitive film coated intramedullary rod sensor; c) at low pH caused by infection, intramedullary rod sensor turns from blue to yellow, while dye-free reference region is unchanged; d) zoomed-in view of intramedullary rod during an infection. (Reproduced with the permission from Reference Rajamanthrilage et al, High Spatial Resolution Chemical Imaging of Implant-Associated Infections with X-ray Excited Luminescence Chemical Imaging Through Tissue. J. Vis. Exp. (Pending Publication), e64252, In-press (2022))..... 74

2.3 A schematic diagram showing parts of the XELCI imaging system. (Reproduced with the permission from Reference Rajamanthrilage et al, High Spatial Resolution Chemical Imaging of Implant-Associated Infections with X-ray Excited Luminescence Chemical Imaging Through Tissue. J. Vis. Exp. (Pending Publication), e64252, In-press (2022)) 80

2.4 A photograph of the XELCI imaging system. (Reproduced with the permission from Reference Rajamanthrilage et al, High Spatial Resolution Chemical Imaging of Implant-Associated Infections with X-ray Excited Luminescence Chemical Imaging Through Tissue. J. Vis. Exp. (Pending Publication), e64252, In-press (2022))..... 81

2.5 LabVIEW control scheme for the XELCI imaging system. (Reproduced with the permission from Reference Rajamanthrilage et al, High Spatial Resolution Chemical Imaging of Implant-Associated Infections with X-ray Excited Luminescence Chemical Imaging Through Tissue. J. Vis. Exp. (Pending Publication), e64252, In-press (2022)) 83

2.6 Exposure of gaffchromic paper for measuring X-ray Dose. A) The scanned area at 5 mm/sec speed and comparison of the color with the color chart. B) The scanned area at 1 mm/sec speed and comparison of the color with the color chart. C) The zoomed in view of the few lines of the scanned area. 85

2.7 Plain radiography vs. functional radiography. (i) Images of three targets acquired using a digital camera, (ii) Plain radiography and XELCI imaging. (a) Photo with no tissue of the three targets on scintillator film. (b) Plain radiograph of the three targets with no tissue. (c) XELCI image of the three targets on scintillator film with no tissue. (d) Photo with tissue of the three targets on scintillator film. (e) Plain radiograph of the three targets with tissue. (f) XELCI image of the three targets on scintillator film with tissue.....86

2.8 Measuring knife edge resolution with XELCI images of a line target with 700 nm light channel and light intensity profiles across the targets and zoom in profile at the edge of the 2 mm wide line. a) Image of 700 nm light through no tissue. b) Light intensity profiles across the four line widths with no tissue. c) Light intensity profiles at the edge of the 2 mm wide line with no tissue. d) Image of 700 nm light through 5 mm tissue. e) Light intensity profiles across the four line widths through 5 mm tissue.

f) Line profiles at the edge of the 2 mm wide line through 5 mm tissue. g) Image of 700 nm light through 10 mm tissue. h) Light intensity profiles across the four line widths through 5 mm tissue i) Zoom in of profiles at the edge of the 2 mm wide line through 10 mm tissue. 88

3.1 Schematic diagram showing general steps of fabricating a rod sensor. 103

3.2 A photo of the plate sensor to implant on the surface of the femur. 108

3.3 Photos and plain radiographs acquired during the surgery of Rabbit 1 A) The femur exposed and ready for the implant plate to be placed. B) Preparing the tibia for placing the intramedullary rod sensor. C) The plain radiograph obtained after the two surgeries showing the rod sensor placed in the tibial intramedullary canal (the plate and sensor was further up on the femur, not in view here, but evident in Figs. 3.4 and 3.5 for Rabbits 2 and 3). 110

3.4 Photos and plain radiographs acquired during the surgery of Rabbit 2 A) The femur exposed and implant plate glued to the femur. B) Localization of the intramedullary rod sensor with a biofilm grown in the proximal tibia. C) The plain radiograph obtained after implant implantation. 111

3.5 Photos and plain radiographs acquired during the surgery of Rabbit 3. A) The femur exposed for the implant plate to glue and showing the tissue thickness of the flap of tissue over the femur. B) Drilling the tibia for inserting the intramedullary rod sensor. C) The plain radiograph obtained after the two surgeries 112

3.6 (A) Stainless steel rod coated with Gd_2O_2S:Eu incorporated epoxy and pH sensitive Acrylamide-PEG gel (B) The coated stainless - steel rod inserted to the drilled hole in the rabbit tibia.[7] (Reproduced with the permission from Reference 7). 115

3.7 XELCI images of the rod sensor in the intramedullary canal. (A) Analyzed image for 620 nm wavelength. (B) Analyzed image for 620 nm wavelength. (C) Analyzed Ratio image (I_{620}/I_{700}). (D) Plain radiograph of the sensor. (E) Superimposed radiograph and XELCI ratio image.[7] (Reproduced with the permission from Reference 7). 116

3.8 Ratio images I_{620}/ I_{700} for Control rabbit (Rabbit 1). A) The XELCI ratio images of the rod sensor showing the pH variations throughout the days Day 0 through Day 11. B) The XELCI ratio images of the plate sensor showing the pH variations throughout the days Day 0 through Day 11. 117

3.9 Ratio images I_{620}/ I_{700} for infected-inoculated rabbit (Rabbit 2). A) The XELCI ratio images of the rod sensor showing the pH variations throughout the days Day 0 through Day 10. B) The XELCI ratio images of the plate sensor showing the pH variations throughout the days Day 0 through Day 10. 118

3.10 Ratio images I_{620}/I_{700} for rabbit with rod cultured with bacterial prior to implantation (Rabbit 3). A) The XELCI ratio images of the rod sensor showing the pH variations throughout the days Day 0 through Day 11. B) The XELCI ratio images of the plate sensor showing the pH variations throughout the days Day 0 through Day 11...119

3.11 Calibration studies for rod sensors A) The rod sensors incubated in different pH solutions. B) The graph of ratio (Signal/Reference) vs pH curve for with no tissue

and with porcine tissue. C) pH change over time for Rabbit 1,2 & 3 (Average ratio normalized to sensor region over time for Rabbit 1,2 & 3, and associated pH calculated from calibration curve B with no tissue). Error bars calculated from standard deviation of pixels in sensor region.....121

3.12 Calibration studies for hydrogel sensors on plates and data for plates in Rabbit prepilot studies. A) Photo of the gel sensors incubated in different pH solutions. B) The XELCI Ratio (Signal/Reference) vs pH with no tissue and with porcine tissue. C) pH change over time for Rabbit 1,2 and 3 (Average ratio normalized to sensor region vs time for Rabbit 1,2 and 3). 123

3.13 Postmortem images of Rabbit 1 after extraction of implant plate. a) Testing the pH of the surrounding tissue of the implant plate (i) rubbing the pH test strip on the tissue (ii) photo showing the color change of the pH strip. b) Testing the pH of the gels embedded in the implant plate (i) implant plate extracted after postmortem (ii) photo showing the color change of the pH strip for big chamber (iii) photo showing the color change of the pH strip for small chamber.....124

3.14 Testing pH of the fluids of tibial opening and extracted rod sensor from Rabbit 1 A) Testing pH of the top of the tibia. B) Testing pH of the surface of the rod sensor. C) The pH strip indicating the pH.....125

3.15 Postmortem images of Rabbit 2 after extraction of implant plate: a) Testing the pH of the surrounding tissue of the implant plate (i) rubbing the pH test strip on the tissue (ii) photo showing the color change of the pH strip. b) Testing the surface pH

of the two chambers (i) explanted implant plate (ii) pH of the big chamber (iii) pH of the small chamber. 126

3.16 Testing pH of the fluids of tibial opening and extracted rod sensor from Rabbit 2 A) (i) Testing the pH of the tissue on top of tibia (ii) The pH strip showing the pH B) (i) Testing the pH of the top of the implant (ii) The pH strip showing the pH C) (i) Testing the pH of the implant surface (ii) The pH strip showing the pH 127

3.17 Postmortem images of Rabbit 3 after extraction of implant plate. A) Testing the pH of the surrounding tissue of the implant plate (i) rubbing the pH test strip on the tissue (ii) photo showing the color change of the pH strip. A) Photos of testing the pH of adjacent fluid using pH indicator paper. 128

3.18 Testing pH of the fluids of tibial opening and extracted rod sensor from Rabbit 3. A) (i) Testing the signs of infection/Abscesses (ii) The pH strip showing the pH. B) (i)Explanted rod sensor (ii) pH strip showing rod surface pH. 129

3.19 Reversibility studies for hydrogel pieces from implant plates. (i) The sensor incubation in the pH 7.4 buffer for Rabbits 1, 2 and 3. (ii) The sensor incubation in the pH 5 buffer for Rabbits 1, 2 and 3. (iii) The sensor incubation again in the pH 7.4 buffer for Rabbits 1, 2 and 3 (for each buffer a start and end of the sensors are shown). 130

3.20 Reversibility studies for explanted rod sensors (i) The sensor incubation in the pH 7.4 buffer for Rabbits 1,2 and 3. (ii) The sensor incubation in the pH 5 buffer for Rabbits 1,2 and 3. (iii) The sensor incubation again in the pH 7.4 buffer for Rabbits

1,2 and 3 (For Rabbit 3, the rod sensors were compared to the initial color of a fabricated neutral sensor). 132

3.21 The Solidworks design of new version of the intramedullary rod sensor (All the dimensions are in mm). 138

4.1 Sensor mechanism. a) Schematic of fluidic sensor at 0 N. b) Corresponding photograph in a Sawbones tibial mimic (arrow shows fluid level). c) Schematic of fluidic sensor at 400 N: plate bending displaces the lever, releasing the bulb and lowering the fluid level. d) Corresponding photograph with fluid level at 400 N. [Reproduced with the permission from **Rajamanthrilage A.C.** et al.: "Measuring Orthopedic Plate Strain to Track Bone Healing Using a Fluidic Sensor Read via Plain Radiography". IEEE Transactions in Biomedical Engineering. (June 2021)]. 148

4.2 SolidWorksTM designs of two main parts of the hydraulic sensor showing different views of the designs A) bulb and fluid capillary sensor; B) lever part of the sensor with one end which attaches to the plate, and a second end which presses on the bulb with a pressure and displacement which depends on the degree of plate bending. (All measurements are in mm) [Reproduced with the permission from **Rajamanthrilage A.C.** et al.: "Measuring Orthopedic Plate Strain to Track Bone Healing Using a Fluidic Sensor Read via Plain Radiography". IEEE Transactions in Biomedical Engineering. (June 2021)]. 150

4.3 Sensor reading during five load cycles for a plated cadaveric tibia with an unstable fracture. a) Plain radiographs showing the fluid level changes with vs. applied load through one load cycle (red arrow shows fluid level). b) Force applied and fluid

displacement vs. image number. c) Five-cycle-average fluid displacement vs. applied force. [Reproduced with the permission from **Rajamanthrilage A.C.** et al.: "Measuring Orthopedic Plate Strain to Track Bone Healing Using a Fluidic Sensor Read via Plain Radiography". IEEE Transactions in Biomedical Engineering. (June 2021)]. 154

4.4 Plain radiographs showing the fluid level changes (little or no change) for allograft-repaired tibia with respect to applied load through one cycle. (Red arrow points to fluid level) [Reproduced with the permission from **Rajamanthrilage A.C.** et al.: "Measuring Orthopedic Plate Strain to Track Bone Healing Using a Fluidic Sensor Read via Plain Radiography". IEEE Transactions in Biomedical Engineering. (June 2021)]. 155

4.5 Photos of experimental setup for measuring plate strain on a cadaveric tibia with an unstable fracture. a) Fluidic sensor attached near the fracture gap. b) Zoomed-in view of the sensor (red arrow points to fluid level). [Reproduced with the permission from **Rajamanthrilage A.C.** et al.: "Measuring Orthopedic Plate Strain to Track Bone Healing Using a Fluidic Sensor Read via Plain Radiography". IEEE Transactions in Biomedical Engineering. (June 2021)].....157

4.6 Sensor reading during five load cycles for a plated cadaveric tibia with an unstable fracture. a) Plain radiographs showing the fluid level changes with vs. applied load through one load cycle (red arrow shows fluid level). b) Force applied and fluid displacement vs. image number. c) Five-cycle-average fluid displacement vs. applied force. [Reproduced with the permission from **Rajamanthrilage A.C.** et al.:

"Measuring Orthopedic Plate Strain to Track Bone Healing Using a Fluidic Sensor Read via Plain Radiography". IEEE Transactions in Biomedical Engineering. (June 2021)].....159

4.7 Fluid level measured at different angles of fractured Sawbones® tibia (fluidic sensor without Ta bead reference). a) Radiographs taken at different X-ray source angles i) through vi) respectively 7.7°, 3.1°, 0°, -4.1°, -7.1°, -11.4°. b) Measured fluid level (from top of bulb) vs angle. [Reproduced with the permission from **Rajamanthrilage A.C.** et al.: "Measuring Orthopedic Plate Strain to Track Bone Healing Using a Fluidic Sensor Read via Plain Radiography". IEEE Transactions in Biomedical Engineering. (June 2021)].....161

4.8 Fluid level measured at different positions and effective magnifications of fractured Sawbones® tibia (fluidic sensor without Ta bead reference). a) Radiographs of specimen positioned at different distances i) through v) respectively -10, -5, 0, 5, 10 cm. b) Measured fluid level vs specimen distance. [Reproduced with the permission from **Rajamanthrilage A.C.** et al.: "Measuring Orthopedic Plate Strain to Track Bone Healing Using a Fluidic Sensor Read via Plain Radiography". IEEE Transactions in Biomedical Engineering. (June 2021)].....162

4.9 Fluid level measured at different angles of fractured Sawbones® tibia (fluidic sensor with embedded Ta bead references). a) Radiographs taken at different X-ray source angles i) through vii) respectively 15°, 10°, 5°, 0°, -5°, -10°, -15°. Red arrows point to the Ta beads. b) Measured fluid level with respect to top bead vs. X-ray source angle. [Reproduced with the permission from **Rajamanthrilage A.C.** et al.:

"Measuring Orthopedic Plate Strain to Track Bone Healing Using a Fluidic Sensor Read via Plain Radiography". IEEE Transactions in Biomedical Engineering. (June 2021)].....165

4.10 Fluid level measured at different positions and effective magnifications of fractured Sawbones® tibia (fluidic sensor with embedded Ta bead references) a) Radiographs of specimen positioned at different distances i) through v) respectively -6, -3, 0, 3, 6 cm. Red arrows show the tantalum beads. b) Measured fluid level vs. position [Reproduced with the permission from **Rajamanthrilage A.C.** et al.: "Measuring Orthopedic Plate Strain to Track Bone Healing Using a Fluidic Sensor Read via Plain Radiography". IEEE Transactions in Biomedical Engineering. (June 2021)].....166

4.11 Plate load to failure for different activity levels. a) Estimated load (N) to failure vs. number of cycles for bent and unbent plates. b) Construct load to failure (N) and associated activity vs. percentage of load carried by plate assuming bent plate from part(a) and 80 kg patient. [Reproduced with the permission from **Rajamanthrilage A.C.** et al.: "Measuring Orthopedic Plate Strain to Track Bone Healing Using a Fluidic Sensor Read via Plain Radiography". IEEE Transactions in Biomedical Engineering. (June 2021)].....170

5.1 Control rabbit (Rabbit 4). XELCI ratio images of the rod sensor during the imaging days. 187

5.2 Infected rabbit-I (Rabbit 6). XELCI Ratio images of the rod sensor during the imaging days. (Red arrow is pointed to the broken gel layer extracted with the sensor) ..187

5.3 Infected rabbit II (Rabbit 7). XELCI Ratio images of the rod sensor during the imaging days. 188

5.4 Photos of chromoionophore mixture and drop coated on filter paper. A) Red colored sensor in acidic solution. B) Blue colored sensor in basic solution.....191

5.5 The extinction spectra and pH curves. A) The extinction spectra for Chromoionophore film coated filter paper in different pHs. B) The pH response curve and least squares fit to simulated protonated and deprotonated indicator dye concentration assuming two state system (acid and base) with species distributed according to Henderson-Hasselback equation.....192

LIST OF TABLES

Table Page

1.1 Tissue penetration depth at different wavelengths for thinner and thicker tissue.....41

1.2 Different methods of monitoring implant associated infections.....47

1.3 Sensor components 51

4.1 Average displacements at different loads for Sawbones® tibia models with an unstable fracture.....152

4.2 Average displacements at different loads for Sawbones® tibia models with an allograft-repaired fracture.....153

4.3 Average displacements at different loads for Human cadaver tibia with an unstable fracture.....160

5.1 The composition for the Chromoionophore III films 191

CHAPTER 1

INTRODUCTION

Bone Fractures or Musculoskeletal injuries and their associated complications have become a major health issue worldwide. They are relatively common and different methods are available for fracture fixation to stabilize the fractured bone ranging from casts, braces, external splinting to intramedullary rods, implant plates and, orthopedic screws etc. Many of the fractures are treated nonoperatively, while many fractures require operative treatment. In the USA alone, 2 million fracture fixation surgeries occur yearly, yet treatments are complex and expensive. Fracture healing/bone repair is the specific physiological process that leads to the restoration of skeletal integrity because of several complex biochemical and biomechanical changes. While a greater fraction heals normally, it is believed that 5-10% of all fracture fixation surgeries are associated with impaired healing. Among the several complications associated, nonunion/refracture and fracture-associated infections are known as major issues. These complications may present simultaneously, or one can arise because of the other. Therefore, it is essential and critical to study this problem and try to address it by developing appropriate solutions.

This dissertation describes two major solutions to address two main complications associated with fracture fixation: I) fracture-related infection and II) nonunion or refracture that can occur due to early weight bearing by hardware. To address the first problem, determine the implant associated infections, a pH sensitive dye incorporated sensor was

developed. To address the second, a hydro-mechanical sensor with X-ray readout was developed to monitor orthopedic plate bending stress during fracture healing.

1.1 Introduction to orthopedic implant-associated infections

Orthopedic hardware such as implant plates, screws, intramedullary nails or external fixators are commonly used by surgeons to keep the bone fragments in place with the correct angle allowing the fractured bones to heal. Introducing these orthopedic implants increase the risk of infection (most commonly caused by *Staphylococcus aureus* and *Staphylococcus epidermidis*). Bacteria can form antibiotic resistant biofilms on the implant surfaces leading to prolonged hospitalization, complex revision procedures, and sometimes complete failure of the implant which may require secondary surgery for its removal, increasing the financial burden and mortality rate.[1,2] Implant associated infections can be caused by bacterial contamination during surgery, debris from the wounds or subsequent adhesion of opportunistic microorganisms on to the implant surface.[3]

Orthopedic implant infection can often lead to osteomyelitis (bone infection). Chronic osteomyelitis is one of the most challenging type of infections to treat and it can arise as a result of open injury, operative procedures or rarely with hematogenous seeding.[4,5] Osteomyelitis includes an inflammatory process caused by an infecting microorganism which leads to bone destruction (Osteolysis).[6] *Staphylococcus aureus* (S. aureus) is the most common causative pathogen which is a highly opportunistic species in chronic bone infections.[7] Osteomyelitis can occur at a specific portion of the bone or can spread in several regions such as marrow, cortex, periosteum, and the surrounding soft

tissue. It is a heterogeneous disease and considered incurable depending on the persistence of bacteria deep in the bone. Early diagnosis will be challenging as the signs of infection may appear in later stages. Thus, Imaging techniques play an important role in diagnosis and follow-up.[8] These infections can be classified as early postoperative or delayed/ chronic depending on the onset of symptoms after implantation. Early postoperative is usually acquired during trauma or implant surgery, caused by virulence organisms in 1-2 weeks and delayed/chronic can occur even after a month (2-10 weeks) due to low virulence organisms. Infections can be caused by microbial spread through bloodstream from a distant focus of infection (hematogenous) or by direct or lymphogenic spread from adjacent infectious focus or penetrating trauma (contiguous).[8,9] After around 3 weeks, implants often need to be removed to initiate the treatments for infection and a replacement surgery for eradication of the infection.[10,11] Risk associated with infection, secondary surgeries and hospitalization can be prevented by the existence of imaging techniques to monitor and locate these infections within the first three weeks.

We developed a pH sensor for monitoring intramedullary rod associated infections (e.g., osteomyelitis) and a novel imaging technique which would allow us to image and map pH variations through bone and tissue. With our technique, we can monitor the pH changes in the surrounding environment and detect implant associated infections early to start the infection eradication treatments avoiding life threatening or costly procedures. Our group has previously reported detecting the luminescent signal from the scintillators at one wavelength irradiating X-rays at a single location giving rise to 2D image without scanning the sample. Next, we improved the technique to non-invasively monitoring pH changes

occurring at the surface of a femur implant plate in the live animal models. With these studies we showed that the principle works for detecting in vivo surface specific pH on implanted devices. This dissertation describes the advancement of pH imaging with an intramedullary rod sensor and an improved imaging technique to monitor pH variations occur inside the bone cavity. We show we can carry out non-invasive pH imaging and mapping through much thicker tissue thicknesses compared to imaging the bone surface in rabbit cadaveric models and live rabbit models.

1.2 Biofilm formation and pH heterogeneity

The origination and development of the implant-associated infections will occur due to the complex interaction between the host, pathogen, and the orthopedic device. A biofilm will be formed by the contact between pathogen and the orthopedic device which will affect the host- defense mechanisms. That will be the first step of biofilm formation which is described as a cycle with four different phases: 1) attachment, 2) microcolony formation 3) biofilm maturation and 4) dispersion.[12] During these phases bacteria behave differently and represent a biofilm biology which is not evident by isolated planktonic state. In the very first step of biofilm formation, free floating individual bacteria make weak interactions with the implant surfaces and develop a strong attraction within few minutes. Then they transform into microcolonies where they will begin the production of adhesins and extracellular matrix compounds for cell attachment. This extracellular polymeric substance (EPS) produced by bacteria is known as glycocalyx. It is comprised of extracellular polysaccharides, phospholipids, proteins, and DNA.[13,14] Once the glycocalyx

makes a rigid, organized layer around the cell, it is called a capsule. Eventually it diffuses and combine with the surrounding medium and EPS becomes the matrix where the cell is embedded. It will be then called as the slime layer which plays an important role during biofilm maturation. EPS accounts for significant amount of the biofilm matrix which plays major functions such as providing the structure function, maintaining overall biofilm health, intracellular bacterial adhesion and cohesion, water retention, and acting as a protective barrier against chemical changes. [15] Maturation and remodeling in the next step will allow further attachment of bacteria and colony growth. In the final step, a small population of bacterial cells as free bacteria or in clumps will be released which can be reattached to surfaces downstream.[16,17]

In the matured status of the biofilm, they are resistant to antibiotics and hard to eradicate only with antibiotic treatment. The increased antibiotic resistance develops because of gradients of oxygen, nutrients, slowed agent diffusion, pH, stress responses, gene expression (resistance factors), dormancy, and tolerance. It is believed that concentration of any nutrient which is consumed by the biofilm will decrease with respect to depth into the biofilm and distance from the nutrient source.[18] There will be developed zones of decreased metabolism and dormant bacteria due to gradients in nutrients and oxygen. Also, bacteria living in proximity in the biofilm will facilitate horizontal gene transfer of resistance mechanisms.[12] Bacteria can inherit antibiotic resistance generated by developing mutations to a specific antibiotic. Therefore, cocktails of antibiotics are more suitable for treating a biofilm rather than one antibiotic where there's a higher probability of generating more mutated bacteria.

Biofilms have heterogeneous microenvironment with significant variation in nutrients, oxygen, pH, as well as bacterial and host cells. There are regions where growth and activity are fast as well as slow. For example, Mc Lean et al report on correlated biofilm imaging, transport and metabolism measurements via combined nuclear magnetic resonance and confocal microscopy. They show a comparison of a 3D MRI and CLSM rendered images for an MR-1 biofilm containing a green fluorescent protein that are acquired consecutively.[19] MRI and CLSM which were employed on the same sample were able to provide complementary structural information. They observed individual bacterial colonies situated at varying distances and were able to resolve the 1 and 2 bacterial colonies (~400 μm apart) in both MRI and CLSM in vitro. Moreover, the figure below shows a series if images showing different imaging techniques carried out on a fractured bone treated with implant plate which is suspected to be infected. The nuclear imaging (WBC SPECT/CT imaging Figure 1.1 h) carried out on the fractured implant with an infection showed several localized regions surrounding the implant infection.[20] In other cases, infections are more uniformly distributed over the implant. How infection spread in vivo, respond to treatments, and grow back for incomplete treatments is not generally known and may depend on the case. XELCI is designed to image pH variations associated with localized infection/inflammation regions at the implant surface; the resolution should be better than PET/SPECT (typically 1 mm or more) and provide more quantitative measurements of the local biochemistry (pH in this dissertation, although it can work with other chemical indicators in future).

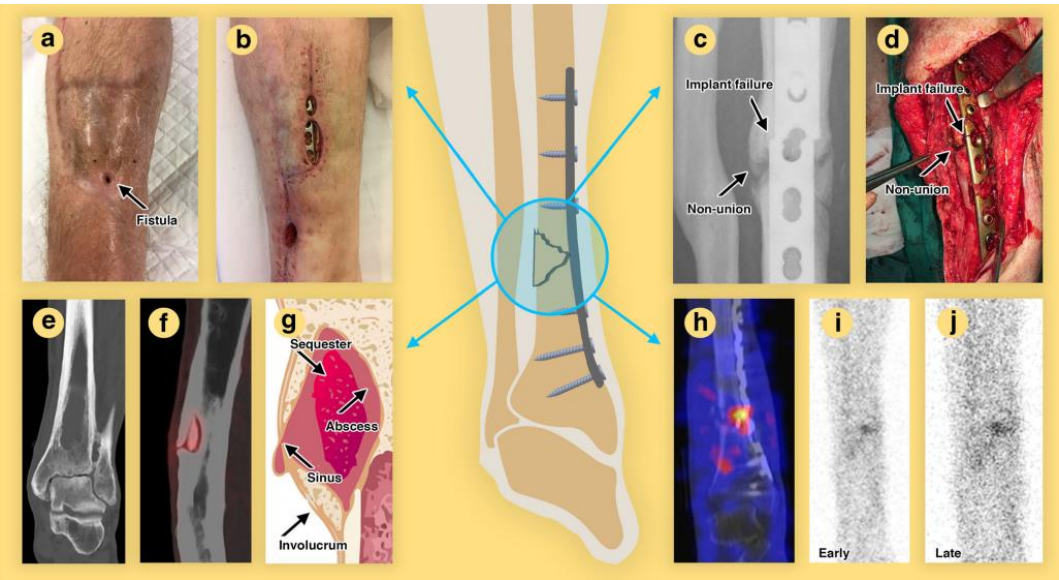

Figure 1.1: Clinical, radiological, surgical, and nuclear imaging features of fracture-related infections a) Fistula which is a communication with the bone or implant b) Wound breakdown with exposed implant c) Plain radiograph showing a nonunion with implant failure, which is considered an FRI d) Intraoperative view of an infected nonunion with plate breakage e) CT image of a subacute intraosseous FRI after fracture treatment, known as Brodie's abscess f) FDG PET/CT image of an encapsulated sequestrum (piece of dead bone which often maintains an FRI) g) Schematic representation of the sequestrum surrounded by an abscess together with a sinus tract to the soft tissues and involucrum (periosteal bone formation caused by pus accumulation below the periosteum) of the bone h) WBC SPECT/CT image shows a hotspot at the fracture site after plate osteosynthesis for the distal tibial fracture i), j) Dual time point WBC scintigraphy with ^{99m}Tc-HMPAO-labelled autologous leucocytes showing (i) uptake in the early phase (j) increase in intensity in the late phase, which is a clear sign of infection[20] (Reproduced with the permission from Reference 20).

Low pH regions are generated in biofilms due to anaerobic fermentation by bacteria in low oxygen environments, as well as poor clearance of organic acids such as lactic acid and acetic acid.[21] Accumulation of these products can lead to reduced pH regions.[18] Hunter et al have studied the pH heterogeneity of the *Pseudomonas aeruginosa* biofilms (~50 µm) using fluorinated derivative of seminaphthorhodafluor-4F 5-(and-6)-carboxylic acid (C-SNARF-4) dye. pH heterogeneity in both the x,y and x,z planes were observed with regions as low as pH 5.6 in the biofilm compared to pH 7 in the bulk fluid. More basic pH values were observed at the microcolony in the fluid-biofilm interface while the values near the substratum showed much more pH variations. The emissions closest to the substratum indicated pH values towards the center of the microcolony were (6.0 ± 0.3), while the surrounding areas were (6.3 ± 0.2).[22] The figure below of Confocal Laser Scanning Microscopy (CLSM) images shows the spatially distinct pH microenvironments observed in different depths (x,y plane) of a *Pseudomonas fluorescens* microcolony. The pH monitoring was carried out by ratio metric imaging of fluorescent mesoporous silica nano sensors (47 ±5 mm diameter). These images exhibit large, dense low pH regions closer to the substratum, range of acidic pockets (2-5 µm) distributed throughout in the bottom layers, or a combination of both large dense clusters surrounded by acidic pockets.[23] Thus it is clear that pH variations can occur over regions ranging from ~10 µm from in vitro imaging, while in vivo nuclear imaging shows biofilm localization can be ~400- 500 µm apart.

Additionally, lower pH due to infection in vivo can be a combination of local pH through immune cell activity and osteoclast activity.[24,25] The initial inflammatory phase of

bone regeneration occurs by stimulating the migration of mesenchymal stem cells, fibroblasts, and endothelial cells as well as immune cells such as macrophages driving the formation of soft callus. This phase is associated with restricted conditions such as low oxygen levels (local tissue hypoxia), low pH and high lactate concentrations.[26–28] The introduction of biomedical devices to animal body can trigger reactions related to foreign bodies which causes low pH conditions.[29] Osteoclast activity during a low pH environment during infection can cause the production of more osteoclasts. Osteoclasts generally contributes to resorption of any small bone particles generated from bone fracture or dynamic regeneration of the tissue by producing acids. But in the presence of an implant associated infection, there can be a disproportion between activities of osteoclasts vs osteoblasts causing bone erosion. Moreover, the changes in mineral composition (presence of brushite and uncarbonated apatite) in both cavities and infected bone was reported in a study carried out with Raman spectroscopy.[30] Konttinen et al observed that the tissue near an implant becomes acidic during an infection in clinical studies carried out measuring with a micro electrode. They measured acidic pH values (5- 7.5) for patients with aseptic loosening (can be due to undetected infection or inflammation caused by wear particles) and septic loosening with pH values closer to 4.4 in the femoral cavity.[31]

Luminescence based studies are reported using optical sensor films with fluorescence,[32–35] surface enhanced Raman spectroscopy,[36] upconversion,[37–39] etc. that can respond to various stimuli such as pH, temperature, pressure, ions light and humidity.[40] These imaging techniques provide an overview of the chemical measurements, but optical scattering of the excitation and emission light through thick tissue restrict the spatial

resolution. Thus, prevents the observation of tiny, localized acidic regions during implant associated infections or after antibiotic treatments. Therefore, it is required to use of a spatially distinct sensor with reference regions to account for spectral distortion and detecting multiple analytes.

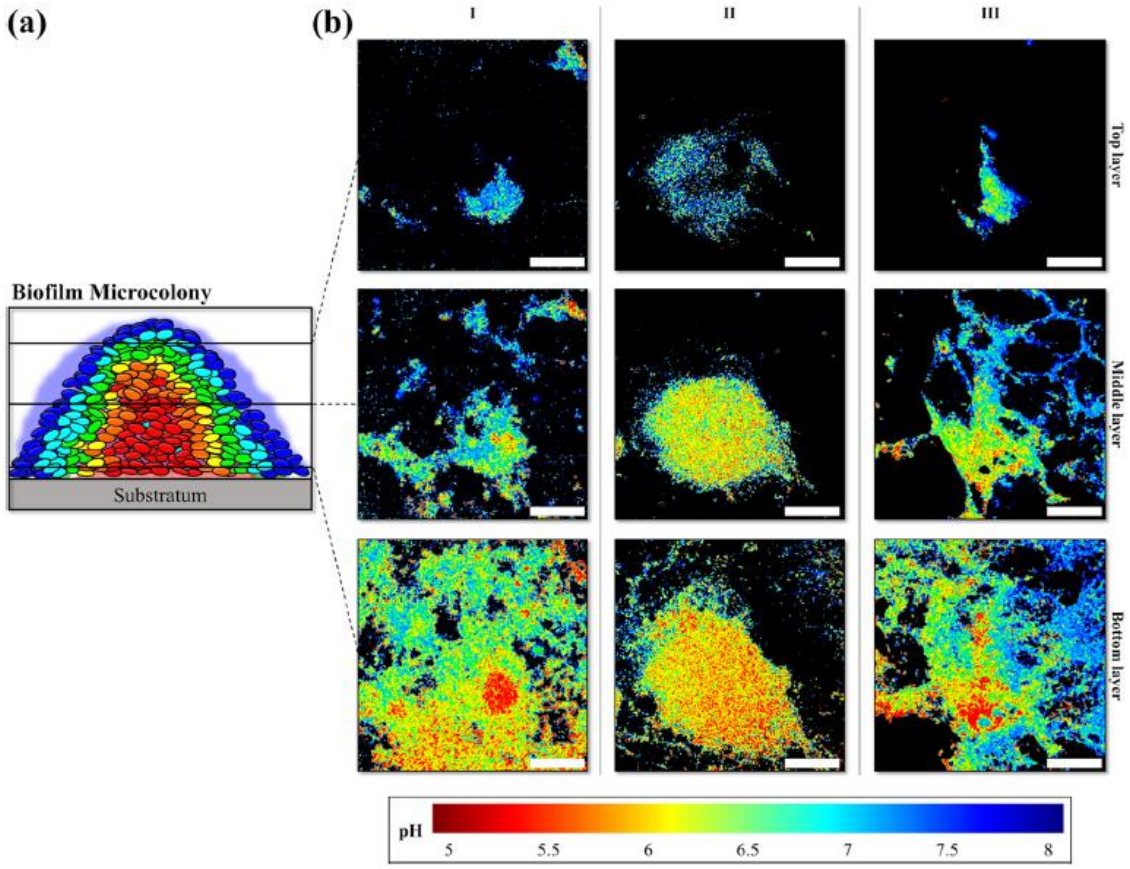

Figure 1.2: Lateral pH distribution within an intact microcolony. A) 2D schematic of distribution of the biofilm microcolonies pH gradient in the bottom, middle, and top layers. B) Ratiometric CLSM x,y cross-sectional images showing pH gradients within the microcolonies of three individual 72h P. fluorescens biofilms (I-III) in the bottom, middle, and top layers, respectively. The pH was analyzed ratiometrically based on the FITC (sensor) and RITC (reference) images and is expressed as a false-colored rainbow spectrum. Scale bars represent 50 μm[23] (Reproduced with the permission from Reference 23).

In plain radiography, implant associated infection may display as osteolysis, implant loosening, necrotic bone fragment or failure of progression of bone healing (nonunion). But first signs of anomalies will not be visible on a plain radiograph until 10-21 days after onset of osteomyelitis and there should be around 30-50% of loss in bone density for radiographs to visualize.[41] Furthermore, Computed tomography (CT scan) could provide a detailed examination as a three-dimensional assessment of the implant and surrounding area. Sometimes CT scan will have limited sensitivity because soft tissue changes might not be seen or issues with metal artifacts. At the later stages, a second surgery is required to treat the infection, to remove the infected hardware and necrotic tissue and bone fragments which will significantly affects the quality of life and function as well as healthcare cost. Therefore, functional imaging is more suitable for early detection of osteomyelitis before anatomical changes are present. Thus, we introduce XELCI as a technique for monitoring implant associated infections through high resolution imaging utilizing X-ray as an excitation source and detecting the luminescence red light generated by the scintillator particles.

For pH imaging with XELCI, a specifically coated sensor comprised of two layers (pH sensitive gel layer over Gd_2O_2S: Eu coated orthopedic hardware) is used. We hypothesize that the acidic byproducts by bacteria can diffuse into the pH sensitive hydrogel layer to indicate pH dependent color changes in the hydrogel layer. Our approach will allow us to monitor local pH changes occur on and surrounding of the implant surfaces to inform and diagnosis of infections early. Moreover, we can investigate the pH changes during infections vs normal healing processes as well as how heterogenic or uniform the

pH in those models non-invasively in vivo, dependence of those pH changes under different factors (for example environment, time, bone cavity infection or bone surface infection, in the presence of vancomycin). Also, we should be able to identify signs of an infection from the inflammation associated with injury and surgery by monitoring the changes periodically. Additionally, XELCI and the specifically coated pH repotting sensor can be utilized in follow the pH variations after treatments for infection eradication, As discussed in the Chapter 3 of this dissertation, we were able to achieve ~500 μm of spatial resolution through 1 cm of tissue for a line target cut with ~100 μm black paper. Thus, we can use a thinner pH sensitive hydrogel (~100 μm), to successfully image areas with different pH (about 500 μm distance). Although, we could image the different pH microenvironments with high spatial resolution, the current images of implant infections show a uniformly distributed pH throughout the sensor.

1.3 Light propagation through tissue

1.3.1 Introduction to light propagation through tissue

Absorption and scattering properties of light governs its penetration and propagation into living tissue.[42] The propagation of light in tissue (optical properties) of tissue can be described using the some fundamental optical properties such as absorption coefficient (μ_a), scattering coefficient (μ_s), scattering function p (θ,ϕ) where θ is the deflection angle of scatter and ϕ is the azimuthal angle of scatter, and associated scattering anisotropy (g), reduced scattering coefficient ($\mu'_s = \mu_s (1-g)$. In the red, scattering is

dominated by Mie scattering due to changes in refractive index due to cellular organelles (especially nuclei) as well as presence of vasculature and red/white blood cells in blood.[43,44] The mean free path for scattering in tissue, $1/\mu_s$, is typically ~100 μm, (i.e. just considering scattering and neglecting absorbance, the transmittance of ballistic light is; $T = e^{-\mu_s^* z}$) where z is depth in tissue. Thus, light behave ballistically (one can focus light) through up to a few hundred micrometers of tissue ($e^{-\mu_s^* z}$).

To show the effect of scattering, we looked at a text through differently scattering milk solutions. As shown in the figure below, a text on a bright screen is viewed through 100% water, several solutions with different amounts of milk+water, and 100% milk. In a clear solution like water, all the light wavelengths will be transmitted depending on the refractive index of the medium. As milk is an emulsion of fat globules (spherical diameter 3-10 μm) and casein micelles (spherical diameter 50- 500 nm) dispersed in an aqueous medium, light interacting will lead to scattering and makes the text less visible. With a very dilute milk solution in Figure 1.3 b, the text is still visible due to a one scattering event. In the presence of a single scattering event, most of the light is transmitted through the solution. Figure 1.3 c and d which are with higher milk concentration appeared to be attenuating the light than previous case. We can expect several scattering events as there are more particles in the solution. If the image contrast is increased, one can still resolve the writing through c, although the increased background to signal intensity also decreases the signal to noise ratio, and the images are too noisy to resolve individual letters even with high contrast through d). In figure 1.3 e, the text through 100% milk solution is not visible,

even with high contrast and essentially all the light is scattered (no ballistic photons). At this stage, light propagation can be modelled as a stochastic photon diffusion problem.

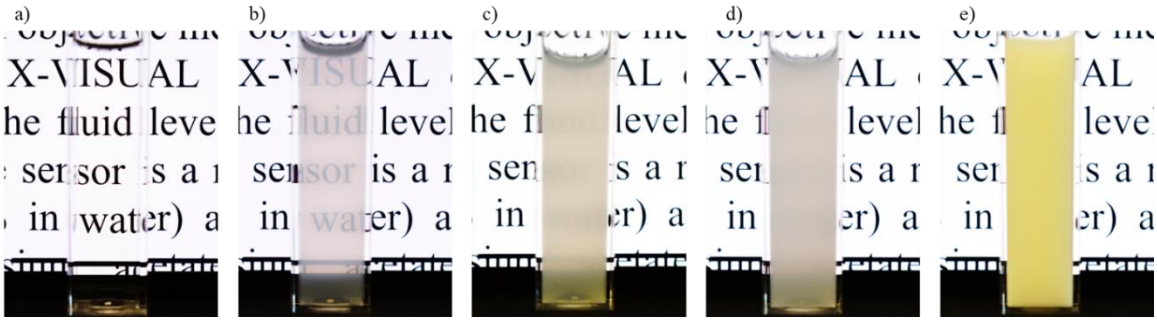

Figure 1.3: Photos of text on a computer screen seen through increasingly scattering media: a) 100% water; b) 0.5% whole milk + 99.5% water; c) 1% whole milk + 99% water; d) 1.5% whole milk + 98.5% water; e) whole milk.

Figure 1.4 below shows a demonstration of red-light diffusion through tissue by shining a red laser light through a finger. As mentioned above, the light propagate through tissue can be deflected multiple times form the original direction. After a short distance entering the tissue, the direction of each photon will be scrambled, and light propagate diffusively in all directions. The intensity decreases as it spreads out and as the light propagate diffusively in all directions. The intensity decreases as it spreads out and as the light is absorbed (the large path length from multiple scattering events increases the chance

$$\psi(\rho, z_0) = \frac{1}{4\pi D}\frac{e^{-\mu_{eff} r_1}}{r_1}$$

that light is absorbed). The Green's function for light fluence, Ψ, at a point (ρ, z) given an isotropic point source at ρ=0, z=z_0 is given by:

Where r_1 =sqrt ((z-z_0)^2 + ρ ^{2}) [45]

Where μ_{eff} = 1/sqrt (3μ_s' (μ_s'+ μ_a));

μ_s' is the reduced scattering coefficient, μ_s =(1-g);

and g= <cos θ>, typically 0.8- 1 for tissue) is the anisotropy function which defines the degree of forward scattering. Thus, the light intensity passing falls exponentially with depth through tissue due to a combination of absorption and scattering, and the light spreads out radially from any point generating a point spread function that depends upon the details of the tissue geometry and absorbance, but is typically around the depth of the tissue being imaged.[46]

Figure 1.4: Red laser light diffusion through tissue. Red light can pass through the tissue, although it is attenuated. Importantly, while the laser starts as a small spot aiming in one direction, after passing through the finger, a large area of the finger illuminated preventing high resolution imaging of light sources.

1.3.2 Wavelength dependent light propagation through tissue

Near infrared and red light penetrate through biological tissues more efficiently compared to visible light because tissue can scatter and absorb less light at longer wavelengths. A window with reasonably deep light penetration is identified at wavelengths between 650 nm and 950 nm for optical imaging as the two major absorbers (Hemoglobin and water) of visible and infrared light respectively, have their lowest absorption coefficients.[47,48]

Figures 1.5 and 1.6 below show the absorption coefficient and the reduced scattering coefficient for various tissue samples. These spectra summarize a in vivo study carried out by Taroni et al. using resolved reflectance spectroscopy. In Figure 1.3, data is plotted for two tissue samples of for arm with thinner fat layer vs a thicker fat layer. The

significant difference between two spectrums can be explained with the tissue composition analysis especially larger fraction of fat. Higher absorption coefficient for thinner arm is due to the presence of hemoglobin. The study also reveals that a thick superficial lipid layer can drastically mask the optical properties of the underlying tissue.

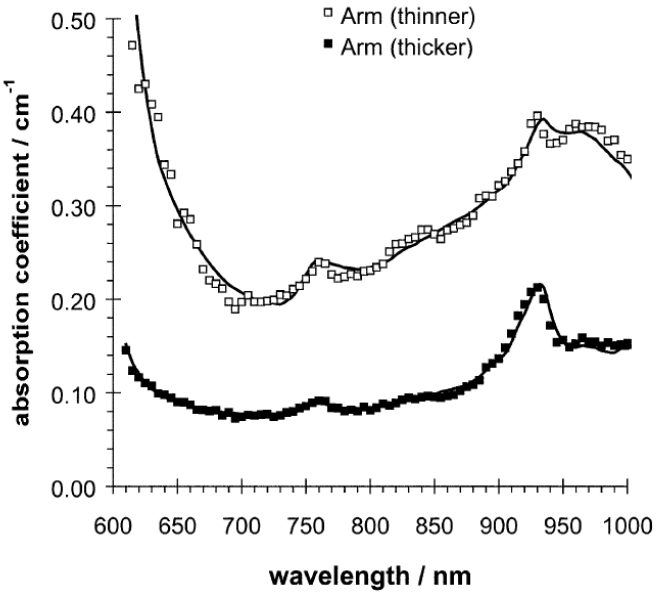

Figure 1.5: Absorption spectra of the forearm of the volunteers with a thinner and a thicker fat layer. The superficial fat layer greatly makes the optical properties of the underlying tissue.[49] (Reproduced with the permission from Reference 49)

Generally, the line shape of scattering spectra of tissue is decreasing with increasing wavelength which can be explained by the Mie theory. For the abdomen which consists of majorly of lipid structure, the scattering spectrum has the lowest slope while the arm is having the highest slope. These absorption and scattering data can be used in calculating

the attenuation of light through tissue. If the penetration depth of the light is given by $\delta = 1/\sqrt{(3\,\mu_a\,\mu'_s)}$, (assuming $\mu'_s >> \mu_a$) we can calculate the tissue penetration depths at different wavelengths for different thicknesses of tissue. The values calculated for 620 nm and 700 nm wavelengths are as below. As the penetration depth of the values suggests, 620 nm light can penetrate more through in larger distances in thick tissue while 700 nm light can penetrate more through thinner tissue.

Table 1.1: Tissue penetration depth at different wavelengths for thinner and thicker tissue

	Penetration depth at 620 nm (in cm)	Penetration depth at 700 nm (in cm)
Thinner forearm	0.24	0.41
Thicker forearm	0.49	0.67

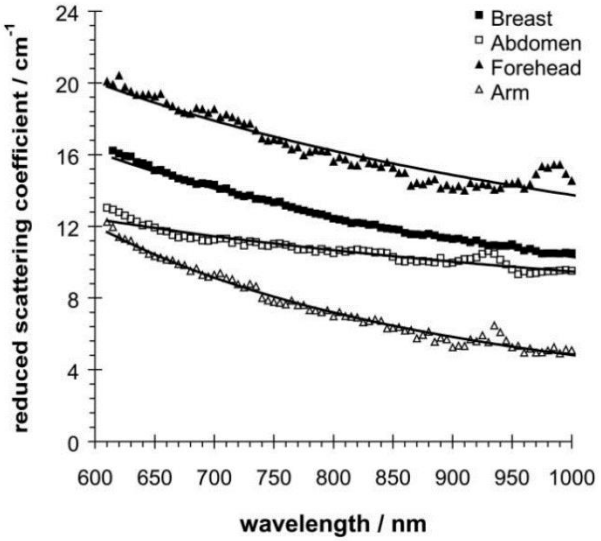

Figure 1.6 : Typical scattering spectra of the abdomen, the female breast, forearm, and forehead.[49] (Reproduced with the permission from Reference 49).

As shown in Figure 1.7 below, the light in different wavelengths (620 nm & 700 nm) penetrates differently through tissue. The graphs are plotted by using the absorption and reduced scattering coefficients reported by Taroni et al for thicker tissue.[49] This variation of wavelength dependent light penetration can affect while imaging through different thicknesses of tissue samples. Light transmittance at both wavelengths decreases exponentially while increasing the tissue thickness. 620 nm light is attenuating more rapidly compared to 700 nm. According to Uzair et al, the signal attenuation through chicken tissue varies exponentially, and we find 1/e penetration depths of (0.62±0.09 cm) for 700 nm and (0.49±0.06 cm) for 620 nm which agrees reasonably well with light attenuation through thicker tissue. Similarly in vivo Rabbit studies we report in the Chapter

3 agrees well with thinner arm penetration depths for the bone surface imaging (for 1 cm of thick tissue) providing penetration depths of 0.27 cm for 620 nm and 0.44 cm for 700nmlight. This effect is due to the higher effective attenuation coefficient at 620 nm than 700 nm.

To address the issue of spectral distortion, we always accompany the pH sensitive sensor region with a reference region in proximity without any pH sensitive film.[50] This requires that we can distinguish the reference from the sensor, which we can do because they are spatially separated and resolvable with our XELCI scanner.

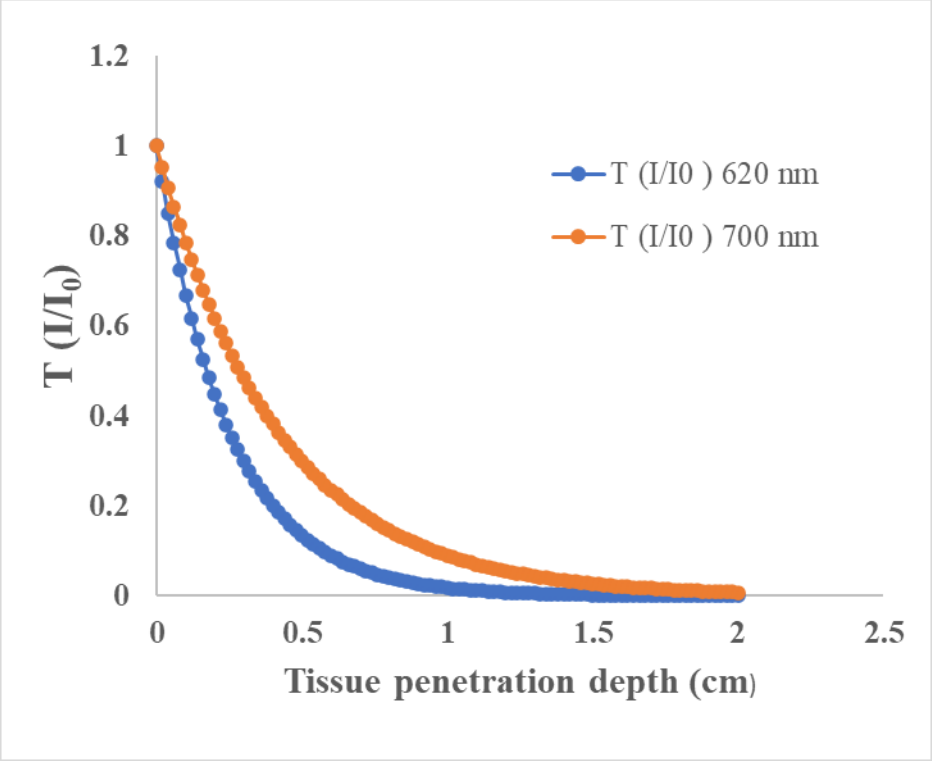

Figure 1.7: The graph of calculated Transmittance (T) vs Tissue penetration depth (cm).

The excitation photon (X-ray photons in XELCI) reaches the sensor and has several possible fates due to photoelectric effect (energy is absorbed) and scattering/Compton scattering events occur while travelling through the tissue. The X-ray photons that reach the pH sensor will excite the scintillator particles to generate visible light in the red region (prominent emissions at ~600 nm and ~700 nm). The light that reaches the detector after several absorption and scattering events due to chromophores (such as hemoglobin and melanin) and filamentous proteins, provide the information to monitor the pH of the surrounding environment.[51] As both X-rays and red light can travel longer distances through tissue XELCI can provide higher spatial resolution in imaging through tissue. Tissue can produce fluorescence effect at any instance it absorbs light and tissue autofluorescence can severely limit the signal to background ratio.[42] The excitation source in fluorescence microscopy will be focused on a plane of the specimen. The light beam will not only excite the same plane of focus but along the whole path of the excitation beam which compromise the 3D resolution since detectors collect all the emission from outside the plane of focus.[52] However, as we use X-rays which can remain focused for a larger distance to excite luminescence one point at a time to determine the pH, high-resolution images of pH variations can be achieved point-by-point scanning of the sensor.

1.4 Different methods of detecting infection

The altered chemical microenvironment present within biofilms were studied with different techniques. Miniature electrodes were used to study the biofilms and observed surface layers of a biofilm are oxygen depleted which makes an anaerobic environment in the deeper layers. Due to the local accumulation of acidic by-products (weak organic acids as succinic, butyric and propionic acids)[53] may lead to pH differences greater than 1 between the bulk fluid and the inner biofilm.[54] Konttinen et al used a sting electrode to measure pH of the surrounding area of a total hip prosthesis of patients with aseptic loosening. They observed that the pH of the patient with a well-fixed and broken cup, along the acetabular base and acetabular cup were 7.75 and 7.85 respectively. While the pH of the femoral cavity of a patient with septic loosening was 4.38 and 5.80 in the femoral stem. Also, the lowest value observed from pathological interface tissue or implant surface was 6.1 ± 0.2.[31] Microelectrode based techniques have the disadvantage of spatial resolution limitation by the tip size as well as disruption of the biofilm. Vroom et al. measured pH gradients within an oral bacterial culture by fluorescence life time imaging using two-photon excitation microscopy.[55] Beveridge and Hunter used seminaphthorhodafluor-4F 5-(and 6) carboxylic acid (C-SNARF-4), a pH sensitive fluorescent ratiometric probe for pH microenvironment analysis of *Pseudomonas aeruginosa*. They observed values as low as pH 5.6 (within the biofilm) to pH 7.0 (bulk fluid).[22] This method allows to minimize perturbations of the biofilm, and the spatial resolution is only limited by the microscope being used. But these free dyes can interact with biofilm components, potentially reducing the sensitivity of the images. Hidalgo et al. studied pH microenvironments of *Escherichia*

coli biofilms with ratiometric core-shell silica nanoparticles in combination with confocal fluorescence microscopy which allowed nondestructive imaging, as well as independent measurement of analyte concentration and reduction of the limitations of free ratiometric sensor dyes.[56]

As indicated in the Table 1.2, currently available techniques can detect the pH adjacent to the orthopedic implants. But none of those techniques were able to image the implant surface to indicate the implant surface pH. The current methods provide direct evidence of prevailing low pH in the surrounding tissue of the infected orthopedic implants and will make the pH of the infected implants more acidic. But none of them could not provide quantitative information on pH of the implant surface. In comparison to the penetrating, intraoperative pH measurements and the extracting body fluids/synovial fluid for pH measurements, XELCI approach allows long term, non-invasive pH monitoring not only during infection but also after antibiotic treatments. Early diagnosis of orthopedic implant associated infections and identifying the infectious agent can be challenging. The crucial step to a successful management is diagnosing early for targeted and long-lasting microbial therapy. We fabricated a sensor to insert into the intramedullary canal and map pH through bone and tissue via XELCI imaging technique. We believe that with this sensor, we would be able to diagnose implant associated infections in its early stages to eradicate by treating with antibiotics without a second surgery. XELCI is compared with the currently available techniques in Table 1.2 below.

Table 1.2: Different methods of monitoring implant associated infections.

	Surface specific imaging	Equilibrium/non equilibrium	High resolution through tissue	Ionizing radiation	X-ray easily superimposed	Representative references
pH microelectrode	Yes, one point at a time	non-equilibrium, (Nernst Equation) fouling and time can cause drift	Yes, one point at a time	No	No	[57–59]
Fluorescent pH indicators	Yes	Equilibrium	No	No	No	[22,60]
MRI (CEST)	Yes	Equilibrium	3D but slow	No	No	[61]
XELCI	Yes	Equilibrium	Yes	Yes	Yes	[50,62]

An intramedullary rod pH sensor was developed to study the early diagnosis and monitoring of pH changes inside the bone during an infection/osteomyelitis. We fabricated the pH-sensitive polymer-coated intramedullary rod sensors and showed that the pH decreases during metabolic activity from *Staphylococcus aureus* biofilms. We hypothesized that 1) the pH in the intramedullary canal would decrease during an infection inside the bone; and 2) the XELCI imaging system would be able to image these pH variations non-invasively in vivo through bone and tissue. Due to the acidic environment produced by implant-associated bacteria, pH variation is an excellent analytical measurement to detect early infection. pH variations at surrounding tissue were imaged and mapped with X-ray Excited Luminescence Chemical Imaging (XELCI), a technique

developed in our lab. We have fabricated a pH sensitive intramedullary rod sensor with scintillator particle incorporated roughed epoxy layer to monitor implant associated pH drop during an infection.

1.5 Introduction to biomechanical sensor

One of the consequences of infection is that the bone does not heal, which will eventually lead to construct fatigue and failure. In addition to infection, there are other reasons that healing occurs slowly or not at all, relating to the initial surgical reduction and fixation, necrotic tissue and bone, bone metabolic diseases, patient age dependent healing rates (especially age), reinjury, and others. Measuring the state of healing is important for informing patient rehabilitation protocols including when weight bearing is safe, and if adjunctive therapies are needed.

To address the early weight bearing and refracture during the fracture healing, a hydromechanical sensor was developed to monitor fracture stiffness of tibial orthopedic plate read via plain radiography. Currently, fracture healing is clinically monitored and managed via imaging studies, serologic markers, clinical examination, and traditional timeframes.[63] These techniques are subjective and only indirectly estimate the stage of healing.[64] The lack of quantitative measurements leads to suboptimal care and inhibits clear communication in the care team (physicians, patients, physical therapists, and physicians treating comorbidities). The need for objective measurements is widely recognized,[65,66] for example, in a review on non-unions Hak et al. state, “The answer to whether we need a better assessment of fracture healing is an unqualified yes.”[66]

In orthopedics, fracture healing is generally considered to be the restoration of biomechanical function, especially for measures of alignment, strength, and stiffness. As a fracture heals, the fracture callus stiffens and the load to failure increases, with the two properties increasing proportionally to each other at early stages.[67] Measuring stiffness (e.g. deflection or strain for a given load) is suitable for tracking healing and risk of failure because it can be measured nondestructively (unlike load-to-failure). For tibial fractures repaired using external fixation (pins passing through the skin connected to an external plate), the fracture stiffness can be measured by applying force across the bone and measuring the resulting pin deflection or plate bending. Several clinical studies on external fixation devices found that compared to standard clinical assessment, decisions based on mechanical stiffness dramatically decreased refracture rates while also reducing average time to hardware removal.[67,68] Similarly, in a clinical study of 27 patients with a titanium femoral plate instrumented with a strain gauge and wireless telemetry, Seide et al found a wide range of healing rates (as measured by decrease in relative elasticity), and strong correlations between mechanical and CT analysis of callus healing.[69] However, such sensors contain complex and sophisticated circuitry for sensing, power, and telemetry and have proven difficult to introduce into the market. Researchers have also proposed methods to non-invasively measure strain on orthopedic devices using ultrasound,[70] implanted magnetoelastic wireless electronic devices,[71,72] and analysis of vibrations through the bone.[73,74] However, all of these approaches are at early stages and would require additional infrastructure and cost to be clinically translated. The fluidic sensor was attached to the orthopedic plate and response (fluid height) was monitored during load cycling. It is

convenient for a physician to monitor whether the patient is ready to start weight bearing with no complications or without delaying it for unnecessary time.

1.6 Biocompatibility of the materials used

Materials used for biomedical applications that are with direct contact to tissues need to be safe with no potential adverse effects. Also, they should not involve in harmful reactions inside the animal body. In other words, the materials should be able to function in specific applications in the presence of an appropriate host response. It indicates that biocompatible material may not be entirely inert but still can be used in in vivo applications.[75] Table 1.3 below shows the key components of the sensors, and we report the biocompatibility of the materials used for fabricating them. We provide experimental data on the biocompatibility of some of the materials used or data from literature to support their usage in vivo.

Table 1.3: Sensor components.

Type of the sensor	Chemical components associated with the sensor
Biochemical sensor	Intramedullary rod (made of Stainless steel) and implant plate sensor (made of Polycarbonate) • pH sensitive layer Poly acrylamide Bromothymol blue Unreacted monomers or photo initiator • Scintillator layer Epoxy/PDMS (Polydimethylsiloxane) Gd_2O_2S: Eu micro particles
Biomechanical sensor	• Fluidic device (made of Acrylic) Cesium Acetate (radiopaque fluid)

1.6.1 Intramedullary rod sensor and implant plate sensor

The biochemical sensors used in this work are of two types: 1) Intramedullary rod sensor and 2) Implant plate sensor. The Intramedullary rod is made of stainless steel, commonly used in biomedical applications[76], and the implant plate is made of polycarbonate. Polycarbonate is also widely used as a biomaterial due to its excellent

mechanical properties and degrade slowly under physiological conditions. Few of the derivatives of the polycarbonates are even used as biodegradable polymers for use in drug delivery and orthopedic applications.[77]

As discussed later in this dissertation, we developed a polyacrylamide-based pH indicating hydrogel to monitor implant-associated infections in the intramedullary cavity. Both rod sensor and implant plate sensors are comprised of two layers, a Bromothymol blue incorporated polyacrylamide hydrogel layer over Gd_2O_2S: Eu particle layer mixed in either epoxy or PDMS (Polydimethylsiloxane). Two layers are coated on the rod sensor while they had layered one over the other in the implant plate sensor. The polyacrylamide hydrogels are reported to be widely used in the biomedical field[78], drug delivery and biosensor fluids.[79] Due to its bioinert and hydrophilic properties, it is generally used in contact lenses.[80,81] The intertwined and separately crosslinked alginate and polyacrylamide triggerable tough hydrogels were tested for lumefantrine (antimalarial drug), in vivo use in Yorkshire pig animal models.[82] Risbud et al studied a polyacrylamide-Chitosan hydrogels for biocompatibility and sustained antibiotic release studies. The hydrogel showed no cytotoxic effects on NIH3T3 and HeLa cells in extract concentrations of 10-40%, but in 60 % of extract concentrations determined by MTT and neutral red assay for some degree, and some other studies showed the biocompatibility using human sera.[83,84] Unreacted monomers, pH sensitive dye and photo-initiator have a possibility of leaching out from the matrix but concentration is reduced given sufficient UV exposure as the photo-initiator and monomers react and are consumed. After preparation of the sensors, they were

pre-leached, washed several times with water and equilibrated in pH 7.4 buffer before implantation to minimize the toxicity that may arise from potential leaching of constituents.

The scintillator film is prepared by incorporating the particles in either epoxy or PDMS. Our group has previously studied the biocompatibility/cytotoxicity of pre leached vs non-pre leached scintillator particle incorporated epoxy coatings using fibroblasts L929 Cells (T192755Z). It indicated that epoxy caused no significant toxicity on the cell viability. These observations are comparable with the studies that are reported in the literature. Bagheri et al reports a study conducted to experiment cytotoxicity of an epoxy composite material for bone fracture plate applications and observed acceptable biocompatibility.[85] Ali et al. reports a similar study on biocompatibility of carbon fibre-reinforced epoxy resin bone plates which showed no cytotoxicity based on small animal implantation and tissue cultures.[86] The scintillator particles in PDMS was able to leach out by incubation in 1M sulfuric acid for 5 days.[38] In addition, the Gadolinium Oxysulfide nanoparticles are widely used in in vivo biomedical imaging such as 1) Magnetic Resonance Imaging (MRI), 2) X-ray Computed Tomography (CT) and 3) Photoluminescence Imaging. Santelli et al. report on Gd_2O_2S: Eu nanoparticles administered intravenously were almost insoluble in pure water and human plasma and tolerated up to 400 mg/kg.[87] Moreover, the amount of Gd_2O_2S: Eu in a epoxy sensor is ~44 mg/ cm^2 less than the recommended dose (0.1 mmol/ kg) of contrast agent in MRI for gadolinium chelates.[88]

1.6.2 Hydromechanical sensor

The biomechanical sensor has two parts to it. The stainless-steel mechanical lever and fluidic device made of acrylic. Stainless steel is frequently used in biomedical applications, and polyacrylates are a well-known biocompatible material for biomedical applications.[89] The radiopaque fluid incorporated inside the fluidic device is Cesium Acetate (85 Wt%). There is little toxicological information available on Cesium Acetate. However, the acute oral toxicities (LD50) for Sodium acetate and Sodium chloride are 3.5 g/kg and 3.75 g/kg, respectively, while that of Cesium chloride is 1.5 g/kg.[90,91] This indicates that the cesium segment of the compound is governing the toxicity of the solution. In the fluidic sensor itself, a minimal volume of Cesium acetate is accommodating (diameter of the fluid reservoir being 7 mm, the volume is ~ 0.077 cm^3). Therefore, the corresponding amount of Cesium acetate (0.18 g) that we are working is significantly less than the toxicity levels and safe for *in vivo* use. While developing biomechanical and biochemical sensors, we paid close attention to the biocompatibility of the materials used for in vivo use. Moreover, we haven't observed any toxicity caused by the chemical sensors for the animals during the studies. We always choose non-toxic materials for every possible occasion. But whenever we are limited by the other factors of fabricating the optimized sensors, we had to use the materials with minimal reported toxicity, or we have taken measures to reduce toxicity before implantation of the sensors (by pre leaching of the hydrogels, by sealing the fluidic sensor properly etc).

1.7 Introduction to thesis chapters

This dissertation describes a biochemical sensor and biomechanical sensor for monitoring implant associated infections in the intramedullary canal and monitoring stiffness of a fractured healing tibia. These studies address the two major compilations in the fracture healing process: infections associated with the orthopedic implants and nonunion/delayed union. These can be inter-related complications because nonunion of the fractures can be resulted in from infection related implant loosening. Additionally, the approaches are related in that they both involve implanted sensors and X-rays; however, they differ in that the infection sensors use optical indicator dyes and X-ray excited optical luminescence while the mechanical sensors use radio dense fluid and X-rays for signal detection.

Chapter 1 Introduces the dissertation and its' chapters. Chapter 2 discusses the X-ray Excited luminescence Imaging (XELCI) technique which enables mapping of biochemical information of implant associated infection. It discusses the working principle, instrumentation, imaging procedure, spatial resolution, and its' application in chemical imaging. Chapter 3 reports the rabbit study on "Non-invasive imaging of chemical changes associated with intramedullary canal infections via XELCI". It shows a detailed description of the pH imaging of the intramedullary canal carried out on one control rabbit model and two infected rabbit models via XELCI. The study on the fluidic sensor for monitoring stiffness of a fractured healing bone is described in Chapter 4. Chapter 5 is on the conclusion of the two main projects which I focused on my graduate research and future work that can be carried out to address the current issues and optimize the sensors.

1.8 References

(1) Gimeno, M.; Pinczowski, P.; Pérez, M.; Giorello, A.; Martínez, M. Á.; Santamaría, J.; Arruebo, M.; Luján, L. A Controlled Antibiotic Release System to Prevent Orthopedic-Implant Associated Infections: An in Vitro Study. *European Journal of Pharmaceutics and Biopharmaceutics* **2015**, *96*, 264–271. https://doi.org/10.1016/j.ejpb.2015.08.007.

(2) Kirby, J. P.; Mazuski, J. E. Prevention of Surgical Site Infection. *Surgical Clinics of North America* **2009**, *89* (2), 365–389.

(3) Arciola, C. R.; Alvi, F. I.; An, Y. H.; Campoccia, D.; Montanaro, L. Implant Infection and Infection Resistant Materials: A Mini Review. *Int J Artif Organs* **2005**, *28* (11), 1119–1125. https://doi.org/10.1177/039139880502801109.

(4) Kanakaris, N.; Gudipati, S.; Tosounidis, T.; Harwood, P.; Britten, S.; Giannoudis, P. The Treatment of Intramedullary Osteomyelitis of the Femur and Tibia Using the Reamer–Irrigator–Aspirator System and Antibiotic Cement Rods. *The bone & joint journal* **2014**, *96* (6), 783–788.

(5) Berebichez-Fridman, R. An Intramedullary Nail Coated with Antibiotic and Growth Factor Nanoparticles: An Individualized State-of-the-Art Treatment for Chronic Osteomyelitis with Bone Defects. *Medical Hypotheses* **2017**, 6.

(6) Pineda, C.; Vargas, A.; Rodríguez, A. V. Imaging of Osteomyelitis: Current Concepts. *Infectious Disease Clinics of North America* **2006**, *20* (4), 789–825. https://doi.org/10.1016/j.idc.2006.09.009.

(7) Inzana, J. A.; Schwarz, E. M.; Kates, S. L.; Awad, H. A. Biomaterials Approaches to Treating Implant-Associated Osteomyelitis. *Biomaterials* **2016**, *81*, 58–71. https://doi.org/10.1016/j.biomaterials.2015.12.012.

(8) Trampuz, A.; Zimmerli, W. Diagnosis and Treatment of Infections Associated with Fracture-Fixation Devices. *Injury* **2006**, *37* (2), S59–S66. https://doi.org/10.1016/j.injury.2006.04.010.

(9) Widmer, A. F. New Developments in Diagnosis and Treatment of Infection in Orthopedic Implants. *CLIN INFECT DIS* **2001**, *33* (s2), S94–S106. https://doi.org/10.1086/321863.

(10) Bryers, J. D. Medical Biofilms. *Biotechnol. Bioeng.* **2008**, *100* (1), 1–18. https://doi.org/10.1002/bit.21838.

(11) Vertes, A.; Hitchins, V.; Phillips, K. S. Analytical Challenges of Microbial Biofilms on Medical Devices. *Anal. Chem.* **2012**, *84* (9), 3858–3866. https://doi.org/10.1021/ac2029997.

(12) Renick, P.; Tang, L. Device-Related Infections. In *Racing for the Surface*; Li, B., Moriarty, T. F., Webster, T., Xing, M., Eds.; Springer International Publishing: Cham, 2020; pp 171–188. https://doi.org/10.1007/978-3-030-34475-7_7.

(13) Branda, S. S.; Vik, Å.; Friedman, L.; Kolter, R. Biofilms: The Matrix Revisited. *Trends in Microbiology* **2005**, *13* (1), 20–26. https://doi.org/10.1016/j.tim.2004.11.006.

(14) Whitchurch, C. B.; Tolker-Nielsen, T.; Ragas, P. C.; Mattick, J. S. Extracellular DNA Required for Bacterial Biofilm Formation. *Science* **2002**, *295* (5559), 1487–1487. https://doi.org/10.1126/science.295.5559.1487.

(15) Flemming, H.-C.; Wingender, J. The Biofilm Matrix. *Nat Rev Microbiol* **2010**, *8* (9), 623–633. https://doi.org/10.1038/nrmicro2415.

(16) Flemming, H.-C.; Wingender, J.; Szewzyk, U.; Steinberg, P.; Rice, S. A.; Kjelleberg, S. Biofilms: An Emergent Form of Bacterial Life. *Nat Rev Microbiol* **2016**, *14* (9), 563–575. https://doi.org/10.1038/nrmicro.2016.94.

(17) Tsang, S. T. J.; Simpson, A. H. R. W. Pathogenesis of Biomaterial-Associated Infection. In *Racing for the Surface*; Li, B., Moriarty, T. F., Webster, T., Xing, M., Eds.; Springer International Publishing: Cham, 2020; pp 109–169. https://doi.org/10.1007/978-3-030-34475-7_6.

(18) Stewart, P. S.; Franklin, M. J. Physiological Heterogeneity in Biofilms. *Nat Rev Microbiol* **2008**, *6* (3), 199–210. https://doi.org/10.1038/nrmicro1838.

(19) McLean, J. S.; Ona, O. N.; Majors, P. D. Correlated Biofilm Imaging, Transport and Metabolism Measurements via Combined Nuclear Magnetic Resonance and Confocal Microscopy. *ISME J* **2008**, *2* (2), 121–131. https://doi.org/10.1038/ismej.2007.107.

(20) Glaudemans, A. W. J. M.; Bosch, P.; Slart, R. H. J. A.; IJpma, F. F. A.; Govaert, G. A. M. Diagnosing Fracture-Related Infections: Can We Optimize Our Nuclear Imaging Techniques? *Eur J Nucl Med Mol Imaging* **2019**, *46* (8), 1583–1587. https://doi.org/10.1007/s00259-019-04378-5.

(21) Radovic-Moreno, A. F.; Lu, T. K.; Puscasu, V. A.; Yoon, C. J.; Langer, R.; Farokhzad, O. C. Surface Charge-Switching Polymeric Nanoparticles for Bacterial Cell Wall-Targeted Delivery of Antibiotics. *ACS Nano* **2012**, *6* (5), 4279–4287. https://doi.org/10.1021/nn3008383.

(22) Hunter, R. C.; Beveridge, T. J. Application of a pH-Sensitive Fluoroprobe (C-SNARF-4) for PH Microenvironment Analysis in Pseudomonas Aeruginosa Biofilms. *APPL. ENVIRON. MICROBIOL.* **2005**, *71*, 10.

(23) Fulaz, S.; Hiebner, D.; Barros, C. H. N.; Devlin, H.; Vitale, S.; Quinn, L.; Casey, E. Ratiometric Imaging of the in Situ pH Distribution of Biofilms by Use of Fluorescent Mesoporous Silica Nanosensors. *ACS Appl. Mater. Interfaces* **2019**, *11* (36), 32679–32688. https://doi.org/10.1021/acsami.9b09978.

(24) Lardner, A. The Effects of Extracellular pH on Immune Function. 9.

(25) Shen, Y.; Liu, W.; Wen, C.; Pan, H.; Wang, T.; Darvell, B. W.; Lu, W. W.; Huang, W. Bone Regeneration: Importance of Local PH—Strontium-Doped Borosilicate Scaffold. *J. Mater. Chem.* **2012**, *22* (17), 8662. https://doi.org/10.1039/c2jm16141a.

(26) Kolar, P.; Gaber, T.; Perka, C.; Duda, G. N.; Buttgereit, F. Human Early Fracture Hematoma Is Characterized by Inflammation and Hypoxia. *Clinical Orthopaedics & Related Research* **2011**, *469* (11), 3118–3126. https://doi.org/10.1007/s11999-011-1865-3.

(27) Claes, L.; Recknagel, S.; Ignatius, A. Fracture Healing under Healthy and Inflammatory Conditions. *Nat Rev Rheumatol* **2012**, *8* (3), 133–143. https://doi.org/10.1038/nrrheum.2012.1.

(28) Erra Díaz, F.; Dantas, E.; Geffner, J. Unravelling the Interplay between Extracellular Acidosis and Immune Cells. *Mediators of Inflammation* **2018**, *2018*, 1–11. https://doi.org/10.1155/2018/1218297.

(29) Anderson, J. M.; Rodriguez, A.; Chang, D. T. Foreign Body Reaction to Biomaterials. *Seminars in Immunology* **2008**, *20* (2), 86–100. https://doi.org/10.1016/j.smim.2007.11.004.

(30) Esmonde-White, K. A.; Esmonde-White, F. W. L.; Holmes, C. M.; Morris, M. D.; Roessler, B. J. Alterations to Bone Mineral Composition as an Early Indication of Osteomyelitis in the Diabetic Foot. *Diabetes Care* **2013**, *36* (11), 3652–3654. https://doi.org/10.2337/dc13-0510.

(31) Konttinen, Y. T.; Takagi, M.; Mandelin, J.; Lassus, J.; Salo, J.; Ainola, M.; Li, T.-F.; Virtanen, I.; Liljeström, M.; Sakai, H.; Kobayashi, Y.; Sorsa, T.; Lappalainen, R.; Demulder, A.; Santavirta, S. Acid Attack and Cathepsin K in Bone Resorption Around Total Hip Replacement Prosthesis. *J Bone Miner Res* **2001**, *16* (10), 1780–1786. https://doi.org/10.1359/jbmr.2001.16.10.1780.

(32) Dansby-Sparks, R. N.; Jin, J.; Mechery, S. J.; Sampathkumaran, U.; Owen, T. W.; Yu, B. D.; Goswami, K.; Hong, K.; Grant, J.; Xue, Z.-L. Fluorescent-Dye-Doped Sol− Gel Sensor for Highly Sensitive Carbon Dioxide Gas Detection below Atmospheric Concentrations. *Analytical chemistry* **2010**, *82* (2), 593–600.

(33) Li, Z.; Liang, R.; Liu, W.; Yan, D.; Wei, M. A Dual-Stimuli-Responsive Fluorescent Switch Ultrathin Film. *Nanoscale* **2015**, *7* (40), 16737–16743.

(34) Yang, Y.; Wang, K.-Z.; Yan, D. Ultralong Persistent Room Temperature Phosphorescence of Metal Coordination Polymers Exhibiting Reversible PH-Responsive Emission. *ACS Appl. Mater. Interfaces* **2016**, *8* (24), 15489–15496. https://doi.org/10.1021/acsami.6b03956.

(35) Zhang, Y.; Li, S.; Pan, G.; Yang, H.; Qile, M.; Chen, J.; Song, Q.; Yan, D. Stretchable Nanofibrous Membranes for Colorimetric/Fluorometric HCl Sensing: Highly Sensitive Charge-Transfer Excited State. *Sensors and Actuators B: Chemical* **2018**, *254*, 785–794.

(36) Wang, F.; Widejko, R. G.; Yang, Z.; Nguyen, K. T.; Chen, H.; Fernando, L. P.; Christensen, K. A.; Anker, J. N. Surface-Enhanced Raman Scattering Detection of PH with Silica-Encapsulated 4-Mercaptobenzoic Acid-Functionalized Silver Nanoparticles. *Analytical chemistry* **2012**, *84* (18), 8013–8019.

(37) Chen, H.; Qi, B.; Moore, T.; Wang, F.; Colvin, D. C.; Sanjeewa, L. D.; Gore, J. C.; Hwu, S.; Mefford, O. T.; Alexis, F. Multifunctional Yolk-in-Shell Nanoparticles for PH-triggered Drug Release and Imaging. *Small* **2014**, *10* (16), 3364–3370.

(38) Wang, F.; Raval, Y.; Chen, H.; Tzeng, T. J.; DesJardins, J. D.; Anker, J. N. Development of Luminescent PH Sensor Films for Monitoring Bacterial Growth through Tissue. *Advanced healthcare materials* **2014**, *3* (2), 197–204.

(39) Mahata, M. K.; Bae, H.; Lee, K. T. Upconversion Luminescence Sensitized PH-Nanoprobes. *Molecules* **2017**, *22* (12), 2064.

(40) Gao, R.; Fang, X.; Yan, D. Recent Developments in Stimuli-Responsive Luminescent Films. *J. Mater. Chem. C* **2019**, *7* (12), 3399–3412. https://doi.org/10.1039/C9TC00348G.

(41) van der Bruggen, W.; Bleeker-Rovers, C. P.; Boerman, O. C.; Gotthardt, M.; Oyen, W. J. G. PET and SPECT in Osteomyelitis and Prosthetic Bone and Joint Infections: A Systematic Review. *Seminars in Nuclear Medicine* **2010**, *40* (1), 3–15. https://doi.org/10.1053/j.semnuclmed.2009.08.005.

(42) Frangioni, J. In Vivo Near-Infrared Fluorescence Imaging. *Current Opinion in Chemical Biology* **2003**, *7* (5), 626–634. https://doi.org/10.1016/j.cbpa.2003.08.007.

(43) Batool, S.; Nisar, M.; Mangini, F.; Frezza, F.; Fazio, E. Scattering of Light from the Systemic Circulatory System. *Diagnostics* **2020**, *10* (12), 1026. https://doi.org/10.3390/diagnostics10121026.

(44) Steinke, J. M.; Shepherd, A. P. Comparison of Mie Theory and the Light Scattering of Red Blood Cells. *Appl. Opt.* **1988**, *27* (19), 4027. https://doi.org/10.1364/AO.27.004027.

(45) Farrell, T. J.; Patterson, M. S.; Wilson, B. A Diffusion Theory Model of Spatially Resolved, Steady-state Diffuse Reflectance for the Noninvasive Determination of Tissue Optical Properties in Vivo. *Medical physics* **1992**, *19* (4), 879–888.

(46) Shimizu, K.; Tochio, K.; Kato, Y. Improvement of Transcutaneous Fluorescent Images with a Depth-Dependent Point-Spread Function. *Appl. Opt.* **2005**, *44* (11), 2154. https://doi.org/10.1364/AO.44.002154.

(47) Smith, A. M.; Mancini, M. C.; Nie, S. Second Window for in Vivo Imaging. *Nature Nanotech* **2009**, *4* (11), 710–711. https://doi.org/10.1038/nnano.2009.326.

(48) Weissleder, R. A Clearer Vision for in Vivo Imaging. *Nat Biotechnol* **2001**, *19* (4), 316–317. https://doi.org/10.1038/86684.

(49) Taroni, P.; Pifferi, A.; Torricelli, A.; Comelli, D.; Cubeddu, R. In Vivo Absorption and Scattering Spectroscopy of Biological Tissues. *Photochem. Photobiol. Sci.* **2003**, *2* (2), 124. https://doi.org/10.1039/b209651j.

(50) Uzair, U.; Benza, D.; Behrend, C. J.; Anker, J. N. Noninvasively Imaging PH at the Surface of Implanted Orthopedic Devices with X-Ray Excited Luminescence Chemical Imaging. *ACS Sens.* **2019**, *4* (9), 2367–2374. https://doi.org/10.1021/acssensors.9b00962.

(51) Lister, T.; Wright, P. A.; Chappell, P. H. Optical Properties of Human Skin. *J. Biomed. Opt* **2012**, *17* (9), 0909011. https://doi.org/10.1117/1.JBO.17.9.090901.

(52) Imanishi, Y.; Lodowski, K. H.; Koutalos, Y. Two-Photon Microscopy: Shedding Light on the Chemistry of Vision. *Biochemistry* **2007**, *46* (34), 9674–9684. https://doi.org/10.1021/bi701055g.

(53) Grinstein, S.; Swallow, C. J.; Rotstein, O. D. Regulation of Cytoplasmic PH in Phagocytic Cell Function and Dysfunction. *Clinical Biochemistry* **1991**, *24* (3), 241–247. https://doi.org/10.1016/0009-9120(91)80014-T.

(54) Stewart, P. S.; William Costerton, J. Antibiotic Resistance of Bacteria in Biofilms. *The Lancet* **2001**, *358* (9276), 135–138. https://doi.org/10.1016/S0140-6736(01)05321-1.

(55) Vroom, J. M.; Grauw, K. J. D.; Gerritsen, H. C.; Bradshaw, D. J.; Marsh, P. D.; Watson, G. K.; Birmingham, J. J.; Allison, C. Depth Penetration and Detection of PH Gradients in Biofilms by Two-Photon Excitation Microscopy. *APPL. ENVIRON. MICROBIOL.* **1999**, *65*, 10.

(56) Hidalgo, G.; Burns, A.; Herz, E.; Hay, A. G.; Houston, P. L.; Wiesner, U.; Lion, L. W. Functional Tomographic Fluorescence Imaging of PH Microenvironments in Microbial Biofilms by Use of Silica Nanoparticle Sensors. *Appl Environ Microbiol* **2009**, *75* (23), 7426–7435. https://doi.org/10.1128/AEM.01220-09.

(57) Allan, V. J. M.; Macaskie, L. E.; Callow, M. E. Development of a PH Gradient within a Biofilm Is Dependent upon the Limiting Nutrient. 7.

(58) Wang, Z.; Deng, H.; Chen, L.; Xiao, Y.; Zhao, F. In Situ Measurements of Dissolved Oxygen, PH and Redox Potential of Biocathode Microenvironments Using Microelectrodes. *Bioresource Technology* **2013**, *132*, 387–390. https://doi.org/10.1016/j.biortech.2012.11.026.

(59) Xiao, Y.; Wu, S.; Yang, Z.-H.; Wang, Z.-J.; Yan, C.-Z.; Zhao, F. In Situ Probing the Effect of Potentials on the Microenvironment of Heterotrophic Denitrification Biofilm with Microelectrodes. *Chemosphere* **2013**, *93* (7), 1295–1300. https://doi.org/10.1016/j.chemosphere.2013.06.065.

(60) Nakata, E.; Yukimachi, Y.; Nazumi, Y.; Uwate, M.; Maseda, H.; Uto, Y.; Hashimoto, T.; Okamoto, Y.; Hori, H.; Morii, T. A Novel Strategy to Design Latent Ratiometric Fluorescent PH Probes Based on Self-Assembled SNARF Derivatives. *RSC Adv.* **2014**, *4* (1), 348–357. https://doi.org/10.1039/C3RA43928C.

(61) Villano, D.; Romdhane, F.; Irrera, P.; Consolino, L.; Anemone, A.; Zaiss, M.; Dastrù, W.; Longo, D. L. A Fast Multislice Sequence for 3D MRI-CEST PH Imaging. *Magnetic resonance in medicine* **2021**, *85* (3), 1335–1349.

(62) Uzair, U.; Johnson, C.; Beladi-Behbahani, S.; Rajamanthrilage, A. C.; Raval, Y. S.; Benza, D.; Ranasinghe, M.; Schober, G.; Tzeng, T.-R. J.; Anker, J. N. Conformal Coating of Orthopedic Plates with X-Ray Scintillators and PH Indicators for X-Ray Excited Luminescence Chemical Imaging through Tissue. *ACS Appl. Mater. Interfaces* **2020**, *12* (47), 52343–52353. https://doi.org/10.1021/acsami.0c13707.

(63) Morshed, S. Current Options for Determining Fracture Union. *Advances in Medicine* **2014**, *2014*, 1–12. https://doi.org/10.1155/2014/708574.

(64) Claes, L. E.; Cunningham, J. L. Monitoring the Mechanical Properties of Healing Bone. *Clinical Orthopaedics and Related Research®* **2009**, *467* (8), 1964–1971. https://doi.org/10.1007/s11999-009-0752-7.

(65) Einhorn, T. A. Enhancement of Fracture-Healing.: *The Journal of Bone & Joint Surgery* **1995**, *77* (6), 940–956. https://doi.org/10.2106/00004623-199506000-00016.

(66) Hak, D. J.; Fitzpatrick, D.; Bishop, J. A.; Marsh, J. L.; Tilp, S.; Schnettler, R.; Simpson, H.; Alt, V. Delayed Union and Nonunions: Epidemiology, Clinical Issues, and Financial Aspects. *Injury* **2014**, *45*, S3–S7. https://doi.org/10.1016/j.injury.2014.04.002.

(67) Richardson, J. B.; Kenwright, J.; Cunningham, J. L. Fracture Stiffness Measurement in the Assessment and Management of Tibial Fractures. *Clinical Biomechanics* **1992**, *7* (2), 75–79. https://doi.org/10.1016/0268-0033(92)90018-Y.

(68) Claes, L.; Grass, R.; Schmickal, T.; Kisse, B.; Eggers, C.; Gerngro�, H.; Mutschler, W.; Arand, M.; Wintermeyer, T.; Wentzensen, A. Monitoring and Healing Analysis of 100 Tibial Shaft Fractures. *Langenbeck's Archives of Surgery* **2002**, *387* (3–4), 146–152. https://doi.org/10.1007/s00423-002-0306-x.

(69) Seide, K.; Aljudaibi, M.; Weinrich, N.; Kowald, B.; Jürgens, C.; Müller, J.; Faschingbauer, M. Telemetric Assessment of Bone Healing with an Instrumented Internal Fixator: A Preliminary Study. *The Journal of Bone and Joint Surgery. British volume* **2012**, *94-B* (3), 398–404. https://doi.org/10.1302/0301-620X.94B3.27550.

(70) Stoffel, K.; Klaue, K.; Perren, S. M. Functional Load of Plates in Fracture Fixation in Vivo and Its Correlate in Bone Healing. *Injury* **2000**, *31*, 37–86. https://doi.org/10.1016/S0020-1383(00)80042-X.

(71) Gattiker, F.; Umbrecht, F.; Neuenschwander, J.; Sennhauser, U.; Hierold, C. Novel Ultrasound Read-out for a Wireless Implantable Passive Strain Sensor (WIPSS). *Sensors and Actuators A: Physical* **2008**, *145–146*, 291–298. https://doi.org/10.1016/j.sna.2007.09.003.

(72) Hammer, R. R.; Hammerby, S.; Lindholm, B. Accuracy of Radiologic Assessment of Tibial Shaft Fracture Union in Humans. *Clinical orthopaedics and related research* **1985**, No. 199, 233–238.

(73) Blokhuis, T. J.; de Bruine, J. H. D.; Bramer, J. A. M.; den Boer, F. C.; Bakker, F. C.; Patka, P.; Haarman, H. J. Th. M.; Manoliu, R. A. The Reliability of Plain Radiography in Experimental Fracture Healing. *Skeletal Radiology* **2001**, *30* (3), 151–156. https://doi.org/10.1007/s002560000317.

(74) Melnikov, P.; Zanoni, L. Z. Clinical Effects of Cesium Intake. *Biological Trace Element Research* **2010**, *135* (1–3), 1–9. https://doi.org/10.1007/s12011-009-8486-7.

(75) Hosseinpour, S.; Gaudin, A.; Peters, O. A. A Critical Analysis of Research Methods and Experimental Models to Study Biocompatibility of Endodontic Materials. *Int Endodontic J* **2022**, *55* (S2), 346–369. https://doi.org/10.1111/iej.13701.

(76) Hermawan, H.; Ramdan, D.; Djuansjah, J. R. Metals for Biomedical Applications. *Biomedical engineering-from theory to applications* **2011**, *1*, 411–430.

(77) Hacker, M. C.; Mikos, A. G. Chapter 33 - Synthetic Polymers. In *Principles of Regenerative Medicine (Second Edition)*; Atala, A., Lanza, R., Thomson, J. A., Nerem, R., Eds.; Academic Press: San Diego, 2011; pp 587–622. https://doi.org/10.1016/B978-0-12-381422-7.10033-1.

(78) *Hydrogels for Medical and Related Applications*; Andrade, J. D., Ed.; ACS Symposium Series; AMERICAN CHEMICAL SOCIETY: WASHINGTON, D. C., 1976; Vol. 31. https://doi.org/10.1021/bk-1976-0031.

(79) Tsou, Y.-H.; Khoneisser, J.; Huang, P.-C.; Xu, X. Hydrogel as a Bioactive Material to Regulate Stem Cell Fate. *Bioactive Materials* **2016**, *1* (1), 39–55. https://doi.org/10.1016/j.bioactmat.2016.05.001.

(80) Fernández, E.; López, D.; López-Cabarcos, E.; Mijangos, C. Viscoelastic and Swelling Properties of Glucose Oxidase Loaded Polyacrylamide Hydrogels and the Evaluation of Their Properties as Glucose Sensors. *Polymer* **2005**, *46* (7), 2211–2217. https://doi.org/10.1016/j.polymer.2004.12.039.

(81) Darnell, M. C.; Sun, J.-Y.; Mehta, M.; Johnson, C.; Arany, P. R.; Suo, Z.; Mooney, D. J. Performance and Biocompatibility of Extremely Tough Alginate/Polyacrylamide Hydrogels. *Biomaterials* **2013**, *34* (33), 8042–8048. https://doi.org/10.1016/j.biomaterials.2013.06.061.

(82) Liu, J.; Pang, Y.; Zhang, S.; Cleveland, C.; Yin, X.; Booth, L.; Lin, J.; Lucy Lee, Y.-A.; Mazdiyasni, H.; Saxton, S.; Kirtane, A. R.; Erlach, T. von; Rogner, J.; Langer, R.; Traverso, G. Triggerable Tough Hydrogels for Gastric Resident Dosage Forms. *Nat Commun* **2017**, *8* (1), 124. https://doi.org/10.1038/s41467-017-00144-z.

(83) Makarand V. Risbud, Ramesh R. Bhond. Polyacrylamide-Chitosan Hydrogels: In Vitro Biocompatibility and Sustained Antibiotic Release Studies. *Drug Delivery* **2000**, *7* (2), 69–75. https://doi.org/10.1080/107175400266623.

(84) Saraydin, D.; Karadağ, E.; Çaldiran, Y.; Güven, O. Nicotine-Selective Radiation-Induced Poly(Acrylamide/Maleic Acid) Hydrogels. *Radiation Physics and Chemistry* **2001**, *60* (3), 203–210. https://doi.org/10.1016/S0969-806X(00)00342-X.

(85) Bagheri, Z. S.; Giles, E.; El Sawi, I.; Amleh, A.; Schemitsch, E. H.; Zdero, R.; Bougherara, H. Osteogenesis and Cytotoxicity of a New Carbon Fiber/Flax/Epoxy Composite Material for Bone Fracture Plate Applications. *Materials Science and Engineering: C* **2015**, *46*, 435–442. https://doi.org/10.1016/j.msec.2014.10.042.

(86) Ali, M.; French, T.; Hastings, G.; Rae, T.; Rushton, N.; Ross, E.; Wynn-Jones, C. Carbon Fibre Composite Bone Plates. Development, Evaluation and Early Clinical Experience. *The Journal of bone and joint surgery. British volume* **1990**, *72* (4), 586–591.

(87) Santelli, J.; Lechevallier, S.; Calise, D.; Marsal, D.; Siegfried, A.; Vincent, M.; Martinez, C.; Cussac, D.; Mauricot, R.; Verelst, M. Multimodal Gadolinium Oxysulfide Nanoparticles for Bioimaging: A Comprehensive Biodistribution, Elimination and Toxicological Study. *Acta Biomaterialia* **2020**, *108*, 261–272. https://doi.org/10.1016/j.actbio.2020.03.013.

(88) Penfield, J. G.; Reilly, R. F. What Nephrologists Need to Know about Gadolinium. *Nat Rev Nephrol* **2007**, *3* (12), 654–668. https://doi.org/10.1038/ncpneph0660.

(89) Lumelsky, Y.; Lalush-Michael, I.; Levenberg, S.; Silverstein, M. S. A Degradable, Porous, Emulsion-templated Polyacrylate. *Journal of Polymer Science Part A: Polymer Chemistry* **2009**, *47* (24), 7043–7053.

(90) Ashokkumar, M.; Mason, T. J. Sonochemistry. *Kirk-Othmer Encyclopedia of Chemical Technology* **2000**.

(91) O'Neil, M. J. *The Merck Index: An Encyclopedia of Chemicals, Drugs, and Biologicals*; RSC Publishing, 2013.

CHAPTER 2

HIGH SPATIAL RESOLUTION IMAGING OF IMPLANT-ASSOCIATED INFECTIONS WITH XELCI (X-RAY EXCITED LUMINESCENCE CHEMICAL IMAGING)

2.1 Abstract

An imaging technique for high resolution optical detection of chemical information around implanted medical devices in combination with X-ray excitation is described. We describe XELCI as technique to noninvasively image chemical concentrations near the surface of implanted medical devices that are coated with chemically reporting surfaces. Our chemically responsive surface consists of two layers coated on implantable medical device; a pH sensitive layer (Bromothymol blue incorporated hydrogel) which is coated over a red-light emitting scintillator (Gd_2O_2S: Eu) layer for monitoring. A focused X-ray beam irradiates a spot on the implant and the red light generated by the scintillator (with 620 nm and 700 nm peaks) is transmitted through the sensing layer which alters the spectral ratio depending on the pH. An image is generated by scanning the X-ray beam across the implant and measuring the spectral ratio of light passing through the tissue point-by-point. This enables noninvasive, high spatial resolution, low background local pH imaging for studying implant associated infection biochemistry.

Some of the sections of this chapter material are published in the Journal of Visual Experiments titled as “High spatial resolution chemical imaging of implant-associated infections with X-ray Excited Luminescence Chemical Imaging (XELCI) through tissue”

2.2 Introduction

Since the discovery of X-rays in 1895,[1,2] biomedical imaging by radiography has evolved from diagnosis of fractures and detection of foreign bodies into more sophisticated techniques.[3–5] These advanced radiographic imaging techniques are not only limited to patient care but also focused on studying the biological functions to address major concerns in biomedicine. They are widely applied in detecting and diagnosis of pathologies in orthopedic implant-associated infections, non-unions, and related complications. For example, CT can be used to find bridging bone which could indicate that the fracture has united. Although these techniques are used frequently to acquire structural information of the surrounding bone and tissue at the orthopedic implant, they cannot provide biochemical information in the specific environment. Thus, we describe a novel technique, X-ray excited luminescence chemical imaging (XELCI), for high-resolution imaging of biochemical information noninvasively at the implant site.

Diagnosis of orthopedic implant associated infections is commonly carried out by one or combination of different means. Clinical observations (pain, swelling, redness, wound discharge etc) suggest the first signs of infection. Later, radiological and laboratory experiments are carried out to confirm the failure of progression of bone healing and identify the pathogenic organism.[6] Nuclear medicinal techniques such as computerized tomography (CT), magnetic resonance imaging (MRI), and radionucleotide methods (Single Photon Emission Computed Tomography (SPECT) and Positron Emission

Tomography (PET) are in use for better visualization of the infected implant and the associated infection. CT and MRI are advantageous in determining bone necrosis and soft tissue abnormalities respectively but cause interferences in close distance to the metal implants.[7] Different X-ray methodologies such as SPECT and PET in combination with radioisotope-labeled analytes as in vivo imaging contrast agents are widely utilized for the diagnosis of implant-associated osteomyelitis.[8] Current applications combine both data from CT scanning and labeling data from either SPECT or PET to generate anatomical information.[9]Although one or more of these imaging modalities are used for successful detection of infection, they are hardly capable of detecting the infections early and to avoid extra medical and surgical expenses. The main purpose of our imaging system is early detection of implant-associated infection and to monitor the course of infection during the treatment to evaluate the success of the treatments. The figure below shows our imaging technique's comparison to other available methods.

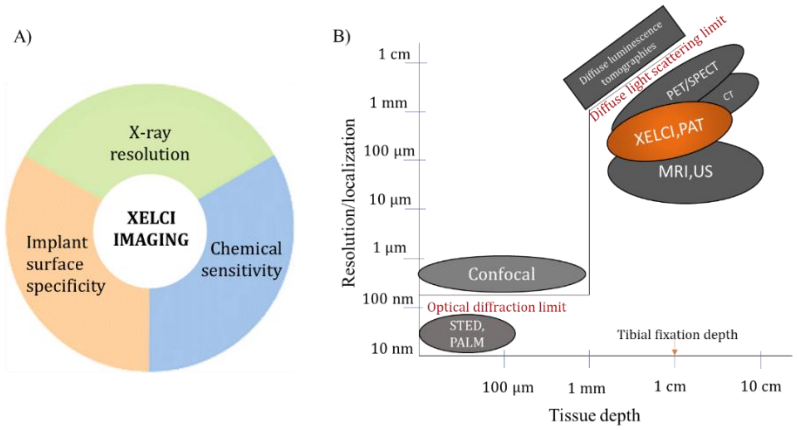

Figure 2.1: Characteristics of the XELCI imaging System. A) Three key features of XELCI. B) Comparison of XELCI imaging to other techniques. (Reproduced with the permission from Reference Rajamanthrilage et al, High Spatial Resolution Chemical Imaging of Implant-Associated Infections with X-ray Excited Luminescence Chemical Imaging Through Tissue. J. Vis. Exp. (Pending Publication), e64252, In-press (2022))

Three specific characteristics of our imaging technique are X-ray resolution, Implant surface specificity and chemical sensitivity. These characteristics of XELCI can be compared with the currently available imaging techniques for imaging orthopedic implant related infections. Once irradiated with X-rays, some phosphor particles generate near-IR (NIR) light that can travel long distances in tissue. These components (X-rays and NIR photons) of electromagnetic radiation are utilized in *in vivo* biomedical imaging as they can propagate through tissue in long distances.[10]

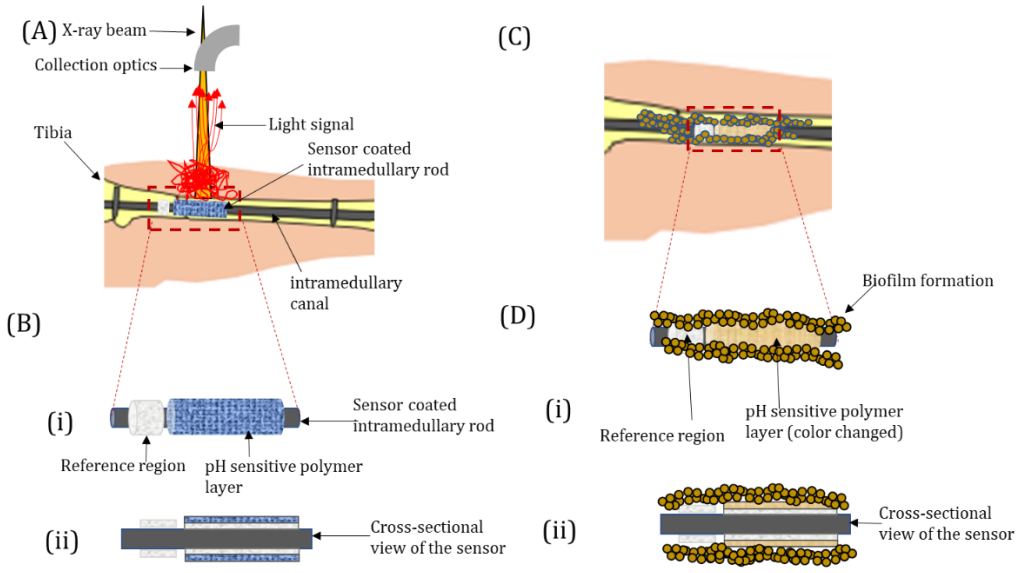

Figure 2.2: Schematic showing principle of XELCI imaging a) Schematic showing implant irradiated with focused X-ray beam and luminescence collected for detection; b) zoomed-in view of the scintillator and pH-sensitive film coated intramedullary rod sensor; c) at low pH caused by infection, intramedullary rod sensor turns from blue to yellow, while dye-free reference region is unchanged; d) zoomed-in view of intramedullary rod during an infection. (Reproduced with the permission from Reference Rajamanthrilage et al, High Spatial Resolution Chemical Imaging of Implant-Associated Infections with X-ray Excited Luminescence Chemical Imaging Through Tissue. J. Vis. Exp. (Pending Publication), e64252, In-press (2022))

XELCI (X-ray Excited Luminescence Chemical Imaging) is a novel imaging technique to acquire high spatial resolution chemical information optically near implanted medical devices in combination with X-ray excitation.[11] This technique involves both an implanted probe and a scanner. The probe contains X-ray scintillators that generate visible and NIR light when irradiated by X-rays. It has a chemically sensitive layer fabricated over the scintillator layer that affects the light intensity or spectrum. Once the implant is irradiated by a sequence of narrow, focused X-ray beam, scintillator particles generate visible light (620 nm and 700 nm) which passes through the pH sensitive layer modulating the luminescence spectrum depending on the pH of the surrounding environment. The transmitted light through tissue and bone is collected and the spectral ratio determines pH. The focused X-ray beam irradiates a point in the scintillator film, and a pH image is formed point-by-point by scanning the beam across the sensor. The chemically sensitive layer chosen for this application is Bromothymol Blue which has pH-dependent absorbance at 600 nm wavelength and almost constant (pH independent) absorbance at 700 nm light which overlaps with the scintillator emission (620 nm and 700 nm). Bromothymol Blue or Bromocresol green has a pK_a value in the pH range we are interested in monitoring implant-associated infections. During analysis of the pH microenvironment of bacterial biofilm with pH-sensitive fluorescent ratiometric dye, pH can vary between 5.6 (within the biofilm) and pH 7 (in the surrounding bulk fluid)[12]. Implanted probe also has a scintillator layer without the pH indicating dye which acts as a spatially distinct reference region. Moreover, the scintillator particles we use has prominent emissions at ~600 nm and ~700 nm wavelengths. The absorbance spectrum of the above dyes overlaps with the emission

spectrum of the Gd_2O_2S:Eu particles. These inorganic scintillator particles undergo sequence of steps once irradiated with X-rays to generate light. The particles will first absorb the X-rays and generate the primary electron and holes. Secondly, the primary electrons and holes will undergo relaxation by producing large number of secondary electrons, holes, photons, plasmons, and other electronic excitations. Then the thermalization of the low-energy secondary electrons (holes) produces e-h pairs with energy roughly in the range of band gap energy. The energy will be then transferred to the luminescent centers from the e-h pairs. Finally the luminescent centers will emit light in the visible range (red light).[13–15] The exciting X-rays and red/NIR luminescence photons are utilized in in vivo biomedical imaging as they can propagate through tissue.[16–20]

2.3 Instrumentation

Figure 2.3 below shows a schematic of the XELCI imaging system. Basic components of the imaging system are the X-ray excitation source with poly capillary optics, one piece acrylic light guide connecting to two photo multiplier tubes, the x, y, and z motorized stage (30 x 15 x 6 cm travel, Models: LTS300 and LTS150, Thorlabs Inc., Newton, NJ, USA for x and y axis and Motorized Linear Vertical Stage Model AT10-60, Motion Control, Smithtown, NY, USA for the z-stage) and the computer connected for data acquisition. The X-ray source, x,y,z stage, collection optics (elbow, light guide, PMTs) are in the X-ray proof enclosure while the X-ray controller, power source for PMTs, function generator connected to the DAQ board and computer are kept outside. The interlock at the front door of the enclosure works as an interlock with a push-button

normally open switch. If the door isn't fully closed (interlock switch is open), the X-ray source won't turn on, and it will automatically turn off the X-ray source if it is opened during operation. The motors can execute a continuous scan as well as it can be moved to any discrete location. The scan speed for y axis is usually 1-5 mm/sec while the step size in the x-axis can be chosen from 150 to 2000 μm. The parameters can be chosen depending on the required spatial resolution. Even exposure times are confirmed by consistent speed throughout a continuous scan.

While positioning the sample for imaging with XELCI, we use a laser cross head connected to polycapillary focusing optics with two intersecting line-shaped laser pointers at the 90° angle to align the elbow precisely underneath it. These lasers should be turned off prior to starting a scan to eliminate any unwanted light reaching the detector other than the light generated by the scintillators. In terms of distance, the user measures distance from tip of focusing optics to the top of the sample to be around 5-5.5 cm before initiating the experiment. This can be achieved either by raising the X-ray source manually, or by moving the stage up and down. For a live animal, or measurement through tissue, the same procedure is used, except we put the animal in with under anesthesia and run an isoflurane gas tube to ensure it says asleep. We monitor its temperature and pulse periodically and add additional bedding and tape to properly position the animal anatomy especially angle, and we estimate 5-5.5 cm focal position to be the depth of the implant rather than just using the distance to the top surface of the skin. We often take a plain X-ray image or course XELCI scan to ensure the correct location. For sensors not covered with tissue, we generally decrease the X-ray source current from the maximum of 600 uA at 50 kV to as

low as 15 uA to make sure the PMTs do not saturate. The X-ray source and its condition is periodically monitored by Clemson university Radiation Safety. The key for X-ray controller is only used by XELCI users and it is always kept away to prevent any accidental powering on/off. Also, the push button interlock at the front door of the XELCI enclosure should be carefully secured before turning on the X-ray. If the interlock isn't working correctly, the user won't be able to power on the X-ray and it will generate errors. Throughout the experiment while the X-ray is on, an orange light is turned to inform everyone the radiation source is powered-on.

The motors can execute a continuous scan as well as it can be move to any discrete location. Even exposure times are confirmed by consistent speed throughout a continuous scan. Once the focused X-ray beam is irradiated on the X-ray luminescence particles, the generated light will pass through the pH sensitive film. Depending on the pH of the film the light will be modulated. The tissue will then scatter and absorb part of the transmitted light and will increase as the tissue thickness increases. The escaped light from the tissue is collected with a one-piece acrylic light guide where a reflective aluminum 90°elbow is attached at the beginning. It will ensure the light is collimated as soon as light reaches the light guide. We also have attached a long pass blue light filter at the beginning of the elbow to ensure that only red light will pass through. The end of the one-piece acrylic light guide bifurcates into two streams leading to two different photo multiplier tubes (PMTs) (Model P25PC-16, SensTech, Surrey, UK). The PMTs are enclosed in a small light tight metal box which is in contact with a Thermoelectric cooler (ElectraCOOL Advanced thermoelectric cool plate, Pollock industries, White River, VT, USA) to cool down the PMTs to ~5°C. At

the beginning of one of the PMTs, we have attached a long pass filter to only measure 700 nm light. Therefore, we can calculate the 620 nm and 700 nm light separately. The PMTs are setup in photon counting\ mode and it generates transistor-transistor logic (TTL) pulses for each photon detected. A national instruments c-DAQ 9171 counts the pulses (saturation point 20 million pulses per second) using USB communication. After processing the collected data, two separate intensity maps are created. The final image is formed by taking a ratio of the signal wavelength intensity (620 nm) to the reference wavelength intensity (700 nm). Ratio measurements rather than taking absolute intensity counts will account for the variation in tissue thickness and optical collection efficiency.

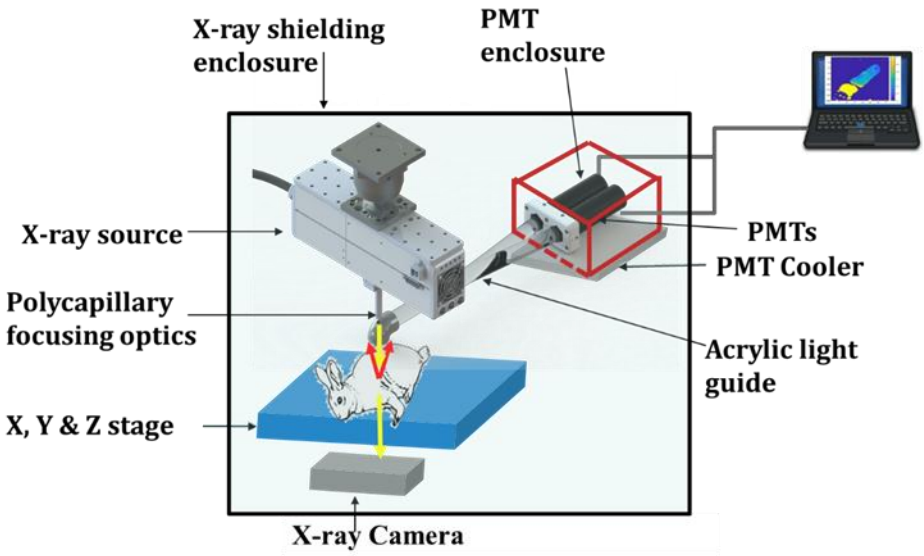

Figure 2.3: A schematic diagram showing parts of the XELCI imaging system. (Reproduced with the permission from Reference Rajamanthrilage et al, High Spatial Resolution Chemical Imaging of Implant-Associated Infections with X-ray Excited Luminescence Chemical Imaging Through Tissue. J. Vis. Exp. (Pending Publication), e64252, In-press (2022))

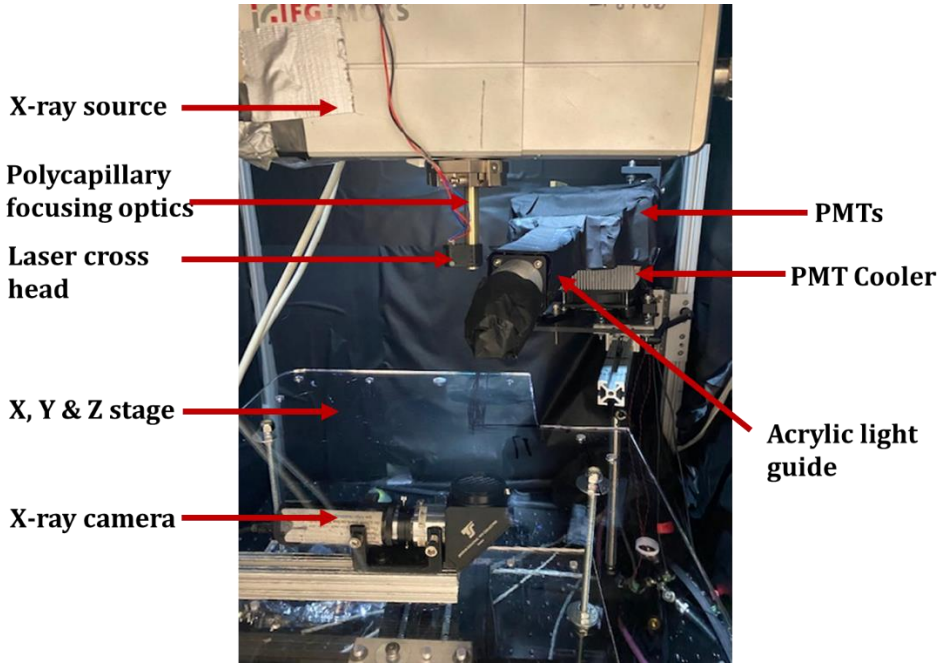

Figure 2.4: A photograph of the XELCI imaging system. (Reproduced with the permission from Reference Rajamanthrilage et al, High Spatial Resolution Chemical Imaging of Implant-Associated Infections with X-ray Excited Luminescence Chemical Imaging Through Tissue. J. Vis. Exp. (Pending Publication), e64252, In-press (2022))

LabVIEW graphic based programming language is used for controlling the imaging system and a basic flow chart of the operation is shown below. The program is first initialized by communicating with the x-y-z axis motorized stage. The x and y axis of the stage is moved to the desired original position. A background is recorded before scanning the sample to determine the dark counts from any light present in the environment other than the sample. The door for the enclosure is closed and X-ray interlock is secured before every scan. Once the sample is properly placed on the stage and the scan is ready to begin, X-ray source (iMOXS, Institute for Scientific Instruments GmbH, Berlin, Germany) with a polycapillary lens (~5 cm focal distance from capillary tip) is turned on at the desired

voltage and current. The y-axis is continuously recorded starting from the first row of the scan. During the scan, the number of counts per each wavelength of light and time since the previous motor position update is recorded. Time is recorded to account for any motor speed changes and hence the exposure time. Therefore, each pixel can be normalized to counts/second. The y axis motor scan to the end of the current row of the y axis and it returns to the starting position. Then the x axis motor increases its position by a step size defined by the user and scans the second row of the y axis. This process is cycled until the x axis motor reaches the specified width for the x direction. The user can control the scan size, motor speed and the motor starting positions. The step size will determine the size of the pixels in the final image of the y axis. Data will be processed by simple linear interpolation and will plot counts versus position while the motors are moving to the start position of the next row. The image will be displayed in real time on the computer screen during acquisition so that the user can validate the scan is imaging the area of interest of the target.

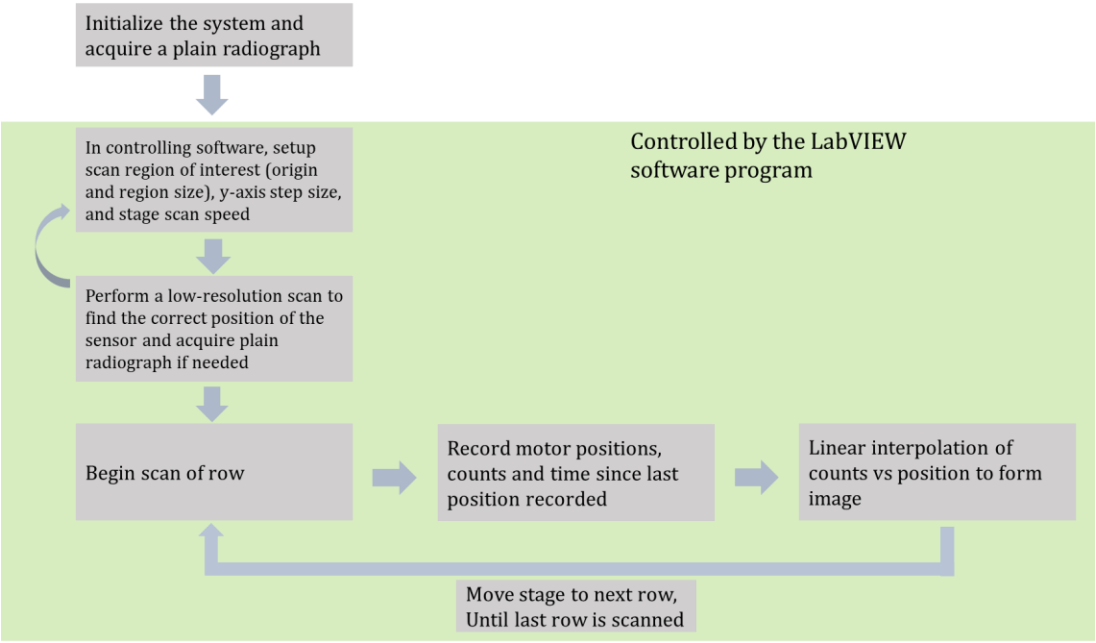

Figure 2.5: LabVIEW control scheme for the XELCI imaging system. (Reproduced with the permission from Reference Rajamanthrilage et al, High Spatial Resolution Chemical Imaging of Implant-Associated Infections with X-ray Excited Luminescence Chemical Imaging Through Tissue. J. Vis. Exp. (Pending Publication), e64252, In-press (2022))

2.4 Methods

2.4.1 X-ray Dosage Experiment

To determine the dosage of the X-ray source we have used the gaff chromic paper to scan a certain area under the focused X-ray beam. A piece of gaff chromic paper (GAFCHROMIC XR-RV3 Comparison Tablet) is placed on the stage as placing any other sample and scanned at 250 µm step size, 5 mm/sec scan speed and an area of 0.5 cm* 0.5

cm. After the scanning the color of the scanned area was compared to the color chart provided with the gaff chromic paper.

2.4.2 Comparison of XELCI technique with Plain radiography and Knife edge resolution experiment

A line target with four different line widths were laser cut from a piece of black cardboard. The line target contains 4 different line widths; 2 mm, 1 mm, 0.5 mm, and 0.2 mm. It was placed over a scintillator layer. XELCI imaging of the line target was carried out through 0 mm, 5 mm, and 10 mm porcine tissue. The 700 nm image is shown in Figure 6a, d and g.

To compare the XELCI imaging with plain radiography, three targets (Luck -metal target, pH sensitive gels at two different pHs and line target) were placed on a scintillator layer. The targets were first imaged with no tissue at 250 µm step size and 1mm/secspeed. The X-ray power for the no tissue experiment is 50 kV, 50 µA and the targets were imaged at 50 kV and 600 µA through 10 mm porcine tissue. Right after imaging a plain radiograph was also acquired on both occasions.

2.5 Results and Discussion

2.5.1 X-ray dosage experiment

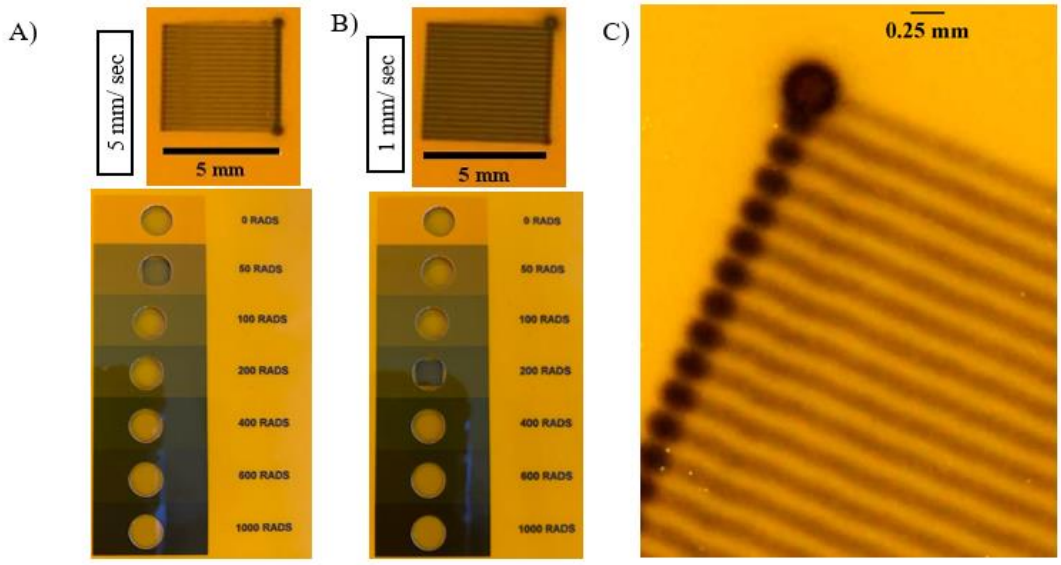

Figure 2.6: Exposure of gaffchromic paper for measuring X-ray Dose. A) The scanned area at 5 mm/sec speed and comparison of the color with the color chart. B) The scanned area at 1 mm/sec speed and comparison of the color with the color chart. C) The zoomed in view of the few lines of the scanned area.

2.5.2 Spatial Resolution

To compare the plain radiography vs. XELCI, three different targets were used for imaging with plain radiography and XELCI with and without tissue. The “Luck” sign (metal target), a line target with four different line widths and pH sensitive hydrogels at two different pHs (pH 6.5 and 7.5) were placed on top of a Gd_2O_2S:Eu particle film. As

shown in the figure 6 b) and e), only the metal target can be observed with plain radiography while in XELCI, all three targets can be seen with XELCI imaging. Moreover, the pH difference between two pH values which are different in one unit can be clearly visualized. Also, the line target with 4 different lines widths (Line widths, top to bottom: 2, 1, 0.5, and 0.2 mm) allowed us to determine the spatial resolution. In the images, the dark areas are where the light intensities are lower and bright areas are where the light intensities are higher. Figure 5 c) and f) shows that we can image complex writing on the metal target with and without tissue via XELCI.

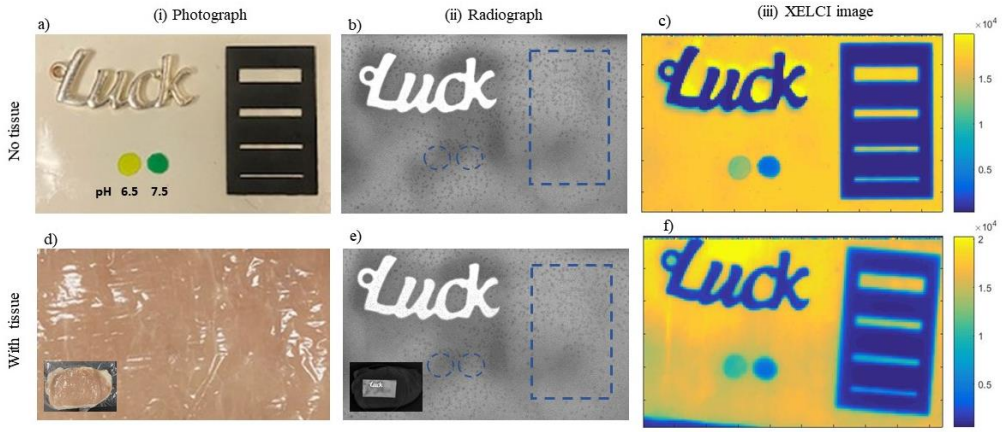

Figure 2.7: Plain radiography vs. functional radiography. (i) Images of three targets acquired using a digital camera, (ii) Plain radiography and XELCI imaging. (a) Photo with no tissue of the three targets on scintillator film. (b) Plain radiograph of the three targets with no tissue. (c) XELCI image of the three targets on scintillator film with no tissue. (d) Photo with tissue of the three targets on scintillator film. (e) Plain radiograph of the three targets with tissue. (f) XELCI image of the three targets on scintillator film with tissue.

To determine the spatial resolution of the XELCI imaging technique, we carried out a knife-edge resolution experiment. As X-ray has high penetration depth through tissue and minimum scattering, the spatial resolution is mainly limited by the width of the X-ray beam, with some additional broadening from light scattering and propagation within the scintillator film, indicator film and through thick tissue. A line target was prepared by laser cutting lines of defined width in a black paper (optically absorbing, 100 μm) and imaged with XELCI through tissue and without any tissue covering. The lines had a width of 2 mm, 1 mm, 0.5 mm, and 0.2 mm. A photograph of the line target placed on the scintillator film and the 620 nm intensity XELCI images of the target scanned with and without tissue (5 mm and 10 mm thick tissue) are shown in figure 5 along with the intensity plots. We can clearly see all the lines in the XELCI images for both with and without tissue. The signal is plotted as an intensity plot for the line drawn across the XELCI images in figure 6 B, E and H. The areas containing the cut-out lines in the paper allowed transmittance of optical signal as indicated by the peaks and the area that was covered with black paper did not allow the signal to pass (valleys in the intensity plot). To determine the knife edge resolution for 20–80% intensity transition, the falling edge of the 2 mm line peak was selected (zoomed in, figure 6 C, F, and I). The 20–80% intensity transition occurred over ~285 (±14.5) μm for without tissue and 475 ± (18) μm or 520± (33.5) μm with tissue. The spatial resolution should not vary with or without tissue as it is determined by the X-ray beam width and the observed slight difference could be due to positioning of the target as it appears to be the case in the XELCI image where the target might not be completely flat on the scintillator film.

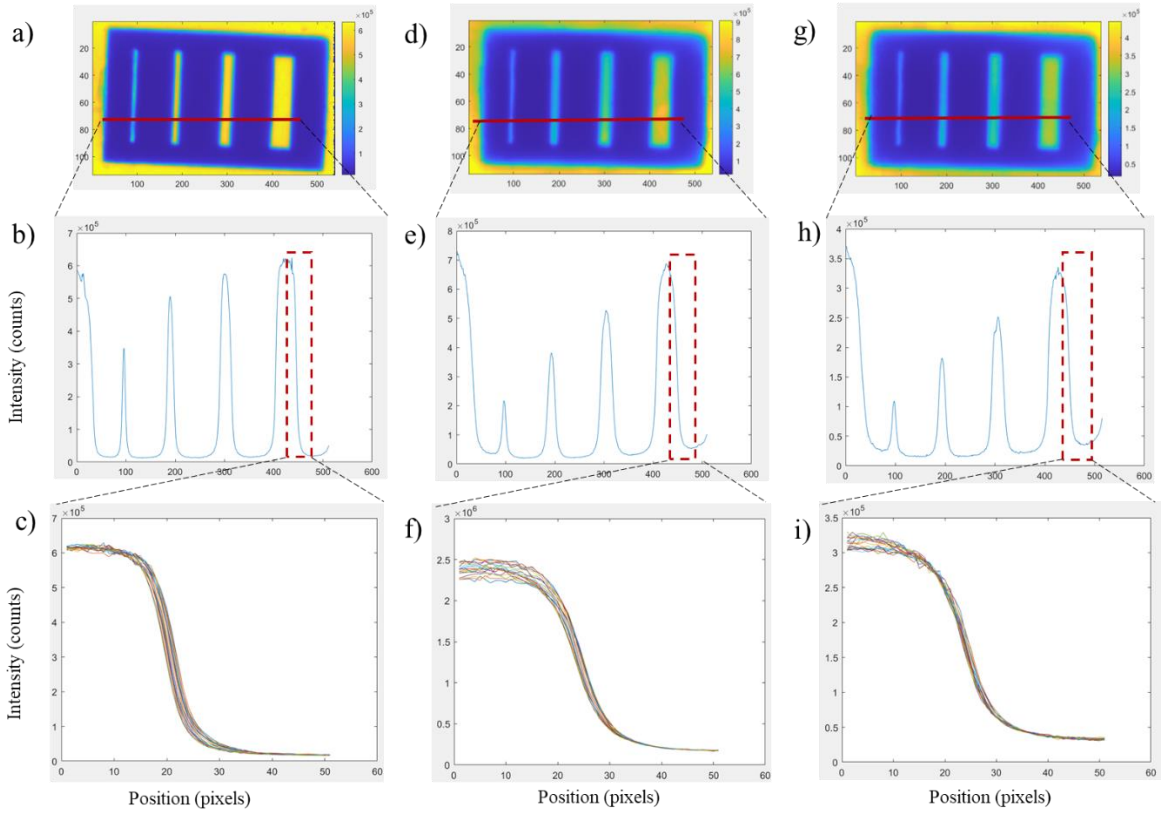

Figure 2.8: Measuring knife edge resolution with XELCI images of a line target with 700 nm light channel and light intensity profiles across the targets and zoom in profile at the edge of the 2 mm wide line. a) Image of 700 nm light through no tissue. b) Light intensity profiles across the four line widths with no tissue. c) Light intensity profiles at the edge of the 2 mm wide line with no tissue. d) Image of 700 nm light through 5 mm tissue. e) Light intensity profiles across the four line widths through 5 mm tissue. f) Line profiles at the edge of the 2 mm wide line through 5 mm tissue. g) Image of 700 nm light through 10 mm tissue. h) Light intensity profiles across the four line widths through 5 mm tissue i) Zoom in of profiles at the edge of the 2 mm wide line through 10 mm tissue.

XELCI provides high spatial resolution pH imaging/mapping through thick tissue according to the above results obtained, mainly governed by the X-ray beam width. As described in detail in the introduction, with high spatial resolution imaging in XELCI, we can image the pH heterogenic environment in biofilms. Biofilms have highly heterogeneous environments with different pH and nutrient concentrations. Also, the biofilms can be localized in one place on the implant surface; otherwise, they can be nearby along the implant surface (around 400 µm apart).[21] In both of cases, we require high-resolution imaging to identify distinct pH regions. As reported in the literature, these lower pH regions can be seen spatially in with gradients up to 2 pH units per 10 µm. [12,22] We can also image different, distinct areas in the local environment. It enables us to identify and differentiate reference and pH sensitive regions close to each other in vivo, which is impossible to obtain with techniques such as fluorescence imaging. The higher spatial resolution is achieved by scanning the sensor point-by-point. Even though, the scattering light through tissue gives rise to the diffusion of light and spread of the pointed light generated. Our group has previously studied how the pointed light diffuses through thick tissue by exciting a scintillator film with a focused X- ray source for different exposure times through different thickness of tissue. The generated pointed light in the scintillator film with full width at half maximum (FWHM) is 0.38 mm while it was 8.57 mm imaged through 10 mm tissue. This provides an idea of diffusion of pointed red light source through tissue.[22] Light will not only diffused by tissue, but scintillator film thickness and sensor thickness will also have an effect on the point spread function. By using a thinner scintillator film and an X-ray beam with a smaller diameter, we will be able to enhance the

spatial resolution more. X-rays have relatively small scattering coefficients through tissue (In the range of ~ 0.14 – 0.87 cm^{-1} depending on the energy of the X-ray, with 5 keV photons scattering more than 100 keV photons) and the absorption can slightly reduce the signal intensity but doesn't significantly affect the image resolution. Higher energy X-ray photons can absorb and scatter even less.[11] We typically run both a low-resolution scan and a high-resolution scan. The low-resolution scan is with a larger step size, and high-resolution scan is with a smaller step size. The time taken for a scan largely depends mainly on the step size, speed of the scan, and area of the scan. For example, it takes ~20 minutes to scan an area of 15 mm*15 mm for a high-resolution image at a slow scan speed of 1 mm/sec and at step size of 200 µm. Scanning the same area at lower resolution and faster scan speed reduces time (e. g. 1 mm step size and 5 mm/sec speed takes around 1 minute. Additional time is needed prior to XELCI scanning to properly set up and position the animal or specimen and understating where the implant is located. For animal experiments we monitor body temperature to make sure the temperature doesn't drop too much during anesthesia. Heating from X-ray radiation is negligible as the X-ray dose for our scan is small. Assuming a 1Gy = 1 J/kg local X-ray dose, and a heat capacity of 3.45 kJ/kg K for muscle, [23,24] the maximum temperature increase from radiation absorption would be less than a mK

$$Q = m\ c\ \Delta T \qquad \text{Equation 1}$$

Q- heat energy
m- mass
c- specific heat capacity
ΔT- change in temperature

$$\Delta T = \frac{Q}{mc}$$

$$\Delta T = \frac{1\,J/kg}{3450\,\frac{J}{kgK}}$$

$$\Delta T = 2.9 * 10^{-4}\ K$$

According to the above calculation, the increase in temperature is negligible. Additionally, even this small temperature increase would rapidly dissipate through blood circulation.

The PMTs have an active photo cathode diameter of 22 mm, this large area facilitates light capture from large diffuse area under the skin. To reduce the dark current from thermally induced electron emission, the PMTs are allowed to cool with a cooler underneath. We have a one-piece acrylic light guide which bifurcates into two streams leading to two different photo multiplier tubes (PMTs) for signal detection. This improvement for the system allowed us to enhance the light collection efficiency and thus detect signal through bone and tissue. Previously we used XELCI imaging for monitoring infections on the surface of the orthopedic implants and we could successfully image pH changes[11,25,26]. We generated high signal/noise images of a modified intramedullary rod through about 2 cm of bone and tissue in rabbit tibia. In general, light attenuation by scattering and absorption increases exponentially with tissue thickness. There is thus a tradeoff between tissue thickness imaged through, X-ray dose/scan time, and spatial resolution.

2.6 Conclusions

As shown in Figure 1, XELCI has three specific characteristics: X-ray resolution, chemical specificity, and implant surface specificity. Those characteristics are comparable

to the currently available imaging techniques such as SPECT, PET, MRI, US, etc[27–29]. Although these techniques provide high resolution structural/anatomical information in high resolution, we could not map/image chemical changes at an implant surface. XELCI combines chemical sensitivity from optical indicator dyes with implant specificity from the coating. The spatial resolution from the X-ray provides a unique, low background and higher spatial resolution detection/mapping of chemical concentrations at implant surfaces through bone and tissue.

XELCI imaging provides a unique way to study the local chemical environment at an implant surface with high spatial resolution for studying infections. In the future, the approach can be generalized to monitor other analytes by selecting different indicator dyes. It can be applied potentially for other diseases and conditions using injected or implanted medical devices coated with scintillator particles and indicator dyes.

2.7 References

(1) Röntgen, W. C. *Ueber Eine Neue Art von Strahlen*; Phys.-med. Gesellschaft, 1895.

(2) Nikl, M. Scintillation Detectors for X-Rays. *Meas. Sci. Technol.* **2006**, *17* (4), R37–R54. https://doi.org/10.1088/0957-0233/17/4/R01.

(3) Raghavendra, P.; Pullaiah, T. Biomedical Imaging Role in Cellular and Molecular Diagnostics. In *Advances in Cell and Molecular Diagnostics*; Elsevier, 2018; pp 85–111. https://doi.org/10.1016/B978-0-12-813679-9.00004-X.

(4) Weissleder, R.; Nahrendorf, M. Advancing Biomedical Imaging. *Proc. Natl. Acad. Sci.* **2015**, *112* (47), 14424–14428. https://doi.org/10.1073/pnas.1508524112.

(5) Robb, R. A. *Three-Dimensional Biomedical Imaging. Volume II Volume II*; 2018.

(6) Metsemakers, Wj.; Morgenstern, M.; McNally, M. A.; Moriarty, T. F.; McFadyen, I.; Scarborough, M.; Athanasou, N. A.; Ochsner, P. E.; Kuehl, R.; Raschke, M.; Borens, O.; Xie, Z.; Velkes, S.; Hungerer, S.; Kates, S. L.; Zalavras, C.; Giannoudis, P. V.; Richards, R. G.; Verhofstad, M. H. J. Fracture-Related Infection: A Consensus on Definition from an International Expert Group. *Injury* **2018**, *49* (3), 505–510. https://doi.org/10.1016/j.injury.2017.08.040.

(7) Trampuz, A.; Zimmerli, W. Diagnosis and Treatment of Infections Associated with Fracture-Fixation Devices. *Injury* **2006**, *37* (2), S59–S66. https://doi.org/10.1016/j.injury.2006.04.010.

(8) Renick, P.; Tang, L. Device-Related Infections. In *Racing for the Surface*; Li, B., Moriarty, T. F., Webster, T., Xing, M., Eds.; Springer International Publishing: Cham, 2020; pp 171–188. https://doi.org/10.1007/978-3-030-34475-7_7.

(9) Ady, J.; Fong, Y. Imaging for Infection: From Visualization of Inflammation to Visualization of Microbes. *Surg. Infect.* **2014**, *15* (6), 700–707. https://doi.org/10.1089/sur.2014.029.

(10) Pratx, G.; Carpenter, C. M.; Sun, C.; Xing, L. X-Ray Luminescence Computed Tomography via Selective Excitation: A Feasibility Study. *IEEE Trans. Med. Imaging* **2010**, *29* (12), 1992–1999. https://doi.org/10.1109/TMI.2010.2055883.

(11) Wang, F.; Raval, Y.; Tzeng, T. J.; Anker, J. N. X-Ray Excited Luminescence Chemical Imaging of Bacterial Growth on Surfaces Implanted in Tissue. *Adv. Healthc. Mater.* **2015**, *4* (6), 903–910.

(12) Hunter, R. C.; Beveridge, T. J. Application of a PH-Sensitive Fluoroprobe (C-SNARF-4) for PH Microenvironment Analysis in Pseudomonas Aeruginosa Biofilms. *APPL Env. MICROBIOL* **2005**, *71*, 10.

(13) Knoll, G. F. *Radiation Detection and Measurement*; John Wiley & Sons, 2010.

(14) Rodnyi, P. A. *Physical Processes in Inorganic Scintillators*; CRC press, 1997; Vol. 14.

(15) Lecoq, P. Scintillation Detectors for Charged Particles and Photons. In *Detectors for Particles and Radiation. Part 1: Principles and Methods*; Fabjan, C. W., Schopper, H., Eds.; Martienssen, W., Series Ed.; Landolt-Börnstein - Group I Elementary Particles, Nuclei and Atoms; Springer Berlin Heidelberg: Berlin, Heidelberg, 2011; Vol. 21B1, pp 45–71. https://doi.org/10.1007/978-3-642-03606-4_3.

(16) Pogue, B. W.; Leblond, F.; Krishnaswamy, V.; Paulsen, K. D. Radiologic and Near-Infrared/Optical Spectroscopic Imaging: Where Is the Synergy? *Am. J. Roentgenol.* **2010**, *195* (2), 321–332. https://doi.org/10.2214/AJR.10.5002.

(17) Ryan, S. G.; Butler, M. N.; Adeyemi, S. S.; Kalber, T.; Patrick, P. S.; Zaw Thin, M.; Harrison, I. F.; Stuckey, D. J.; Pule, M.; Lythgoe, M. F. Imaging of X-Ray-Excited Emissions from Quantum Dots and Biological Tissue in Whole Mouse. *Sci. Rep.* **2019**, *9* (1), 19223. https://doi.org/10.1038/s41598-019-55769-5.

(18) Yang, Y.; Wang, K.-Z.; Yan, D. Ultralong Persistent Room Temperature Phosphorescence of Metal Coordination Polymers Exhibiting Reversible PH-Responsive Emission. *ACS Appl. Mater. Interfaces* **2016**, *8* (24), 15489–15496. https://doi.org/10.1021/acsami.6b03956.

(19) Anderson, R. R.; Parrish, J. A. The Optics of Human Skin. *J. Invest. Dermatol.* **1981**, *77* (1), 13–19. https://doi.org/10.1111/1523-1747.ep12479191.

(20) Ash, C.; Dubec, M.; Donne, K.; Bashford, T. Effect of Wavelength and Beam Width on Penetration in Light-Tissue Interaction Using Computational Methods. *Lasers Med. Sci.* **2017**, *32* (8), 1909–1918. https://doi.org/10.1007/s10103-017-2317-4.

(21) Glaudemans, A. W. J. M.; Bosch, P.; Slart, R. H. J. A.; IJpma, F. F. A.; Govaert, G. A. M. Diagnosing Fracture-Related Infections: Can We Optimize Our Nuclear Imaging Techniques? *Eur. J. Nucl. Med. Mol. Imaging* **2019**, *46* (8), 1583–1587. https://doi.org/10.1007/s00259-019-04378-5.

(22) Fulaz, S.; Hiebner, D.; Barros, C. H. N.; Devlin, H.; Vitale, S.; Quinn, L.; Casey, E. Ratiometric Imaging of the in Situ PH Distribution of Biofilms by Use of Fluorescent Mesoporous Silica Nanosensors. *ACS Appl. Mater. Interfaces* **2019**, *11* (36), 32679–32688. https://doi.org/10.1021/acsami.9b09978.

(23) Uzair, U. A PH Sensor for Non-Invasive Detection and Monitoring of PH Changes During Implant-Associated Infection Using X-Ray Excited Luminescence Chemical Imaging. Ph.D., Clemson University, Ann Arbor, 2020.

(24) Giering, K.; Minet, O.; Lamprecht, I.; Müller, G. Review of Thermal Properties of Biological Tissues. *Laser-Induc. Interstitial Thermother.* **1995**, 45–65.

(25) Cohen, M. L. Measurement of the Thermal Properties of Human Skin. A Review. *J. Invest. Dermatol.* **1977**, *69* (3).

(26) Uzair, U.; Johnson, C.; Beladi-Behbahani, S.; Rajamanthrilage, A. C.; Raval, Y. S.; Benza, D.; Ranasinghe, M.; Schober, G.; Tzeng, T.-R. J.; Anker, J. N. Conformal Coating of Orthopedic Plates with X-Ray Scintillators and PH Indicators for X-Ray Excited Luminescence Chemical Imaging through Tissue. *ACS Appl. Mater. Interfaces* **2020**, *12* (47), 52343–52353. https://doi.org/10.1021/acsami.0c13707.

(27) Uzair, U.; Benza, D.; Behrend, C. J.; Anker, J. N. Noninvasively Imaging PH at the Surface of Implanted Orthopedic Devices with X-Ray Excited Luminescence Chemical Imaging. *ACS Sens.* **2019**, *4* (9), 2367–2374. https://doi.org/10.1021/acssensors.9b00962.

(28) Chen, H.; Rogalski, M. M.; Anker, J. N. Advances in Functional X-Ray Imaging Techniques and Contrast Agents. *Phys. Chem. Chem. Phys.* **2012**, *14* (39), 13469. https://doi.org/10.1039/c2cp41858d.

(29) Green, M. V.; Seidel, J.; Vaquero, J. J.; Jagoda, E.; Lee, I.; Eckelman, W. High Resolution PET, SPECT and Projection Imaging in Small Animals. *Comput. Med. Imaging Graph.* **2001**, *25* (2), 79–86.

(30) Garcia, E. V. Physical Attributes, Limitations, and Future Potential for PET and SPECT. *J. Nucl. Cardiol.* **2012**, *19* (S1), 19–29. https://doi.org/10.1007/s12350-011-9488-3.

CHAPTER 3

NON-INVASIVE IMAGING OF CHEMICAL CHANGES ASSOCIATED WITH INTRAMEDULLARY CANAL INFECTIONS VIA XELCI (X-RAY EXCITED LUMINESCENCE CHEMICAL IMAGING)

3.1 Abstract

Implanted medical device-associated infections are a major cause of fixation failure. Detection and treatment of these infections remain as a challenge as clinical symptoms are often delayed or completely absent till the infection reaches a later stage and harder to treat with antibiotics. Once diagnosed early, infections can be treated without removal of implants and undergoing a second surgery. Herein, we describe a X-ray Excited Luminescence Chemical Imaging (XELCI) based pH sensor for noninvasive detection and imaging of changes in local pH with high spatial and pH resolution.

The sensor is fabricated as a coating on an implant (orthopedic plates, Intramedullary nails, etc). It has two layers: a layer of Gd_2O_2S:Eu scintillators that produces 620 nm and 700 nm luminescence upon X-ray irradiation, and a pH-indicating film containing BTB (Bromothymol Blue) which covers the scintillators and alters the luminescence spectrum in a pH dependent manner. The spectrum escaping through the tissue is measured to determine the local pH as a focused X-ray beam irradiates one spot on the implant. The X-ray beam scans across the sensor surface to generate an image and measures pH point by point which enables high spatial resolution, low background measurements of local pH for studying implant associated infections. We are interested in detecting pH changes through

bone and infections associated with intramedullary nails. These are a type of orthopedic implants which are commonly implanted into the medullary cavity of the bone to fix comminuted femoral and tibial fractures. They are associated with osteomyelitis. As a preliminary study, we have imaged an epoxy-PEG coated stainless-steel rod with two distinct pH regions (pH 4 and pH 8) in a reamed rabbit cadaver tibia. We were successfully able to image the above pH changes through bone *in vitro* with XELCI imaging. With the results obtained from in vitro studies, we carried out a pre-pilot rabbit study with intramedullary rod sensor using three animal models: a control model and two infected models (one rabbit with a sensor implanted a pre-grown biofilm and other rabbit infected at the time of surgery). The study revealed that with the modified XELCI imaging system, we can detect the signal through both bone and tissue. Moreover, we observed no significant changes of the pH in the control animal compared to the infected animal models where we observed changes of pH in the intramedullary canal.

3.2 Introduction

Implantable medical devices, such as orthopedic plates, intramedullary rods, pacemakers, prosthetics, catheters, and many other biomedical devices are an extremely important component in the field of medicine, and they have significantly improved the quality of life of patients. Out of these implantable medical devices, orthopedic devices are increasingly used for fracture fixation, including intramedullary nails, external-fixation pins, plates, and screws to restore mobility. But they are linked with increased risk of

implant associated infections. For example, Magill et al report that around 50% of the nosocomial infections are biomaterial infections associated with indwelling surgical devices in the USA.[1,2] Intravascular and intraurethral infections are more common than infections related to surgical devices and *Staphylococcus aureus* was found to be the most common pathogen associated with implant infections.[3,4] But surgical biomaterial associated infections are not infrequent and should be treated with prolonged antibiotic therapy and multiple invasive procedures. In the United States, about 2 million fracture fixation devices are inserted annually and 5- 10% of them lead to implant-associated infections.[5]

Previously our group studied implanted medical device associated infections by implanting modified plate sensors on the surface of the femur of the rabbit models .[6–8] The sensors were made of layered films of scintillator particles and pH sensitive gel layers. The group studied the pH changes occur in normal healing vs an infection. As the infection starts to form with biofilm formation, we initially expected the local pH to become acidic.[9] According to the XELCI imaging (color maps of the sensors were more uniform) and pH mapping, the pH remained close to in situ pH as in no infection or normal healing. Also, the infection studies revealed that pH didn't drop significantly in the open plate infections even though there were clear signs of infection postmortem. But in one of the cavity simulation studies showed a very small drop in the pH during an infection. Our group observed a delayed restoration of the pH in one of the cavity simulation studies on the bone surface.[8] We can expect a bone cavity to be in even lower pH than the surface as we are comparing a closed system vs an open system in vivo. Slow perfusion and diffusion rates

are expected in the cavity due to slower fluid exchange. Moreover, Konttinen et al report pH measured in the femoral cavity and femoral stem of a patient with septic loosening to be 4.38 and 5.80 in a study carried out by observing both aseptic and septic patients.[10,11] As the results from infection studies on the bone surface contradict the results from clinical studies, we were curious to investigate the intramedullary canal to see whether it behaves differently in a more closed, poorly perfused environment.[9,10]

Intramedullary rods are an important category of orthopedic devices which are forced into the intramedullary canal to align the bone fragments in place for fracture healing. These devices can be associated with infections/osteomyelitis resulting in local acidosis caused by bacterial by products. Local acidosis/low extracellular pH inside the bone cavity also can influence the immune cell activity and osteoclast activity.[12–15] Moreover, in case of an implant associated infection inside bone are very complex as both local bone cells and the infecting pathogen can modify the immune response. Osteoclasts and osteoblasts are involved in constant remodeling of bone and adapting to the changes of mechanical loading. Osteoclasts degrade damaged bone by degrading mineralized bone by producing acids while osteoblasts' primary function is bone formation.[16] During bacterial bone infection, it is evident that osteolysis in osteomyelitis is majorly due to immune system because of increased osteoclast activity and decreased osteoblast activity. *Staphylococcus aureus* biofilm-conditioned media inhibited the bone formation and upregulation of RANKL (receptor activator NF kappa B ligand) caused the increased bone resorption.[17]

We describe an intramedullary rod sensor prepared by conformally coating a stainless-steel rod with scintillator layer and pH sensitive polymer hydrogel in combination with XELCI to monitor decrease in pH through both bone and tissue. pH microelectrode, fluorescent pH indicators, and MRI etc. are few other techniques that are used for monitoring pH changes at orthopedic implants, and they are summarized in the in the Chapter 1: Introduction. [18–21] XELCI will be efficient and advantageous in reporting chemical information at the infection site.[7,22] As X-ray has a low attenuation as well as the IR and near IR light generated by Gd_2O_2S:Eu particles can pass through larger distances through tissue, XELCI can provide high resolution, low background pH mapping through tissue.[23–26] By fabricating the novel sensor on the intramedullary rod, and other optimizations to the XELCI imaging system, the intramedullary cavity pH was mapped in the control rabbit as well as two infection models of the rabbits by infecting prior to the surgery and at the time of surgery.

3.3 In vitro imaging (Rabbit cadaver) of pH through tissue and bone

This experiment was designed to study whether the pH variations can be identified and mapped through both bone and tissue. As a preliminary study, an intramedullary rod sensor was prepared with two distinct pH regions and a reference region to image via XELCI.

3.3.1 Fabrication of the rod sensor

Titanium or stainless-steel rods (4 mm diameter) were purchased by McMaster Carr. They were cut into smaller pieces (20 mm) length. They were cleaned thoroughly washing with Alconox and distilled water.

The Gd_2O_2S: Eu (8 µm) luminescence particles were incorporated to two part-epoxy (Loctite) in 4:1 ratio. All the constituents were mixed thoroughly until the particles are well incorporated into epoxy. The mixture was then applied on the surface of the rods as a conformal coating where thickness of the film would be approximately 1 mm. The rods were rolled on sugar crystals to roughen the surface before curing. Then they were allowed to cure for 30 minutes to 1 hour. Later the sensor rods were put in a water bath to dissolve all the sugar crystals and leaving behind the porous scintillator layer for 15- 30 minutes. The sensors were then air dried completely. The rods were leached in ethanol 70% solution for 1 hour and allowed to air dry.

The hydrogel solution was prepared by mixing a monomer; Acrylamide (35 wt%), the cross-linker Poly(ethyleneglycol) diacrylate average Mn 700 (PEGDA 700) (35 wt%), and the UV initiator, 2,2-dimethoxy-2-phenyl acetophenone (DMPA) (1wt%), a pH indicating dye, Bromothymol Blue (BTB) (0.5 wt%) and DI water. All the chemicals are used as received and used by mass. The constituents were dissolved until clear for 30 minutes- 1 hour in a 360° rotator and with a vortex mixer. The clear solution in an open glass vial was kept in a nitrogen environment for 1-2 hours before diluting the mixture. The original polymerizable solution was diluted to make a 10% solution with DI water.

Then the rod was dip coated three times in the diluted polymer solution by leaving a reference region at the top of the rod. Then a small cut was made in middle to make two distinct pH regions on the rod. The bottom region was dipped in the pH 5 buffer and the top pH sensitive region was incubated in pH 8 region[7].

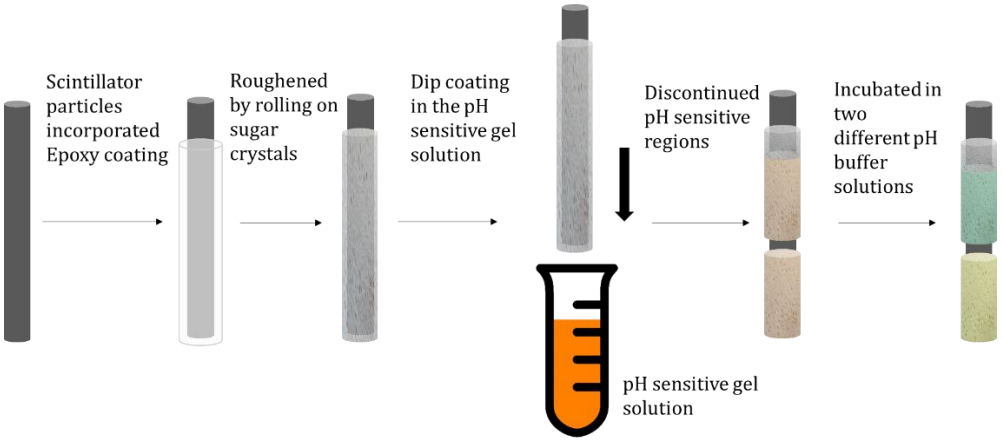

Figure 3.1: Schematic diagram showing general steps of fabricating a rod sensor.

3.3.2 Preparing the rabbit cadaver for imaging

The rabbit tibia was reamed with a 6 mm drill bit and the rod sensor was inserted into the intramedullary canal. The canal was cleaned with saline to get rid of the small bone fragments. The XELCI imaging was carried out through bone at tissue.

3.3.3 Imaging through tissue and bone

XELCI imaging was carried out through bone at tissue generally at two different step sizes. A low-resolution scan was carried out first to identify the region of interest (sensor area). After optimizing the area for the scan, a high-resolution imaging was carried

out. For a low-resolution scan a step size of 1000 µm with 5 mm/sec was used while for the high-resolution scan a step size of 250 µm with 5 mm/sec was used.

3.4 Imaging pH through tissue and bone in live Rabbit model

A rabbit study (10 or 11 days long post-surgery) was carried out to model detecting infections in the intramedullary rod. Three New Zealand White rabbits were used for this study. They were purchased from Charles River Laboratories (Wilmington, MA) and acclimated at the Godley Snell Animal Research Facility for at least 10 -14 days prior to surgery. One of the rabbits was used as a control rabbit (Rabbit 1). Two rabbits (Rabbit 2 and Rabbit 3) were used to experiment infection models. An intramedullary rod sensor with a biofilm grown before the surgery was inserted into the tibial intramedullary canal of Rabbit 2 and Rabbit 3 was infected at the time of the surgery with *Staphylococcus aureus* culture.

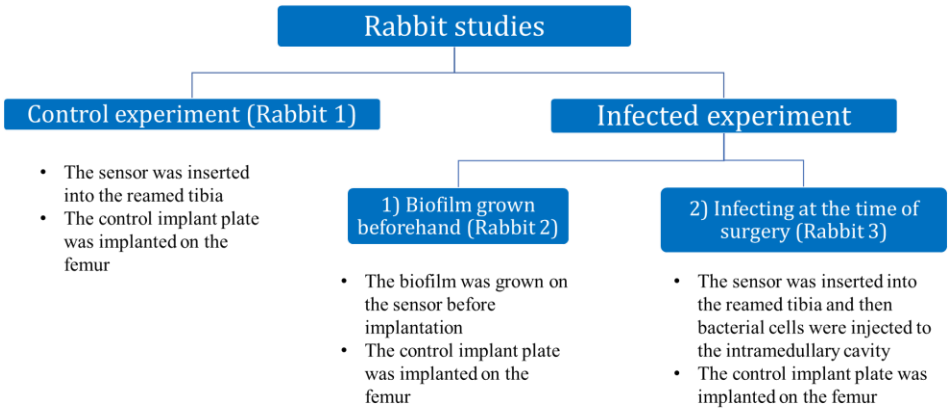

A detailed description of the experimental procedure with sensor designing surgery and imaging are presented below.

3.4.1 Fabrication of the rod sensor

Fabrication of the intramedullary rod for XELCI imaging has two basic steps: 1) Coating the stainless-steel rod with luminescent particles incorporated polymer layer and 2) Dip coating the polymer coated rod in the pH sensitive gel layer.

The luminescence particle incorporated polymer layer was prepared by mixing the Gd_2O_2S: Eu particles (8 µm) with epoxy (Loctite) in 4: 1 ratio and mixed thoroughly with until the particles are well incorporated in the polymer mixture with a wooden stick. The pre-cut stainless-steel rods (3 mm (diameter)*20 mm (length)) were coated with thin film of Gd_2O_2S: Eu incorporated epoxy. The epoxy coating was roughened with sugar crystals by pressing them on the sugar before epoxy cures. The coated rods were allowed to cure for 1hour, and sugar particles (Domino granulated sugar) were dissolved by dipping in water for 10 minutes. Once they are completely dried in the air, they were dipped in ethanol (70%) and leached for 1 hour. Again, the scintillator layer coated rods were allowed to air dry. Then, the epoxy layer was sectioned to create a reference and a sensing layer on the rod. (Shorter, top region as the reference region and longer, bottom region as the sensing/pH region). After air drying completely, the rods were dip coated (only the bottom region) in the pH sensitive Acrylamide-PEG polymeric solution in the glove box.

The hydrogel solution was prepared by mixing a monomer; Acrylamide (35 wt%), the cross-linker Poly(ethyleneglycol) diacrylate average Mn 700 (PEGDA 700) (35 wt%), and the UV initiator, 2,2-dimethoxy-2-phenyl acetophenone (DMPA) (1wt%), a pH indicating dye, Bromothymol Blue (BTB) (0.5 wt%) and DI water. All the chemicals are used as received and used by mass. The constituents were dissolved until clear for 30

minutes- 1 hour in a 360° rotator and with a vortex mixer. The clear solution in an open glass vial was kept in a nitrogen environment for 1-2 hours before diluting the mixture. The original polymerizable solution was diluted to make a 10% solution with DI water.

The rods were coated with polymeric solution by dip coating 3 times and curing under UV for 1 minute in between each dip coating and after dip coating the last layer, it was cured for 3 minutes.

3.4.2 Fabrication of the plate sensor

Plate sensors were used as a control on the rabbit femur to detect any pH changes occurring. These implant plates are used in previous rabbit experiments to monitor implant associated infections on the surface of the bone. The implant plate is machined of acrylic and has 4 chambers. Two of the small chambers are for reference and two larger chambers will be incorporated with pH sensing sensors. The bottom most layer is a thin film made of luminescence particle incorporated polymeric material.

Polydimethylsiloxane mixture was made by mixing the SYLGARD 184 Silicone Elastomer Base and SYLGARD 184 Silicone Elastomer in 10:1 ratio. Gadolinium Oxysulfide (Gd_2O_2S: Eu) luminescence particles (8 µm) particles were encapsulated in PDMS (Polydimethylsiloxane) in 4:1 ratio and mixed well to incorporate microparticles fully in the polymer material. Then the thin film was made using a spacer made from transparency film. A transparency film with a rectangular hole in middle was cut and glued on to a microscope slide. The scintillator particle film was spread evenly with a spatula to

obtain the thin film. These films were cured in the oven at 100 ℃ for 10-15 minutes and they were cut into required shape for the experiment.

Polyacrylamide-polyethylene glycol hydrogel pH sensing film was made by mixing a monomer; Acrylamide (35 wt%), the cross-linker Poly(ethyleneglycol) diacrylate average Mn 700 (PEGDA 700) (35 wt%), and the UV initiator, 2,2-dimethoxy-2-phenyl acetophenone (DMPA) (1wt%), a pH indicating dye, Bromothymol Blue (BTB) (0.5 wt%) and DI water. All the chemicals are used as received and used by mass. The constituents were dissolved until clear for 30 minutes- 1hour in a 360° rotator and with a vortex mixer. The clear solution in an open glass vial was kept in a nitrogen environment for 1-2 hours before polymerizing in the reaction cell where a silicone spacer sandwiched between two glass slides. The gels were polymerized entirely inside a glove box for 10-12 minutes under a nitrogen environment. After polymerization the hydrogels were cut as required to use in the experiment.

Once all the necessary layers are ready and synthesized, they were assembled in the acrylic implant plate sensor. Two small chambers were layered only with scintillator films and the big chambers were assembled with both layers; the pH sensing hydrogel layer was equilibrated in PBS pH 7.4 buffer solution over the scintillator film (see Figure 3.2).

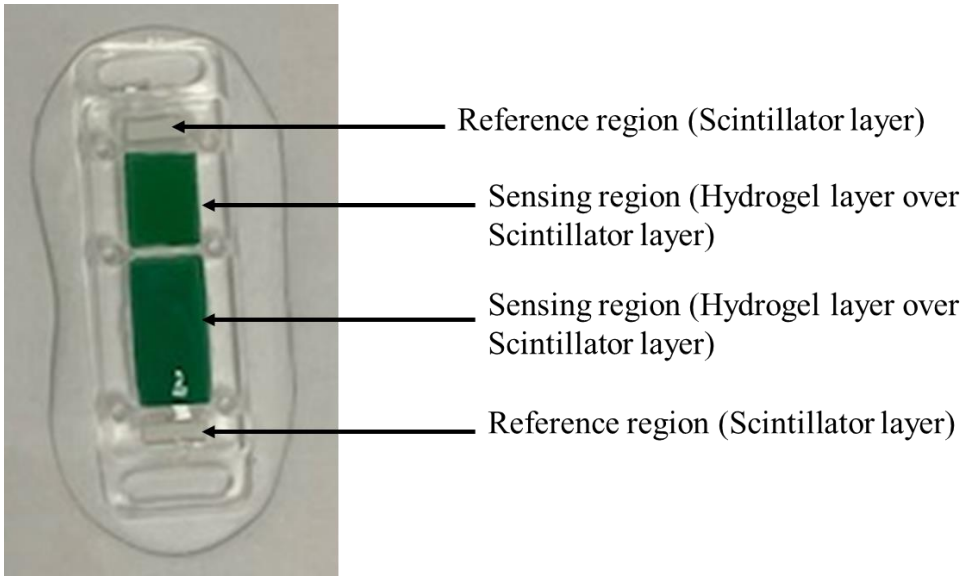

Figure 3.2: A photo of the plate sensor to implant on the surface of the femur.

3.4.3 Growing bacteria on the rod sensor

A fresh culture of Staphylococcus aureus 1945 (ATCC 25923) was prepared by taking one colony from a TSA plate streaked within one week to inoculate 5 ml of sterile Tryptic Soy Broth (TSB). The bacterial culture was shaken at 37 ℃ for 16-18 hrs, until stationary phase. The culture was pelleted from the TSB via centrifugation and washed twice with Phosphate Buffer Solution (PBS) and the pellet was resuspended in 5 ml of sterile PBS. Bacterial concentration was quantify using optical density at 600 nm using the linear range. Then the sample was diluted to 10^5 cells/mL using sterile PBS. The Tryptic Soy Agar (TSA) was sterilized by autoclaving and then cooled by mixing until the temperature reached 45 ℃. The TSA was inoculated by bacteria. The diluted bacterial culture (100 µL) was pipetted onto the surface of the implantable sensor. The implants were first sterilized by immersing in 70% etanol solution for 5 minutes and stored in the

sterile PBS. Another 100 µL of uninoculated TSA was pipetted over another implant as a control. An additional 100 µL of uninoculated TSA over the implantable sensor before it was inoculated at 37 ℃ for 48 hours prior to implantation.

3.4.4 Sensor insertion and rabbit surgery

Dr. John Parrish performed this rabbit surgery in the Godley Snell Research Center.

The control experiment was conducted in Rabbit 1. After induction of anesthesia, Rabbit 1 was placed in a right lateral position and final aseptic preparation was accomplished. A lateral approach was performed to the mid shaft of left femur and the implant plate was applied. Sterile glue was applied to anterior surface and incision was closed with 4-0 Vicryl. The rabbit position was changed to dorsal recumbent with the knee bent. A second surgery was then performed approach to the anterior tibia by incised skin. A 1.8 mm pilot was drilled into the tibial plateau. An X-ray was taken to confirm the location. The drilled hole was widened in the cortical by a 4.5 mm then a 6.0 mm bit to allow for implant passage. Intramedullary rod sensor was inserted into the reamed tibial canal and sterile PBS 7.4 (100 µL) was introduced, (the sensor was gently tapped into the place with ortho hammer and elevator). Then the wound was closed by sterile bone wax. The tissue wound was closed with 4-0 Vicryl. Both wounds on the femur and tibia were sealed with skin glue. A plain radiograph was obtained after the surgery and rabbit was allowed to recover.

Figure 3.3: Photos and plain radiographs acquired during the surgery of Rabbit 1 A) The femur exposed and ready for the implant plate to be placed. B) Preparing the tibia for placing the intramedullary rod sensor. C) The plain radiograph obtained after the two surgeries showing the rod sensor placed in the tibial intramedullary canal (the plate and sensor was further up on the femur, not in view here, but evident in Figs. 3.4 and 3.5 for Rabbits 2 and 3).

One of the infected model experiments was conducted in Rabbit 2. After induction of anesthesia, Rabbit 2 was placed in a right lateral position and final aseptic preparation was accomplished. A lateral approach was performed to the mid shaft of left femur and the implant plate was applied. Sterile glue was applied to anterior surface and incision was closed with 4-0 Vicryl. The rabbit position was changed to dorsal recumbent with the knee bent. A second surgery was then performed approach to the anterior tibia by incised skin. A 1.8 mm pilot is drilled into the tibial plateau. An X-ray was taken to confirm the location. The drilled hole was widened in the cortical by a 4.5 mm then a 6.0 mm bit to allow for implant passage. Intramedullary rod sensor with a biofilm of *Staphylococcus aureus* grown beforehand the surgery was inserted into the reamed tibial canal. (The sensor was gently tapped into the place with ortho hammer and elevator) During insertion of the intramedullary rod, the reference region was displaced from the original position, and it is

visible on the plain radiograph shown on the figure below. Then the wound was closed by sterile bone wax. The tissue wound was closed with 4-0 Vicryl. Both wounds on the femur and tibia were sealed with skin glue. After that the rabbit was allowed to recover.

Figure 3.4: Photos and plain radiographs acquired during the surgery of Rabbit 2 A) The femur exposed and implant plate glued to the femur. B) Localization of the intramedullary rod sensor with a biofilm grown in the proximal tibia. C) The plain radiograph obtained after implant implantation.

The second infected model experiments were conducted in Rabbit 3. After induction of anesthesia, Rabbit 3 was placed in a right lateral position and final aseptic preparation was accomplished. A lateral approach was performed to the mid shaft of left femur and the implant plate was applied. Sterile glue was applied to anterior surface and incision was closed with 4-0 Vicryl. The rabbit position was changed to dorsal recumbent with the knee bent. A second surgery was then performed approach to the anterior tibia by incised skin. A 1.8 mm pilot is drilled into the tibial plateau. An X-ray was taken to confirm the location. The drilled hole was widened in the cortical by a 4.5 mm then a 6.0 mm bit to allow for implant passage. Intramedullary rod sensor was inserted into the reamed tibial canal. (The sensor was gently tapped into the place with ortho hammer and elevator) An

inoculation of *Staphylococcus aureus* (100 µL) was introduced into the intramedullary canal. Then the wound was closed by sterile bone wax. The tissue wound was closed with 4-0 Vicryl. Both wounds on the femur and tibia were sealed with skin glue. Then the rabbit was allowed to recover, and imaging was performed periodically.

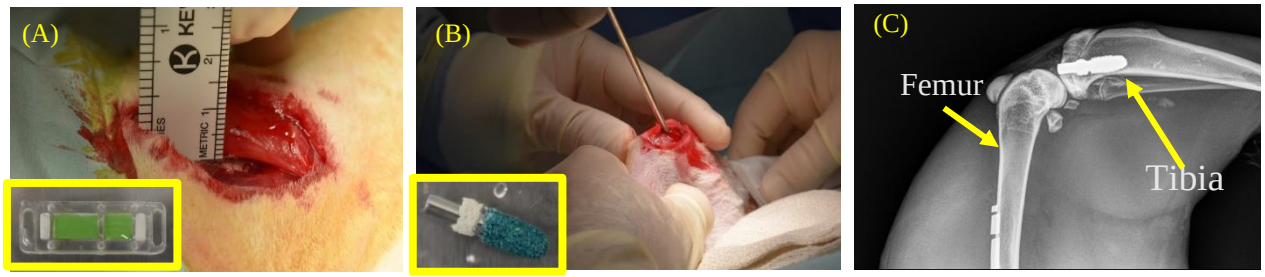

Figure 3.5: Photos and plain radiographs acquired during the surgery of Rabbit 3. A) The femur exposed for the implant plate to glue and showing the tissue thickness of the flap of tissue over the femur. B) Drilling the tibia for inserting the intramedullary rod sensor. C) The plain radiograph obtained after the two surgeries

3.4.5 Imaging through bone and tissue

Rabbits were imaged via XELCI at two step sizes (1000 µm and 250 µm) to obtain rapid low-resolution and high-resolution but slower scans of the sensor, respectively. The X-ray source voltage was set to 50 kV and current to 600 µA. Speed for y-axis travel is 5 mm/sec and return velocity was at 12 mm/sec. The scan area depends on the positioning of the rabbit on the stage.

3.4.6 Postmortem studies and pH reversibility studies

After euthanasia of the animal, the pH of the surrounding environment of the sensors were checked with pH papers. Moreover, the pH chambers, surface of the sensors were also checked. After explaining the sensors, the hydrogel pieces were put in higher and lower pH buffers to monitor the reversibility of the sensors. Photos were taken at each buffer solution after equilibration.

3.4.7 Calibration curve for the rod sensor through tissue

The rod sensors were prepared as described previously and they were incubated at different pHs ranging from 4-8 for 2 hours. Then the rods were imaged with tissue and no tissue to obtain the calibration curve for both high- and low-resolution scans.

3.4.8 Calibration curve for the plate sensor through tissue

The gel sensors used for animal studies were utilized to develop a calibration curve. Similar size (5 mm) gel discs were cut using a hole punch, placed in the wells over the scintillator particle layer, and incubated in the specific buffer (4-8). The well plate was first imaged with no tissue and then imaged through 10 mm porcine tissue for both high- and low-resolution scans.

3.5 Results and Discussion

3.5.1 In vitro imaging (Rabbit cadaver) of pH through tissue and bone

As intramedullary rods are used to treat long bone fractures, a coated stainless-steel rod is used to investigate pH changes during osteomyelitis/bone infection.[27,28] To study the pH changes occurring due to osteomyelitis inside the intramedullary canal of a tibia, we imaged a rod sensor with two distinct pHs. The stainless-steel rod sensor was coated with epoxy-PEG pH film and created two pH regions by incubating in two different pHs. It was then inserted in the reamed tibia of a rabbit cadaver as a method similar to Odekerken et al.[29] Figure 3.6 (A) shows the epoxy-PEG pH sensor coated stainless-steel rod and Figure 5 (B) shows the inserted rod sensor in the reamed rabbit tibia. Once the XELCI imaging was carried out on the sensor and analysis of the data we could clearly differentiate the two distinct pHs through bone and tissue. Figure 3.7 shows the images of 620 nm, 700 nm, and ratio (620 nm/700 nm).

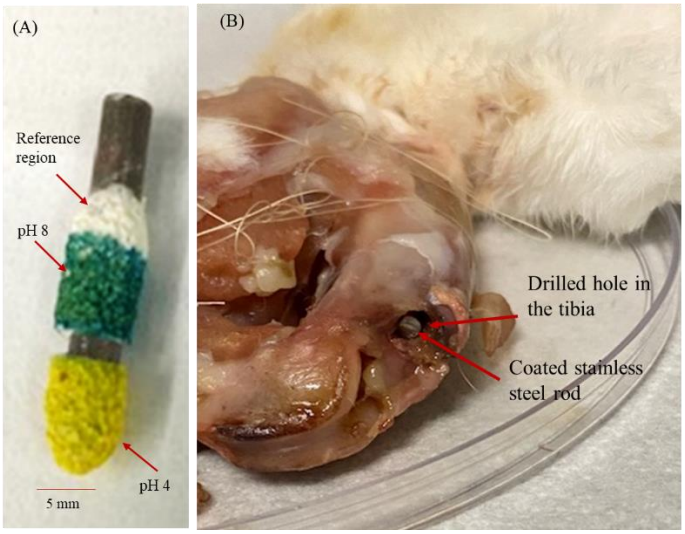

Figure 3.6: (A) Stainless steel rod coated with Gd_2O_2S:Eu incorporated epoxy and pH sensitive Acrylamide-PEG gel (B) The coated stainless - steel rod inserted to the drilled hole in the rabbit tibia.[7] (Reproduced with the permission from Reference 7).

The acidic pH region (pH 4) is indicated as a bright signal than the basic pH region (pH 8) in the 620 nm image. It can be described due to the stronger absorption of the scintillator emission by the pH dye at basic pH. Therefore, the two distinct pH regions and the reference region can be clearly imaged through the bone and tissue as shown in the Figure 3.7 (A), (B) and (C) with the XELCI imaging.

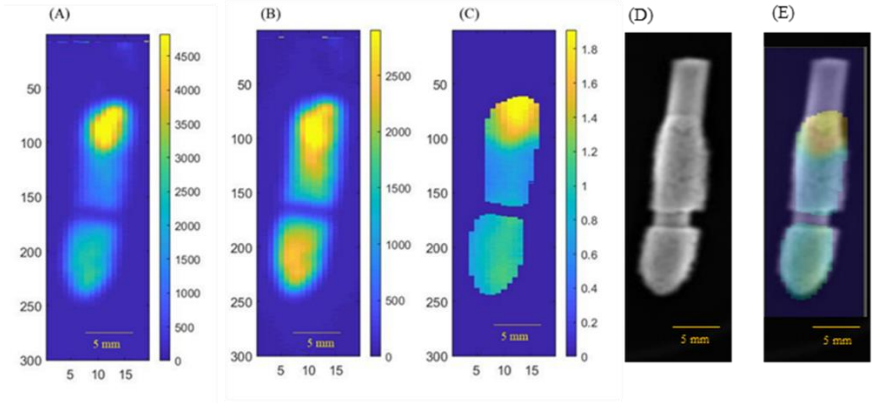

Figure 3.7: XELCI images of the rod sensor in the intramedullary canal. (A) Analyzed image for 620 nm wavelength. (B) Analyzed image for 620 nm wavelength. (C) Analyzed Ratio image (I_{620}/I_{700}). (D) Plain radiograph of the sensor. (E) Superimposed radiograph and XELCI ratio image.[7] (Reproduced with the permission from Reference 7).

3.5.2 In vivo imaging (Rabbit studies) of pH through tissue and bone

Rabbit 1 was chosen as the control model of the experiment without inoculating the tibial intramedullary canal. The rod sensor was implanted in the intramedullary canal and imaging was carried out for Day 0 through Day 11 until postmortem. Figure 3.8 below shows the images of the sensors generated in MATLAB throughout the days. The sensor was equilibrated in PBS 7.4 buffer before implantation and the Day 0 before implantation image demonstrate that the sensor is in basic pH. The bright yellow area indicates the reference region, and the darker blue area indicates the sensing area with a basic pH. The signal ratio of the sensing to the reference area remains the same throughout the days. Also, the postmortem imaging suggests that the pH of sensing area of rod sensor remains same. Also, the plate sensor pH didn't change significantly throughout the days as expected which was implanted on the femur surface of the same leg.

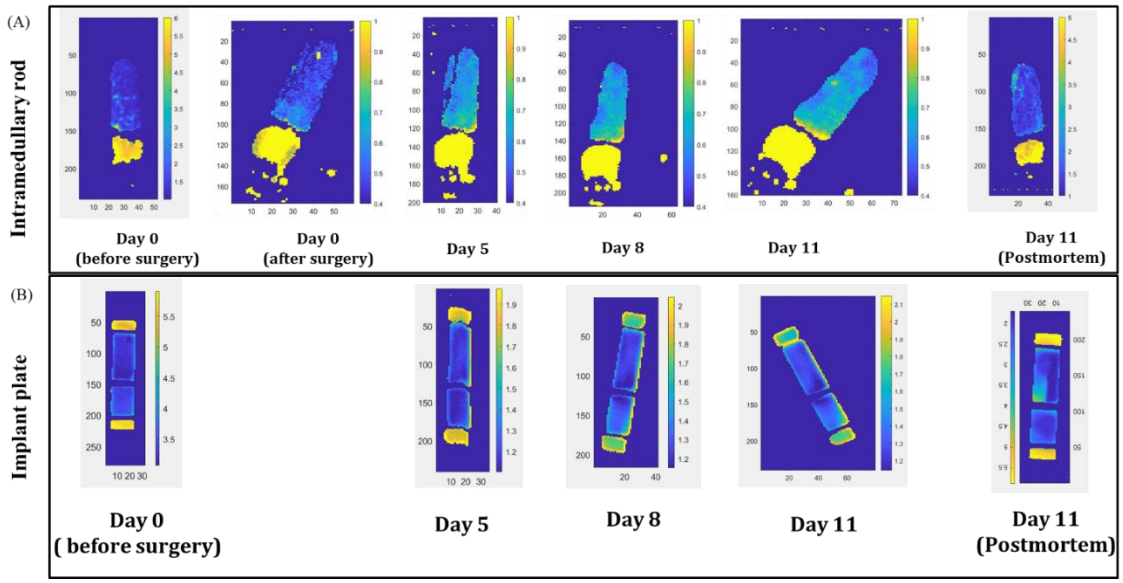

Figure 3.8: Ratio images I_{620}/ I_{700} for Control rabbit (Rabbit 1). A) The XELCI ratio images of the rod sensor showing the pH variations throughout the days Day 0 through Day 11. B) The XELCI ratio images of the plate sensor showing the pH variations throughout the days Day 0 through Day 11.

The first infected model was implanted with a pre-biofilm grown (for 48 hours) rod sensor. The Figure 3.9 below shows the ratio (I_{620}/I_{700}) images of the rod sensor and plate sensors from Day 0 through Day 11 before implantation and after implantation. After analyzing the data and calculating the signal/reference counts ratio indicates that the pH of the intramedullary canal drops and reach to a acidic pH and later the acidity reduces gradually until Day 11. Figure 3.11 C demonstrates this variation in the pH throughout the days.

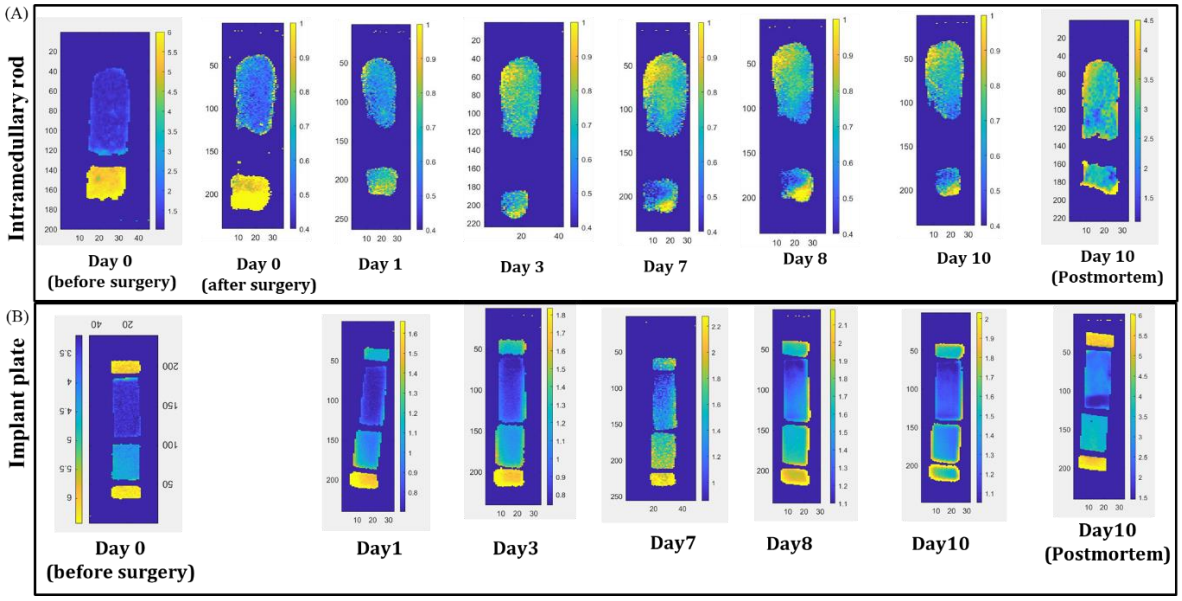

Figure 3.9: Ratio images I_{620}/ I_{700} for infected-inoculated rabbit (Rabbit 2). A) The XELCI ratio images of the rod sensor showing the pH variations throughout the days Day 0 through Day 10. B) The XELCI ratio images of the plate sensor showing the pH variations throughout the days Day 0 through Day 10.

The second infection study was carried out by inoculating the tibial intramedullary canal at the time of the surgery. Once the sensor is implanted and infected with Staphylococcus aureus inoculum, the imaging was carried out for 10 days until euthanasia. Figure 3.10 below shows the ratio images of the rod sensor and plate sensor for each day of the imaging was carried out. According to the calculations done for the Rabbit 3 ratio images, it shows the pH of the intramedullary canal reached a basic pH after a day of implantation and later the pH became acidic. Also, this variation of the pH changes is shown on a graph the pH change (Signal/reference) vs postoperative days in Figure 3.11C.

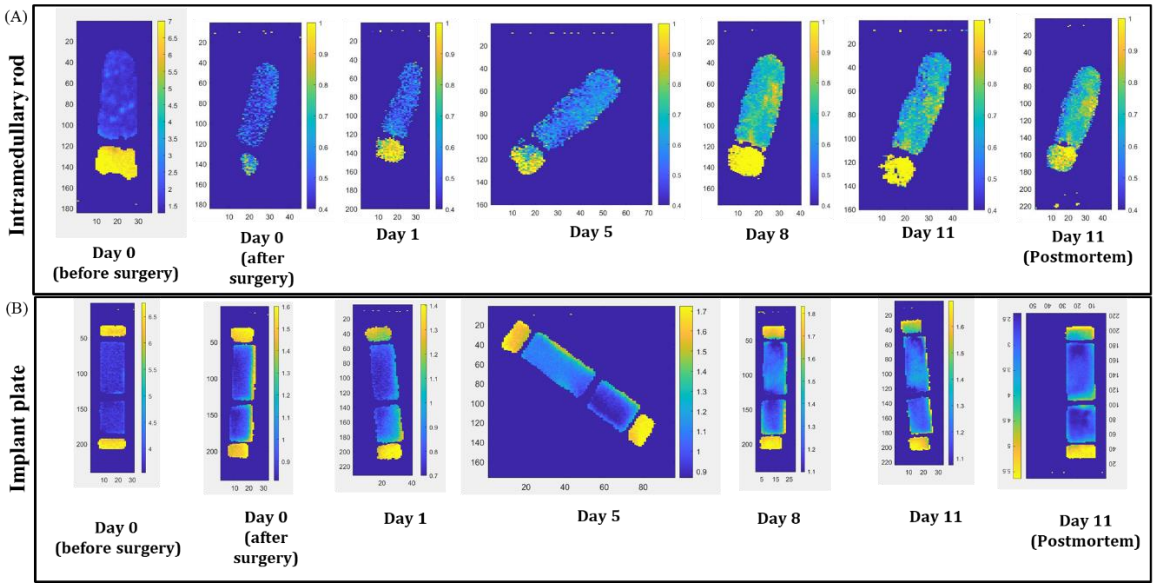

Figure 3.10: Ratio images I_{620}/I_{700} for rabbit with rod cultured with bacterial prior to implantation (Rabbit 3). A) The XELCI ratio images of the rod sensor showing the pH variations throughout the days Day 0 through Day 11. B) The XELCI ratio images of the plate sensor showing the pH variations throughout the days Day 0 through Day 11.

According to the XELCI images of the implants obtained, we can clearly see a uniform color of the pH sensors which indicates a constant pHs in the surrounding pH regions for all the plate sensors implanted on the bone surface of the femur. Moreover, a similar case was observed for the control rabbit intramedullary rod sensor. We can determine that throughout a normal healing cycle, the pH changes at the implants behave the same and uniform with no significant difference in pH. Compared to infection studies on Rabbits 2 and 3, the pH changes are clearly visible in the intramedullary canal. According to the acquired images of the rod sensor (Rabbit 2 & 3), the pH variations seem to be evenly

distributed throughout the implant surface. We can observe some fine features with different color scales; however, the shape of these features appears to be from unevenness of the sensor as we make the particle layer porous as is evident in photos of the sensor in buffer (Fig 3.11A).

A calibration curve was developed for the intramedullary rod sensor by imaging the rod sensor incubated in different pHs ranging from pH 4 to pH 8. The rods were incubated in the buffer solution for an hour and imaging was carried out. XELCI imaging was performed on the rods with 10 mm porcine tissue and without tissue. Calibration curves are plotted by calculating the signal/reference for the rods at different pHs. Figure 3.11B shows the graphs of ratio vs pH for the rods with and without tissue. After analysis of the images throughout the imaging days, the pH variations were graphed with respect to the days. The pH of the sensor was achieved by comparing the values to the calibration curve. As shown in the figure below, the control rabbit exhibits no significant changes in the pH during the healing process (~ 7.8). For both the infected models, we observed the reduction in the pH throughout the imaging days. Rabbit 2 showed pH variations in (~7.4 to 5.6) range while Rabbit 3 showed pH variations in (~6.9- 5.8) range.

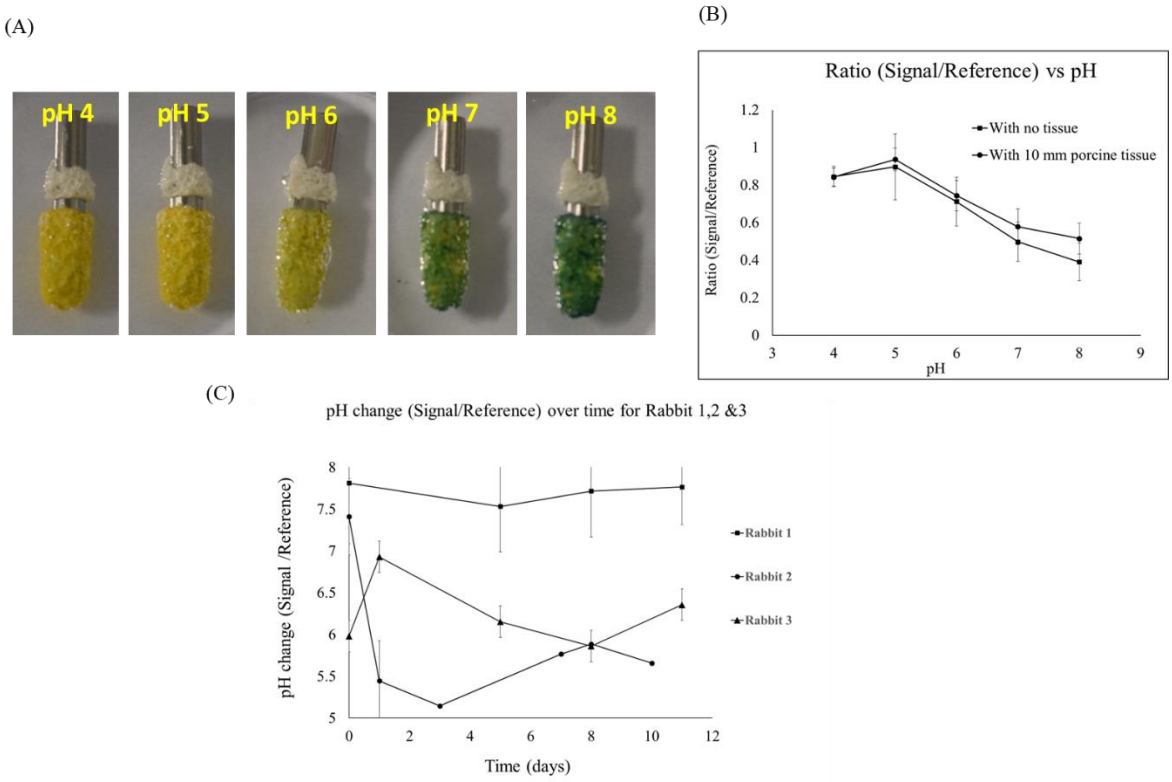

Figure 3.11: Calibration studies for rod sensors A) The rod sensors incubated in different pH solutions. B) The graph of ratio (Signal/Reference) vs pH curve for with no tissue and with porcine tissue. C) pH change over time for Rabbit 1,2 & 3 (Average ratio normalized to sensor region over time for Rabbit 1,2 & 3, and associated pH calculated from calibration curve B with no tissue). Error bars calculated from standard deviation of pixels in sensor region.

As suggested by the data analysis for implant plates during the imaging days, they exhibited no significant change in the pH values during healing as expected. The figure below (Figure 3.12) shows the calibration curve developed for the gel sensors and it indicates the pH of the implant plate varied in the range of ~ 7.4- 6.8. The pH changes for all three rabbits are shown in the graph (Figure 3,12 C). These pH values were calculated using the with tissue calibration curve presented in the Figure 3.12 B. As illustrated in the MATLAB ratio images, the color maps show a difference in the two chambers of the implant plate specially for Rabbit 2 indicating a lower pH in the smaller chamber. Postmortem, we did observe that the color in the small chamber appeared greener (more acidic), which may be due to the agarose layer we put on top of the sensor layer. After the euthanasia, the sensors were explanted from the rabbit and pH of the surrounding tissue, pH of the recovered gel sensors were checked. The tests suggested the surrounding tissue and the gels of Rabbit 1 (control) were remained in basic pH (pH 7.5-7.8) postmortem. Figure 3.12 A and B shows the photos of pH observations with the pH strips. The difference between the observed color of the indicator film and the pH paper measurement suggests that the pH film was measuring a slightly different region (e.g., below the agarose layer).

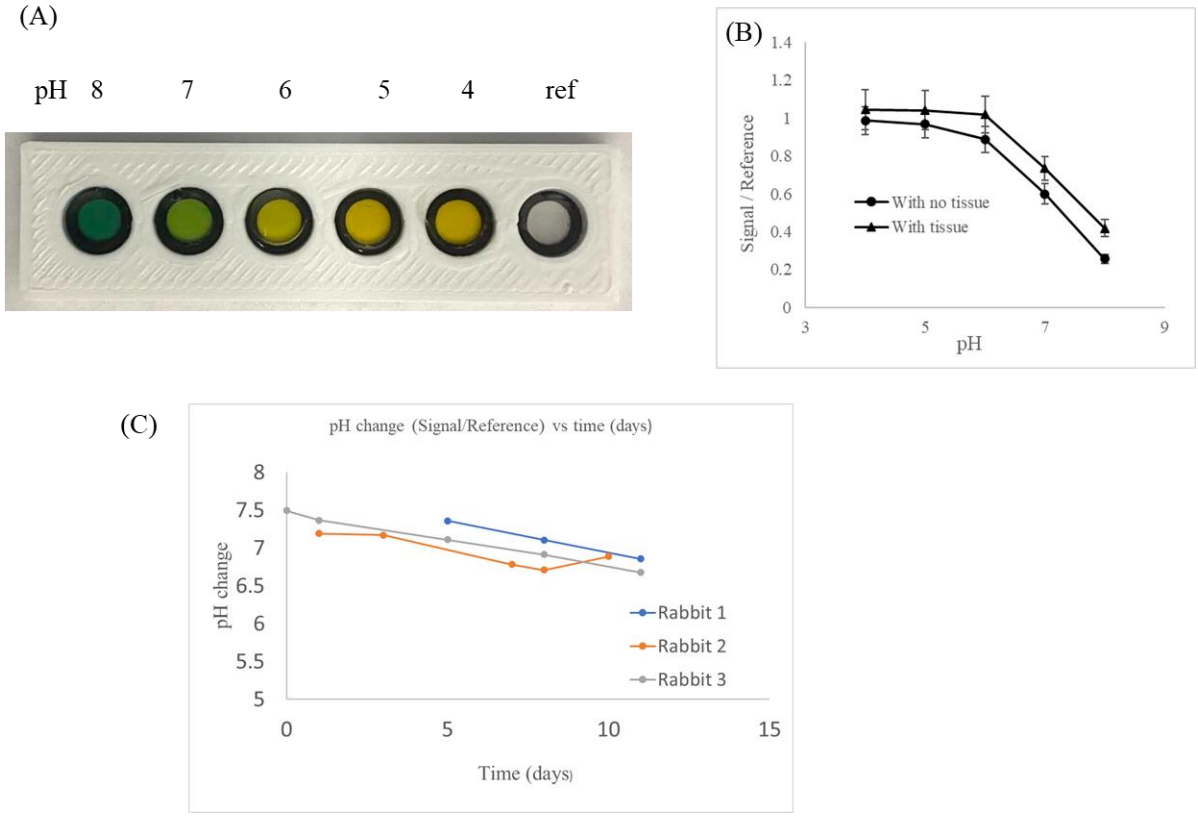

Figure 3.12: Calibration studies for hydrogel sensors on plates and data for plates in Rabbit prepilot studies. A) Photo of the gel sensors incubated in different pH solutions. B) The XELCI Ratio (Signal/Reference) vs pH with no tissue and with porcine tissue. C) pH change over time for Rabbit 1,2 and 3 (Average ratio normalized to sensor region vs time for Rabbit 1,2 and 3).

It is unclear if the XELCI image was able to observe the change in color from the pH indicator. On the one hand, the ratio did look different in Figure 3.9, but on the other hand, there is some ambiguity in which reference region to use, and we observe differences between the reference for each chamber. Postmortem, we observe more blood over one of the reference regions (Figure 3.13) which could account for the differences. If we use the closest chamber reference for each camber, to determine the corresponding pH (which would be the logical way to avoid tissue dependent spectral distortion), we didn't see a significant variation between chamber pHs. This highlights the need for more reference regions in proximity to sample, and controlling the design to make pooling of blood over the reference regions less likely.

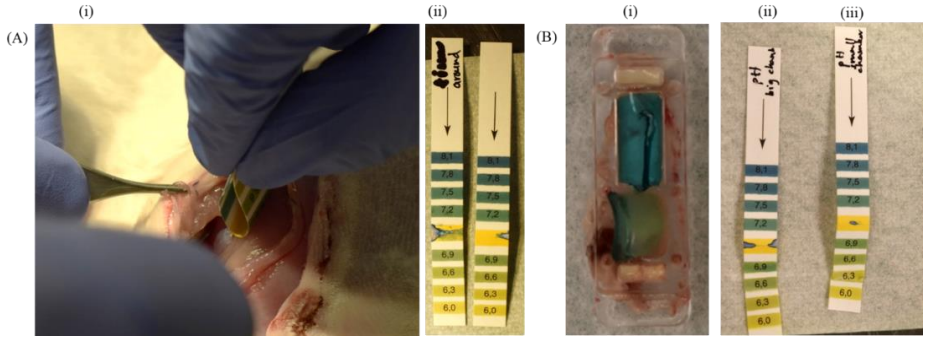

Figure 3.13: Postmortem images of Rabbit 1 after extraction of implant plate. a) Testing the pH of the surrounding tissue of the implant plate (i) rubbing the pH test strip on the tissue (ii) photo showing the color change of the pH strip. b) Testing the pH of the gels embedded in the implant plate (i) implant plate extracted after postmortem (ii) photo

showing the color change of the pH strip for big chamber (iii) photo showing the color change of the pH strip for small chamber.

The pH of the top of the tibia and the surface of the rod sensor were tested postmortem with the pH strips and they were also exhibiting basic pHs around pH 7.5-7.8. The photos of these observations are shown in the Figure 3.14 below.

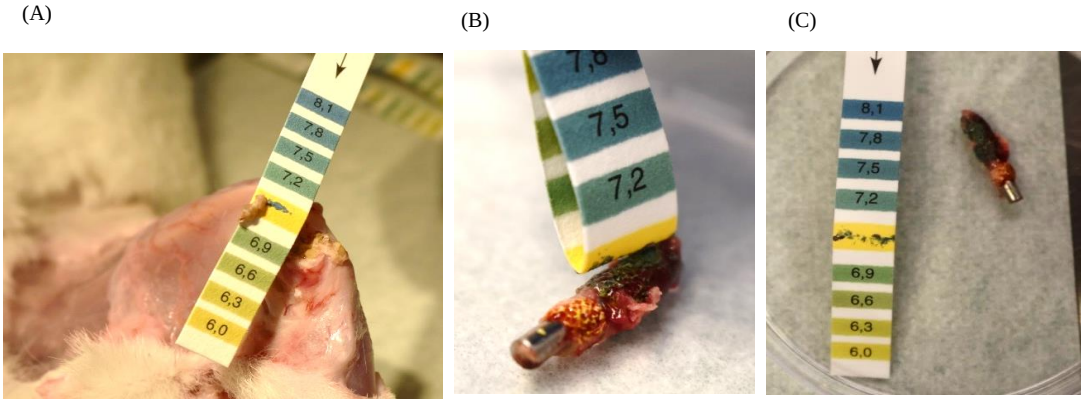

Figure 3.14: Testing pH of the fluids of tibial opening and extracted rod sensor from Rabbit 1 A) Testing pH of the top of the tibia. B) Testing pH of the surface of the rod sensor. C) The pH strip indicating the pH.

The plate sensors and rod sensors implanted on the Rabbit 2 were also tested for pH postmortem. The surrounding tissue of the plate sensor and gel sensors showed basic pH varying from pH 7.8 to 8.1 (Figure 3.15 A and B).

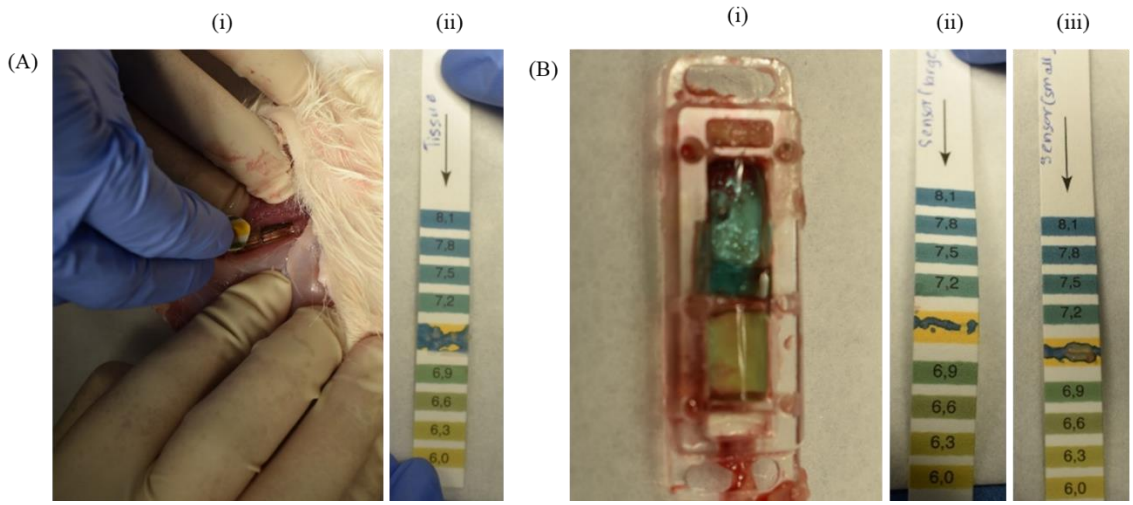

Figure 3.15: Postmortem images of Rabbit 2 after extraction of implant plate: a) Testing the pH of the surrounding tissue of the implant plate (i) rubbing the pH test strip on the tissue (ii) photo showing the color change of the pH strip. b) Testing the surface pH of the two chambers (i) explanted implant plate (ii) pH of the big chamber (iii) pH of the small chamber.

In the postmortem studies, the signs of infection around tibia such as white color pus were observed. The pH of the top of the Rabbit 2 infected tibia and the rod sensor pH were slightly acidic than the pH of the plate sensor. As shown in the Figure 3.16 A and B the pH of the top of the tibia was around 7.2 while the rod sensor was around 6.9 according to the pH strips.

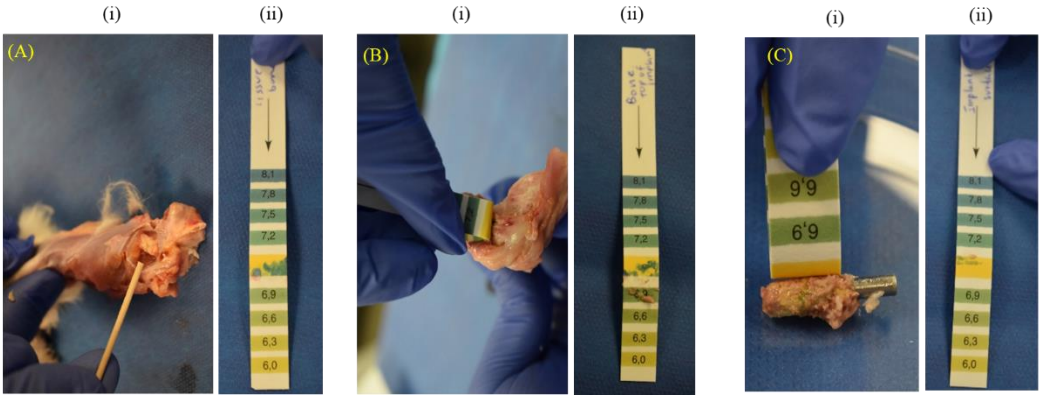

Figure 3.16 Testing pH of the fluids of tibial opening and extracted rod sensor from Rabbit 2 A) (i) Testing the pH of the tissue on top of tibia (ii) The pH strip showing the pH B) (i) Testing the pH of the top of the implant (ii) The pH strip showing the pH C) (i) Testing the pH of the implant surface (ii) The pH strip showing the pH

The pH was tested of the sensors removed postmortem with pH strips for Rabbit 3 infected model. The non-infected plate sensors were showing basic pHs in around 7.8- 8.1 (Figure 3.17).

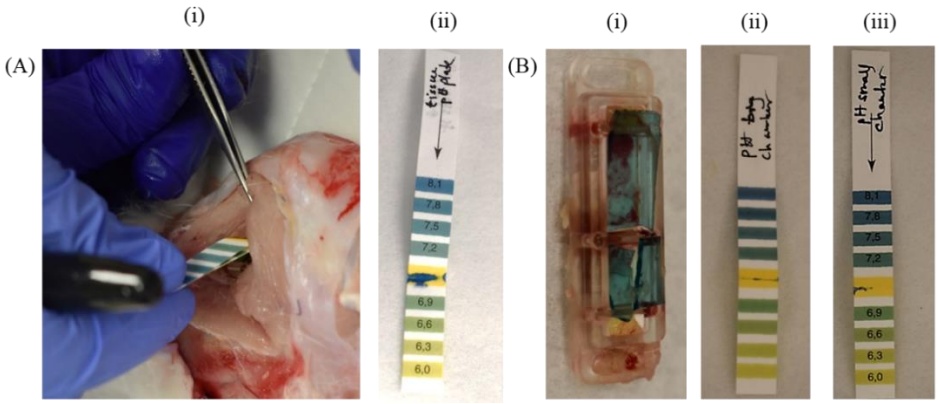

Figure 3.17: Postmortem images of Rabbit 3 after extraction of implant plate. A) Testing the pH of the surrounding tissue of the implant plate (i) rubbing the pH test strip on the tissue (ii) photo showing the color change of the pH strip. A) Photos of testing the pH of adjacent fluid using pH indicator paper.

Clear signs of infections were observed postmortem. As shown in the Figure 3.18 A), the top of the tibia had a pocket of abscess. The pH of the top of the tibia was showing pH 6.9-7.2. Also, the rod surface was showing somewhat increase in pH on the pH strip.

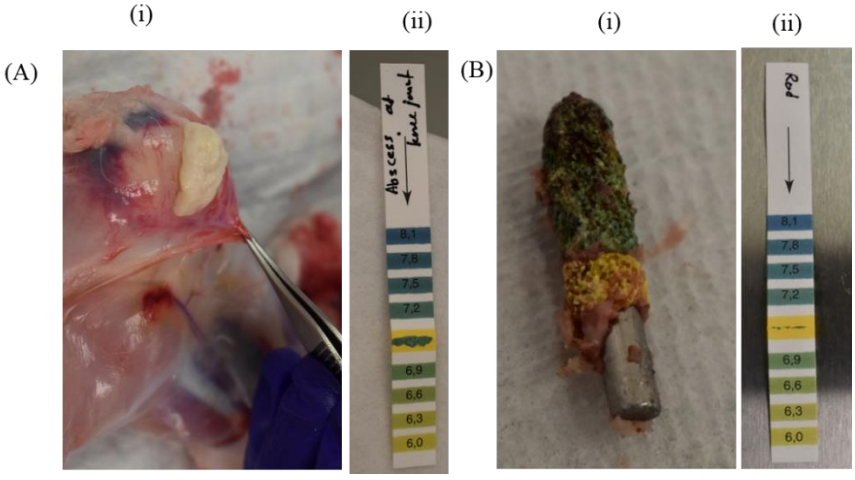

Figure 3.18 Testing pH of the fluids of tibial opening and extracted rod sensor from Rabbit 3. A) (i) Testing the signs of infection/Abscesses (ii) The pH strip showing the pH. B) (i)Explanted rod sensor (ii) pH strip showing rod surface pH.

Moreover, the gels sensors recovered from the implant plates on bone surface of the rabbits were exhibiting more basic pH postmortem and slightly intense green color as the body homeostasis is disturbed. Although the gel sensors were similar in color before implantation, the some of the pieces were exhibiting a slightly basic color. That can be due to exposure to the higher carbon dioxide concentrations in the air compared to inside the body. Those sensors were also exposed to the air as the top agarose layer on the plate sensors were damaged or broken while retrieving the sensors cut opening the tissue.

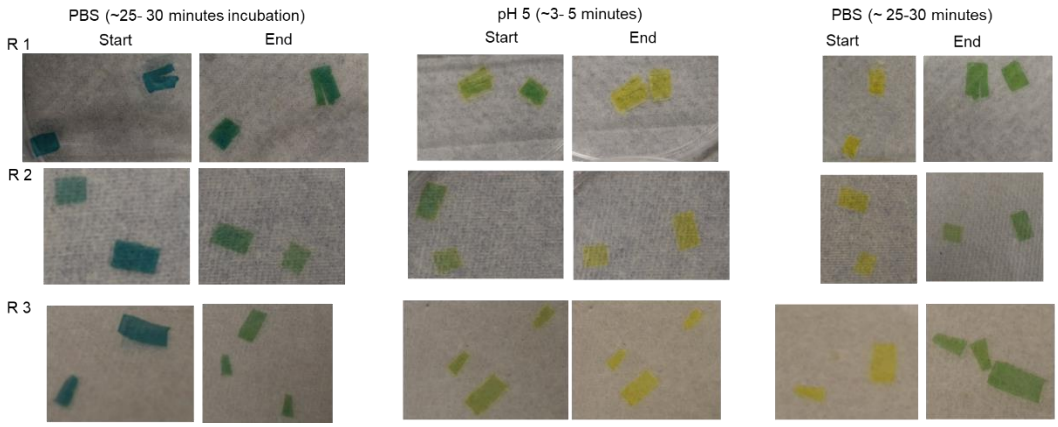

Figure 3.19: Reversibility studies for hydrogel pieces from implant plates. (i) The sensor incubation in the pH 7.4 buffer for Rabbits 1, 2 and 3. (ii) The sensor incubation in the pH 5 buffer for Rabbits 1, 2 and 3. (iii) The sensor incubation again in the pH 7.4 buffer for Rabbits 1, 2 and 3 (for each buffer a start and end of the sensors are shown).

As a part of postmortem studies, we have studied the reversibility of the hydrogel sensors from the explanted implant plates. As the first step they were equilibrated at the PBS (pH 7.4) solution for 30 minutes and then transferred to pH 5 buffer. In around 3-5 minutes the color of the gel changed to its acidic color. After changing the equilibrated hydrogels at pH 5 to PBS, the color change was observed. The basic color was observed after 25-30 minutes. Therefore, this study shows that the sensor hydrogel was responsive and reversible even after explanting. Reversibility studies were also carried out on the rod sensors. For Rabbit 1, the rod sensor was changing color as expected from pH 7.4 to pH 5, But the color of the rod wasn't fully reversible to the initial color at pH 7.4. Moreover, the rod explanted from Rabbit 1& 2 had a layer of tissue which was tightly adhered to the

surface of the sensor membrane. Therefore, it was harder to monitor any color changes. But the Rabbit 3 rod sensor was exhibiting a very distinct color change at basic and acidic pHs. While carrying out the experiment, it was made sure to keep it little longer in the specific buffer to equilibrate. After the final step of changing, it to pH 7.4 buffer, the sensors were incubated overnight to look for any change in color. But no significant difference of the basic color was observed. The color changes were compared to an unused neutral rod sensor while taking pictures for Rabbit 3. The figure below shows all the compiled photos for the reversibility study. Although it was harder to observe the changes for the Rabbit 1 and 2 sensors (due to the tissue adhered to the sensor), a clear color changes were observed for changing from pH 7.4 to pH 5 buffer and from pH 5 to pH 7.4 buffer. Which confirms the rod sensors were behaving reversible after extraction.

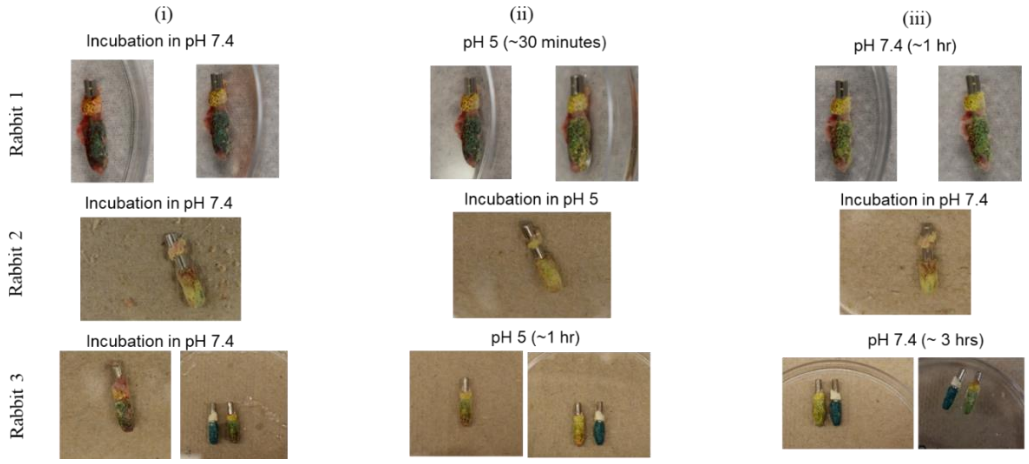

Figure 3.20: Reversibility studies for explanted rod sensors (i) The sensor incubation in the pH 7.4 buffer for Rabbits 1,2 and 3. (ii) The sensor incubation in the pH 5 buffer for Rabbits 1,2 and 3. (iii) The sensor incubation again in the pH 7.4 buffer for Rabbits 1,2 and 3 (For Rabbit 3, the rod sensors were compared to the initial color of a fabricated neutral sensor).

This pre-pilot rabbit study was carried out using three rabbit models and only one animal was used to study each of the hypothesis. As this is a pre-pilot study, the animal use protocol (AUP) allowed to use two animals. But one of the previous animals didn't survive until the experiment is over. Therefore, we had to order two more animals to carry out the study (rabbits are social animals which should be housed with one or more other rabbits for company). Therefore, with minor amendments to the AUP, we decided to test the second hypothesis of implanting a sensor with pre-grown a biofilm. Generally, a pilot study is carried out to analyze the test procedure's feasibility before the full-scale study. As it is the initial step of an entire study, a smaller number of animals will be used.[30] We carried out this study reflecting all the testing procedures of the main study to validate the

feasibility of the experimental methods (performing the surgery, fabricating the sensors, bacterial concentration and etc) and imaging procedures. As mentioned previously, this is the first study to investigate the ability of using the XELCI imaging for monitoring the pH changes associated with implant associated infections through bone and tissue in vivo. We could confirm with this study that pH changes associated with implant associated infections can be monitored with XELCI imaging providing pH mapping of the local environment.

Determining how many animals should be used in an experiment is very important as smaller sample size will not provide the real effect occur in an experiment. A larger sample size which is larger than necessary will lead to waste of resources and ethical issues on the sacrificed animals.[31] There are three basic methods that we can use to calculate the sample size: 1) Traditional or common sense; 2) by power analysis; and 3) by Mead's resource equation. Most investigators try to decide sample sizes depending on similar work carried out by other experimentalists. By carefully studying the type of the experiment and other variables, this seems to be a sensible approach. Power analysis method use six variables (some of which requires prior knowledge and information) to carry out the calculations: such as 1) Provisional sample size, 2) power (specify 80-90 %) 3) significance level 4) sidedness 5) variability/ standard deviation and 6) estimated minimum detectable effect size. Once feeding this information in to specific software or using the variables manually in an equation, a researcher can determine the sample size in more scientifically.[31,32] The resource equation (E= Total number of animals – Total number of groups) will be useful to determine sample size when the expected standard deviations or

expected differences in values between groups are unknown or hard to find. Even though this method is easy to use it cannot be considered as scientific as power analysis.[32]

In this pre-pilot rabbit study, we didn't use a particular sex as our main objective was to test experimental procedures (imaging and sensor behavior) and surgery procedures can be implemented successfully aiming the subsequent pilot studies. We mainly focused on choosing New Zealand White rabbits (easily available and less aggressive) in certain weight range (~ 3-4 kg) and from both sex for housing them in the animal facility before surgery. Choosing a healthy large animal in this range will allow an experimental model to withstand surgical trauma, preventing serious post operative problems and leading to a better survival rate. Compared to other species such as primates the rabbits have faster skeletal change and bone turnover, and they are commonly used for screening implants prior testing in a larger animal. We also believe that the sex related variables in an animal will not significantly affect developing an infection in the intramedullary cavity or on the bone surface. Because with this study we didn't notice any sex dependent changes occur in while developing the infections inside the intramedullary cavity. Some investigators reported using female sex as it is the biologically stronger sex.[33] As we have used both sex in the infection model and eventually both the animal developed infections in the intramedullary cavity and surrounding area suggests that with the bacterial dose, we have inoculated can give rise to an infection locally. Usually, when we carry out the pilot and full-scale study, several animals (~10-12) will be used to test the hypothesis in both control and test experiments. In full scale studies, we will use at least 5-6 animals in a group as control models as well as similar number of animals as the test models (infected studies).

3.6 Conclusions and Future work

In this pre-pilot rabbit study, we studied the pH changes occur in the tibial intramedullary canal during an event of osteomyelitis with a control rabbit model. To mimic osteomyelitis in vivo, two approaches were chosen. For one of the models, the tibia of left leg was reamed and inoculated with Staphylococcus aureus to develop an infection in the intramedullary canal at the time of the surgery while for the other model, a pre-infected sensor was implanted at the time of the surgery. Previously in the XELCI imaging, we only mapped the pH of the surface of the bone. But with this pre-pilot rabbit study, it is demonstrated that we were able to detect the pH variations through bone and tissue with the modifications to the XELCI imaging system.

According to the analysis of acquired XELCI images during the rabbit study, the control rabbit with sterile implant remains uninfected during the time of study while the two other infected models were showing reduction in the pH varying from 5.5- 7. Although the trend of the pH variations was different for each infected model, the acidic environment has prevailed until the day of the postmortem.

The postmortem observations exhibit that the control rabbit model remains uninfected during the study while there were clear signs of infections (abscess and white pus) for both infected models. Also, the postmortem pH changes suggested that the control rabbit model was uninfected as the gel sensors and surrounding pH were basic while both infected models show slightly acidic pH for top of the tibia and sensor surface.

In some instances, the MATLAB analysis is subject to systematic errors in interpreting the pH variations, especially while imaging through different thicknesses of

tissue. Where multiple reference regions are available, the MATLAB script can be modified to account for the tissue thickness variations via a gradient normalization approach. For the implant plates, we can introduce a reference line along the implant and for a rod sensor, the reference regions can be placed on both ends of the sensor to account for those variations.

In previous infected rabbit studies, we use implant plate sensors to monitor pH variations with pH sensitive gel layers. But the sensors weren't behaving as expected and we didn't see pH variations during an infection on the surface of the bone.[6] Even though we artificially created the cavity environment, the acidic metabolites were neutralized throughout the imaging days.[8] As we have a more enclosed environment in the intramedullary cavity, we wanted to confirm that the pH changes could be imaged with the new version of the rod sensor with pH sensitive gel layers. While transitioning to the intramedullary rod pH detection, we changed the location of the sensor implantation as well as the type of the sensor (implant plate with layered sensor films vs a coated stainless steel rod sensor). Thus, it is unclear to what extent the pH drop we observed for infection in the intramedullary canal was due to differences in biology of the bone vs. soft tissue above the plate (or periosteum below), or due to differences in the sensor itself. Clearly, the biology could be different, and the sensor geometry and thickness could also plausibly affect reading: A thicker sensor responds more slowly because analytes need to diffuse into its thickness, and more importantly, analytes can escape to adjacent regions averaging out heterogeneity finer than the scale of the sensor thickness. This applies to pH (where any holes in the biofilm or region close to blood vessels could allow the acid to diffuse out),

and also to accumulation/escape of other biomolecules such as oxygen or quorum sensing molecules. Although a thick sensor would respond if the entire tissue and biofilm were acidic, it is possible that it would not readily detect if there were small regions on the bottom of the biofilm that were acidic (e.g., Fig 1.2).

To see to what extent sensor shape could account for the pH drop in the intramedullary canal (or the lack of response on the plate), for future experiments (outlined in Chapter 5), we design a new rod sensor version to incorporate the gel sensors as layers. The proposed version of the intramedullary rod is as follows (Figure 3.21). With the newer rod sensor, we can also test the behavior of these layered film sensors in a more enclosed environment than the implanted infected sensor on open bone surface. It will allow us to study and understand both locations' chemical environment. The pH sensitive gel layers over the scintillator film are about 400 -500 μm thick. They are thicker pH sensitive layers compared to the dip coated rod sensor. In this new design, two of the reference regions will be at the ends of the rod sensor while the pH sensing gel sensor in the middle chamber. Two reference regions will be used to account for tissue thickness differences while imaging.

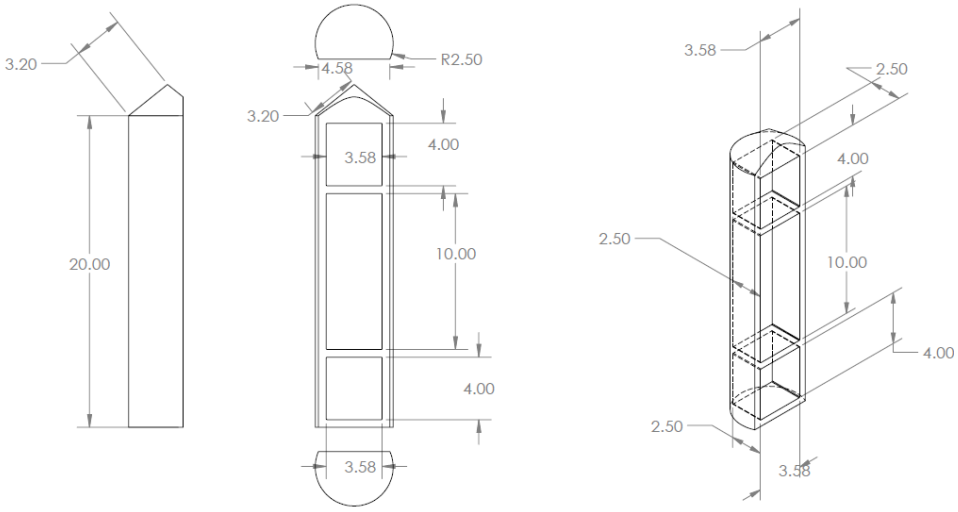

Figure 3.21: The Solidworks design of new version of the intramedullary rod sensor (All the dimensions are in mm).

In conclusion, intramedullary rod associated infection studies via XELCI allowed us to acquire high resolution imaging of pH variations in a closed system through thick tissue. The XELCI images shows clear edges of sensor also along with the sensor abnormalities. Moreover, we observed more encouraging data and XELCI imaging showed clear drop of pH in the intramedullary sensor. The control sensors implanted on the bone surface of the femur showed more constant pH throughout but generally, the agarose layer sometimes affected both the measurements in XELCI and postmortem. Here we are reporting first high-resolution chemical imaging through bone and tissue which allow us to study interesting biochemistry during intramedullary rod associated infection.

3.7 References

(1) Magill, S. S.; Edwards, J. R.; Bamberg, W.; Beldavs, Z. G.; Dumyati, G.; Kainer, M. A.; Lynfield, R.; Maloney, M.; McAllister-Hollod, L.; Nadle, J.; Ray, S. M.; Thompson, D. L.; Wilson, L. E.; Fridkin, S. K. Multistate Point-Prevalence Survey of Health Care–Associated Infections. *N. Engl. J. Med.* **2014**, *370* (13), 1198–1208. https://doi.org/10.1056/NEJMoa1306801.

(2) Klevens, R. M.; Edwards, J. R.; Richards, C. L.; Horan, T. C.; Gaynes, R. P.; Pollock, D. A.; Cardo, D. M. Estimating Health Care-Associated Infections and Deaths in U.S. Hospitals, 2002. *Public Health Rep.* **2007**, *122* (2), 160–166. https://doi.org/10.1177/003335490712200205.

(3) Li, B.; Webster, T. J. Bacteria Antibiotic Resistance: New Challenges and Opportunities for Implant-Associated Orthopedic Infections: BACTERIA ANTIBIOTIC RESISTANCE. *J. Orthop. Res.* **2017**. https://doi.org/10.1002/jor.23656.

(4) Oliveira, W. F.; Silva, P. M. S.; Silva, R. C. S.; Silva, G. M. M.; Machado, G.; Coelho, L. C. B. B.; Correia, M. T. S. Staphylococcus Aureus and Staphylococcus Epidermidis Infections on Implants. *J. Hosp. Infect.* **2018**, *98* (2), 111–117. https://doi.org/10.1016/j.jhin.2017.11.008.

(5) Arciola, C. R.; Alvi, F. I.; An, Y. H.; Campoccia, D.; Montanaro, L. Implant Infection and Infection Resistant Materials: A Mini Review. *Int. J. Artif. Organs* **2005**, *28* (11), 1119–1125. https://doi.org/10.1177/039139880502801109.

(6) Uzair, U.; Benza, D.; Behrend, C. J.; Anker, J. N. Noninvasively Imaging PH at the Surface of Implanted Orthopedic Devices with X-Ray Excited Luminescence Chemical Imaging. *ACS Sens.* **2019**, *4* (9), 2367–2374. https://doi.org/10.1021/acssensors.9b00962.

(7) Uzair, U.; Johnson, C.; Beladi-Behbahani, S.; Rajamanthrilage, A. C.; Raval, Y. S.; Benza, D.; Ranasinghe, M.; Schober, G.; Tzeng, T.-R. J.; Anker, J. N. Conformal Coating of Orthopedic Plates with X-Ray Scintillators and PH Indicators for X-Ray Excited Luminescence Chemical Imaging through Tissue. *ACS Appl. Mater. Interfaces* **2020**, *12* (47), 52343–52353. https://doi.org/10.1021/acsami.0c13707.

(8) Uzair, U. A PH Sensor for Non-Invasive Detection and Monitoring of PH Changes During Implant-Associated Infection Using X-Ray Excited Luminescence Chemical Imaging. Ph.D., Clemson University, Ann Arbor, 2020.

(9) Swenson, O.; Claff, C. L. Changes in the Hydrogen Ion Concentration of Healing Fractures. *Proc. Soc. Exp. Biol. Med.* **1946**, *61* (2), 151–154.

(10) Konttinen, Y. T.; Takagi, M.; Mandelin, J.; Lassus, J.; Salo, J.; Ainola, M.; Li, T.-F.; Virtanen, I.; Liljeström, M.; Sakai, H.; Kobayashi, Y.; Sorsa, T.; Lappalainen, R.; Demulder, A.; Santavirta, S. Acid Attack and Cathepsin K in Bone Resorption Around Total Hip Replacement Prosthesis. *J. Bone Miner. Res.* **2001**, *16* (10), 1780–1786. https://doi.org/10.1359/jbmr.2001.16.10.1780.

(11) Esmonde-White, K. A.; Esmonde-White, F. W. L.; Holmes, C. M.; Morris, M. D.; Roessler, B. J. Alterations to Bone Mineral Composition as an Early Indication of

Osteomyelitis in the Diabetic Foot. *Diabetes Care* **2013**, *36* (11), 3652–3654. https://doi.org/10.2337/dc13-0510.

(12) Shen, Y.; Liu, W.; Wen, C.; Pan, H.; Wang, T.; Darvell, B. W.; Lu, W. W.; Huang, W. Bone Regeneration: Importance of Local PH—Strontium-Doped Borosilicate Scaffold. *J. Mater. Chem.* **2012**, *22* (17), 8662. https://doi.org/10.1039/c2jm16141a.

(13) Kolar, P.; Gaber, T.; Perka, C.; Duda, G. N.; Buttgereit, F. Human Early Fracture Hematoma Is Characterized by Inflammation and Hypoxia. *Clin. Orthop.* **2011**, *469* (11), 3118–3126. https://doi.org/10.1007/s11999-011-1865-3.

(14) Cao, S.; Liu, P.; Zhu, H.; Gong, H.; Yao, J.; Sun, Y.; Geng, G.; Wang, T.; Feng, S.; Han, M. Extracellular Acidification Acts as a Key Modulator of Neutrophil Apoptosis and Functions. *PLoS One* **2015**, *10* (9), e0137221.

(15) Lardner, A. The Effects of Extracellular PH on Immune Function. 9.

(16) Silver, I.; Murrills, R.; Etherington, D. Microelectrode Studies on the Acid Microenvironment beneath Adherent Macrophages and Osteoclasts. *Exp. Cell Res.* **1988**, *175* (2), 266–276.

(17) Lüthje, F. L.; Jensen, L. K.; Jensen, H. E.; Skovgaard, K. The Inflammatory Response to Bone Infection – a Review Based on Animal Models and Human Patients. *APMIS* **2020**, *128* (4), 275–286. https://doi.org/10.1111/apm.13027.

(18) Allan, V. J. M.; Macaskie, L. E.; Callow, M. E. Development of a PH Gradient within a Biofilm Is Dependent upon the Limiting Nutrient. 7.

(19) Xiao, Y.; Wu, S.; Yang, Z.-H.; Wang, Z.-J.; Yan, C.-Z.; Zhao, F. In Situ Probing the Effect of Potentials on the Microenvironment of Heterotrophic Denitrification

Biofilm with Microelectrodes. *Chemosphere* **2013**, *93* (7), 1295–1300. https://doi.org/10.1016/j.chemosphere.2013.06.065.

(20) Nakata, E.; Yukimachi, Y.; Nazumi, Y.; Uwate, M.; Maseda, H.; Uto, Y.; Hashimoto, T.; Okamoto, Y.; Hori, H.; Morii, T. A Novel Strategy to Design Latent Ratiometric Fluorescent PH Probes Based on Self-Assembled SNARF Derivatives. *RSC Adv* **2014**, *4* (1), 348–357. https://doi.org/10.1039/C3RA43928C.

(21) Villano, D.; Romdhane, F.; Irrera, P.; Consolino, L.; Anemone, A.; Zaiss, M.; Dastrù, W.; Longo, D. L. A Fast Multislice Sequence for 3D MRI-CEST PH Imaging. *Magn. Reson. Med.* **2021**, *85* (3), 1335–1349.

(22) Wang, F.; Raval, Y.; Tzeng, T. J.; Anker, J. N. X-Ray Excited Luminescence Chemical Imaging of Bacterial Growth on Surfaces Implanted in Tissue. *Adv. Healthc. Mater.* **2015**, *4* (6), 903–910.

(23) Chen, H.; Rogalski, M. M.; Anker, J. N. Advances in Functional X-Ray Imaging Techniques and Contrast Agents. *Phys. Chem. Chem. Phys.* **2012**, *14* (39), 13469. https://doi.org/10.1039/c2cp41858d.

(24) Ash, C.; Dubec, M.; Donne, K.; Bashford, T. Effect of Wavelength and Beam Width on Penetration in Light-Tissue Interaction Using Computational Methods. *Lasers Med. Sci.* **2017**, *32* (8), 1909–1918. https://doi.org/10.1007/s10103-017-2317-4.

(25) Anderson, R. R.; Parrish, J. A. The Optics of Human Skin. *J. Invest. Dermatol.* **1981**, *77* (1), 13–19. https://doi.org/10.1111/1523-1747.ep12479191.

(26) Young, A. R. Chromophores in Human Skin. *Phys. Med. Biol.* **1997**, *42* (5), 789–802. https://doi.org/10.1088/0031-9155/42/5/004.

(27) Andriole, V. T.; Nagel, D. A. Chronic Staphylococcal Osteomyelitis: An Experimental Model'. 7.

(28) Trampuz, A.; Zimmerli, W. Diagnosis and Treatment of Infections Associated with Fracture-Fixation Devices. *Injury* **2006**, *37* (2), S59–S66. https://doi.org/10.1016/j.injury.2006.04.010.

(29) Odekerken, J. C.; Arts, J. J.; Surtel, D. A.; Walenkamp, G. H.; Welting, T. J. A Rabbit Osteomyelitis Model for the Longitudinal Assessment of Early Post-Operative Implant Infections. *J. Orthop. Surg.* **2013**, *8* (1), 38. https://doi.org/10.1186/1749-799X-8-38.

(30) In, J. Introduction of a Pilot Study. *Korean J. Anesthesiol.* **2017**, *70* (6), 601–605.

(31) Charan, J.; Kantharia, N. How to Calculate Sample Size in Animal Studies? *J. Pharmacol. Pharmacother.* **2013**, *4* (4), 303–306.

(32) Festing, M. F. On Determining Sample Size in Experiments Involving Laboratory Animals. *Lab. Anim.* **2018**, *52* (4), 341–350. https://doi.org/10.1177/0023677217738268.

(33) Calasans-Maia, M. D.; Monteiro, M. L.; Áscoli, F. O.; Granjeiro, J. M. The Rabbit as an Animal Model for Experimental Surgery. *Acta Cir. Bras.* **2009**, *24*, 325–328.

CHAPTER 4

MEASURING ORTHOPEDIC PLATE STRAIN TO TRACK BONE HEALING USING A FLUIDIC SENSOR READ VIA PLAIN RADIOGRAPHY

4.1 Abstract

We describe a fluidic X-ray visualized strain indicator under applied load (X-VISUAL) to quantify orthopedic plate strain and inform rehabilitative care. The sensor comprises a polymeric device with a fluidic reservoir filled with a radio-dense fluid (cesium acetate) and an adjoining capillary wherein the liquid level is measured. A stainless-steel lever attaches to the plate and presses upon the acrylic bulb with a displacement proportional to plate bending strain. The sensor was attached to a plate in a Sawbones composite tibia mimic and a human cadaveric tibia. An osteotomy model (5 mm gap) was used to simulate an unstable osteotomy, and allograft repair to simulate a stiffer healed fracture. The cadaveric and Sawbones tibia were cyclically loaded five times (0 - 400 N) using a mechanical test stand, and fluid displacement was measured from plain radiographs. The fluid displacement was compared to applied axial force and displacement. The sensor displayed reversible and repeatable behavior with a slope of 0.096 mm/kg and fluid level noise of 50 to 80 micrometer (equivalent to 5-10 N). The allograft-repaired composite fracture was 13 times stiffer than the unstable fracture. An analysis of prior external fracture fixation studies and fatigue curves for internal plates indicates that the threshold for safe weight bearing should be $1/5^{th}$ -$1/10^{th}$ of the initial bending for an

unstable fracture. The precision of our device (<2% body weight) should thus be sufficient to track fracture healing from unstable through safe weight bearing.

4.2 Introduction

Two of the most common complications associated with fracture healing are bone non-union and orthopedic implant associated infections. Implant associated infections can also be directly related to the bone non-union as it can cause implant loosening which hinders the fracture healing process. Once the increase in stiffness has ceased, it can be an indicative of bone non-union due to infection. In the earlier chapters, I introduced the XELCI imaging which uses X-ray as the exciting light source and its' applications as a possible solution for detecting infections and mapping pH variations throughout the fracture healing process. Herein, I describe a hydromechanical strain sensor to monitor the stiffness of the healing tibial fracture via plain radiography. This work is published in IEEE Transactions in the biomedical engineering journal in 2021 (Rajamanthrilage et al.: "Measuring Orthopedic Plate Strain to Track Bone Healing Using a Fluidic Sensor Read via Plain Radiography". IEEE Transactions in Biomedical Engineering. (June 2021)).

Following fracture fixation surgery, patients commonly ask, "Am I healing normally, and when will it be safe to resume weight bearing?" These are important questions because premature weight bearing can lead to refracture and hardware failure, while unnecessary delayed return to activities can affect quality of life. About five percent of the annual estimated 2 million fracture fixation surgeries in the United States result in delayed or impaired healing due to various reasons,[1,2] with nearly 100,000 non-unions

annually.[3–5] In particular, tibial fracture is the most common long bone injury, and non-union is relatively prevalent in part due to the small tissue envelope.[6,7] For slowly healing patients at risk of disabling nonunion, physicians can prescribe restrictive/assisted weight bearing,[8] altered physical therapy regimes, tests to detect and address underlying metabolic disorders, apply biologics such as teriparatide,[9] prescribe electrical, ultrasound, or shockwave bone stimulation therapies, or perform revisions before hardware failure.[10–12] However, these are unnecessary or contraindicated in most patients, who heal normally. Since no single time frame applies to all patients, individual assessments are necessary.

This study introduces an implantable hydraulic sensor which can easily attach to the plate to quantify tibial plate bending during the fracture healing process via plain radiography (X-ray projection imaging). Plain radiography is ubiquitously available in hospitals and routinely used to observe the hardware and fracture callus, however, it conventionally has limited value for quantification of fracture healing.[13,14] Plain radiography can help physicians assess fracture healing and detect pathologies because of its excellent contrast for hardware/bone, low cost, extensive availability, rapidity, and lower radiation exposure compared to computed tomography (CT). However, image interpretation is qualitative, subjective, and correlates poorly with mechanical properties such as stiffness or stability.[15,16] Previously, we made a plate attachment with a tungsten pin that moved against a scale to quantitatively indicate plate bending via plain radiography.[17] However, the 12 cm long pin was surgically cumbersome, and reducing pin length would require a protruding scale and much smaller displacement. To address this

concern, herein we developed a smaller device which uses hydraulic gain to amplify the signal from plate bending and increase precision for tracking healing bone.

4.3 Device operating principle

As a fracture heals and the callus stiffens, it increasingly shares load with the plate, which therefore bends less under the same load. Orthopedic plate deflection under load thus provides an objective metric for monitoring the fracture healing. Our X-VISUAL device reads plate deflection as a change in the fluid level within a channel. The 0.57 ml of fluid in the sensor is a radio-dense cesium acetate solution (85 wt % in water) and is apparent on radiographic images. Cesium acetate is a colorless, hygroscopic, ionic compound with low toxicity which has been used for medical applications and previous reports indicate that it is relatively safe for in vivo use.[18] The hydraulic action of the sensor provides mechanical gain (fluid level change/plate deflection between lever attachment and bulb) based on the ratio of the bulb's cross-sectional area to the channel's cross-sectional area. Fig. 1 illustrates how the sensor works. With no load applied to the fractured bone, the fluid level is fixed by the position of a lever impinging on the bulb (Fig. 1 (a)). When the bone is compressed under axial load, the fracture closes, and the plate bends because the plate is off the central axis (Figure 4.1 (b)). This bending action releases the stainless-steel lever away from the fluid reservoir pulling fluid from the channel and thus reducing the fluid level. Figure 4.1 (b) and Figure4.1 (d) are photos of hydraulic sensor with and without load. While axial compression is applied here, the same principle would apply to axial tension or direct bending moments

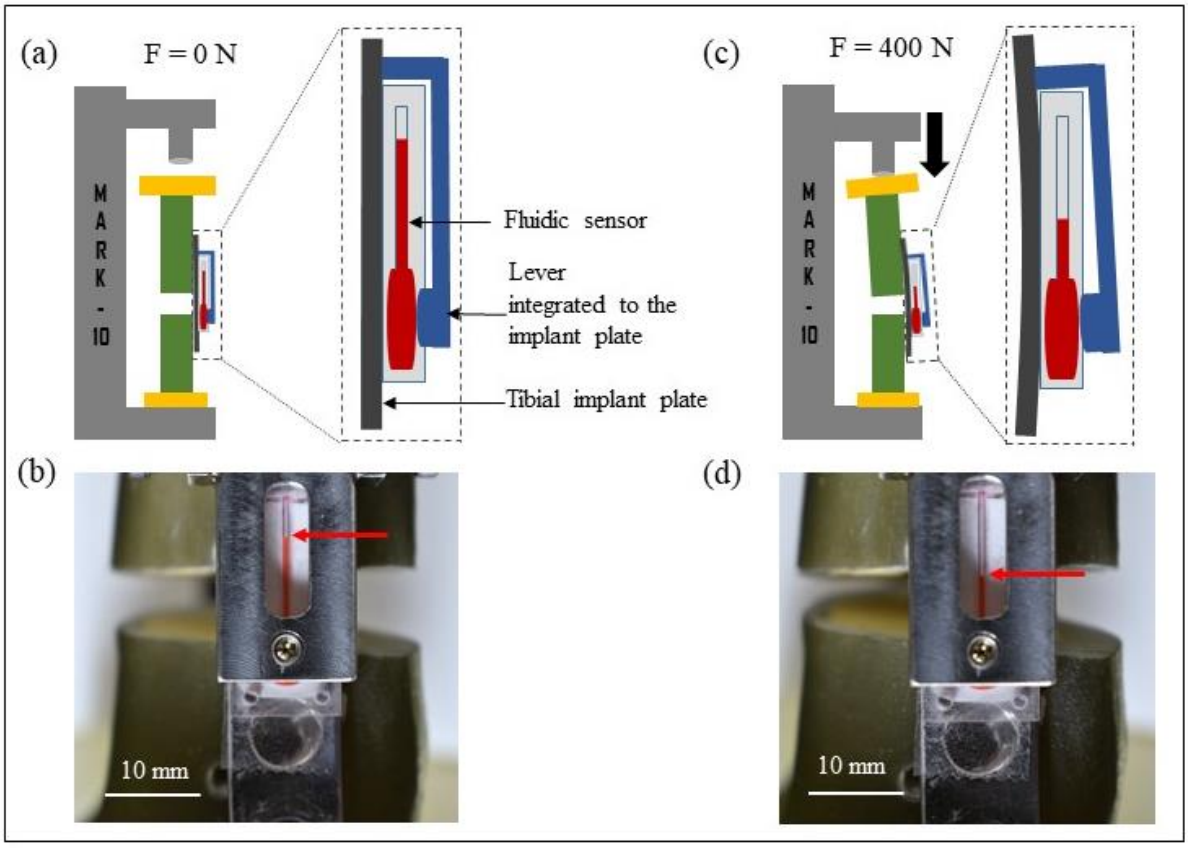

Figure 4.1: Sensor mechanism. a) Schematic of fluidic sensor at 0 N. b) Corresponding photograph in a Sawbones tibial mimic (arrow shows fluid level). c) Schematic of fluidic sensor at 400 N: plate bending displaces the lever, releasing the bulb and lowering the fluid level. d) Corresponding photograph with fluid level at 400 N. [Reproduced with the permission from **Rajamanthrilage A.C.** et al.: "Measuring Orthopedic Plate Strain to Track Bone Healing Using a Fluidic Sensor Read via Plain Radiography". IEEE Transactions in Biomedical Engineering. (June 2021)].

4.4 Device fabrication

The passive fluidic sensor is comprised of two components, an acrylic component containing a disc-shaped fluid reservoir (bulb) attached to a millimeter diameter channel for reading fluid level, and a stainless steel mechanical lever which presses on the bulb and alters the fluid level in the channel according to degree of plate bending. Technical drawings are provided in below (Figure 4.2). The stainless-steel lever component was designed to mount to an orthopedic plate and included an adjustable set screw to press on the fluid reservoir of the sensor. The acrylic component was machined in two halves and glued together using acrylic glue. Then, the indicator fluid was introduced into the bulb using a 27-gauge needle. Finally, the end of the channel was sealed to prevent escape of the fluid during operation or influx of bodily fluids.

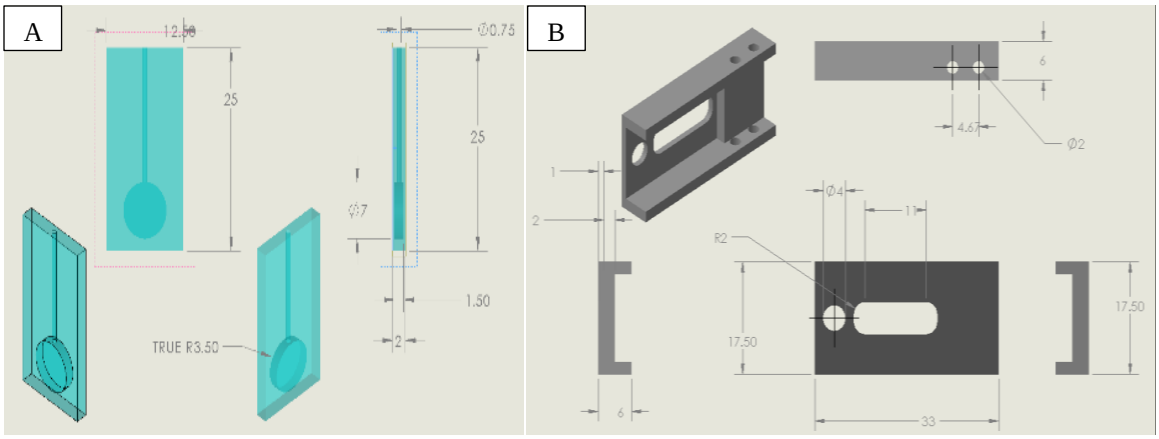

Figure 4.2:SolidWorksTM designs of two main parts of the hydraulic sensor showing different views of the designs A) bulb and fluid capillary sensor; B) lever part of the sensor with one end which attaches to the plate, and a second end which presses on the bulb with a pressure and displacement which depends on the degree of plate bending. (All measurements are in mm) [Reproduced with the permission from **Rajamanthrilage A.C.** et al.: "Measuring Orthopedic Plate Strain to Track Bone Healing Using a Fluidic Sensor Read via Plain Radiography". IEEE Transactions in Biomedical Engineering. (June 2021)].

4.5 Sensor monitoring on the tibial implant plate

An unstable fracture was created at the proximal shaft of a Sawbones® tibia composite mimic (Pacific Research Laboratories, Inc., Vashon, WA, Sawbones® Model #3402). An internal fixation plate (Smith and Nephew, Lawrenceville, GA, 4.5 mm tibial locking compression plate) was employed to fix the proximal fracture. Then the hydraulic sensor was attached to the tibial plate and centered over the fracture. The lever was attached to the implant plate using screws that gripped from both sides.

4.6 Measuring fluid level under load in a composite sawbones tibial model

The fluidic sensor was tested on a fractured tibia Sawbones® model by monitoring the fluid displacement (mm) against the applied force (N) using an ESM-303 motorized tension/compression test stand (Mark-10 Corp., Copiague, NY) to directly evaluate the mechanical properties of the fracture site. An axial compressive load of 0 through 400 N was applied to the proximal end of the fractured model. For context, 400 N is approximately one-half body weight for an 80 kg patient. For analysis in plain radiography, the fluid reservoir was filled with cesium acetate (85 wt%).

The initial fluid level was adjusted by the turning a bottom screw attached to the lever until the "no load" level was at the top of the channel. This initial fluid level was measured in radiography, and all other fluid level displacements were calculated by subtracting this initial level. Next, the axial load on the tibia was progressively increased (loading) up to 400 N and progressively decreased (unloading) to 0 N. One set of increasing load points and one set of decreasing load points were considered as one full cycle of the study. Reproducibility of the hydraulic sensor was examined by executing five continuous loading and unloading cycles. The same procedure was carried out on a bone with an allograft (segment cut out from another Sawbones® tibia) pushed into the fracture gap to simulate a repaired and reduced fracture. While such repairs are rare because traumatic fractures rarely have bone segment ejection, it simulates good fracture reduction and shows how stiffness would be expected to improve as the callus stiffens during healing. The allograft-repaired fracture was cycled over five loading cycles as with the unstable fracture. We have used NEXT II digital radiography software system (CA, USA) and Poskom VET-

20 BT Hybrid-battery powered portable X-ray source (Medicaleconet, Oberhausen, Germany) for loading experiments.

A fluidic sensor filled with radio-dense cesium acetate solution (85% wt %) was used for radiographic imaging. Figure 4.3 (a) shows the sequence of plain radiographs for the first of five linearly increasing and decreasing load cycles (0-400 N and back) with a Sawbones® composite tibial mimic with a 5 mm osteotomy. Figure 4.3 (b) shows the graphs of applied force and fluid displacement (difference from no load level) versus image number. Almost identical maximum and minimum fluid displacements were observed for each cycle indicating the reversible behavior of the fluidic sensor, with a small but consistent fluid height asymmetry at intermediate force levels indicating some hysteresis. The hysteresis curve (Figure 4.3 (c)) for fractured bone has a maximum hysteresis of ~20 N and slope of 0.096 mm/kg. During loading, average displacements were ranged from 0.00 ± 0.01 mm at 0 N through 3.935 ± 0.001 mm at 400 N. The mean noise level (loading and unloading) was 0.02 mm (0.3 kg) and maximum was 0.06 mm (0.6 kg). Average displacements are tabulated and are presented in Table 1.

Table 4.1: Average displacements at different loads for Sawbones® tibia models with an unstable fracture

Loading		Unloading	
Load applied (N)	Displacement (mm)	Load applied (N)	Displacement (mm)
0	0.00 ± 0.01	400	3.935 ± 0.001
100	0.70 ± 0.04	300	2.82 ± 0.01
200	1.66 ± 0.04	200	1.88 ± 0.04
300	2.60 ± 0.02	100	0.87 ± 0.06
400	3.935 ± 0.001	0	0.00 ± 0.01

Table 4.2: Average displacements at different loads for Sawbones® tibia models with an allograft-repaired fracture

Loading		Unloading	
Load applied (N)	Displacement (mm)	Load applied (N)	Displacement (mm)
0	0.00 ± 0.09	400	0.31 ± 0.08
100	0.04 ± 0.04	300	0.23 ± 0.07
200	0.11 ± 0.07	200	0.10 ± 0.12
300	0.14. ± 0.06	100	0.14 ± 0.08
400	0.31. ± 0.08	0	0.00 ± 0.07

We repeated the experiment after introducing an allograft of the same Sawbones® material to form a much stiffer construct under axial compression which simulated bone healing (or surgical interventions occasionally used to stabilize the fracture). In comparison to the fractured bone, the allograft –repaired bone showed approximately 13x less fluid displacement on radiographs with cyclic loading. The fluid displacement and cyclic loading is graphed and showed in Figure 4.3 (b) and 4.3 (c). The radiographs are shown in the Figure 4.4 below. The fluid displacement at 400 N (maximum load) was 0.31 ± 0.07 mm, corresponding to a slope of 0.0076 mm/kg.

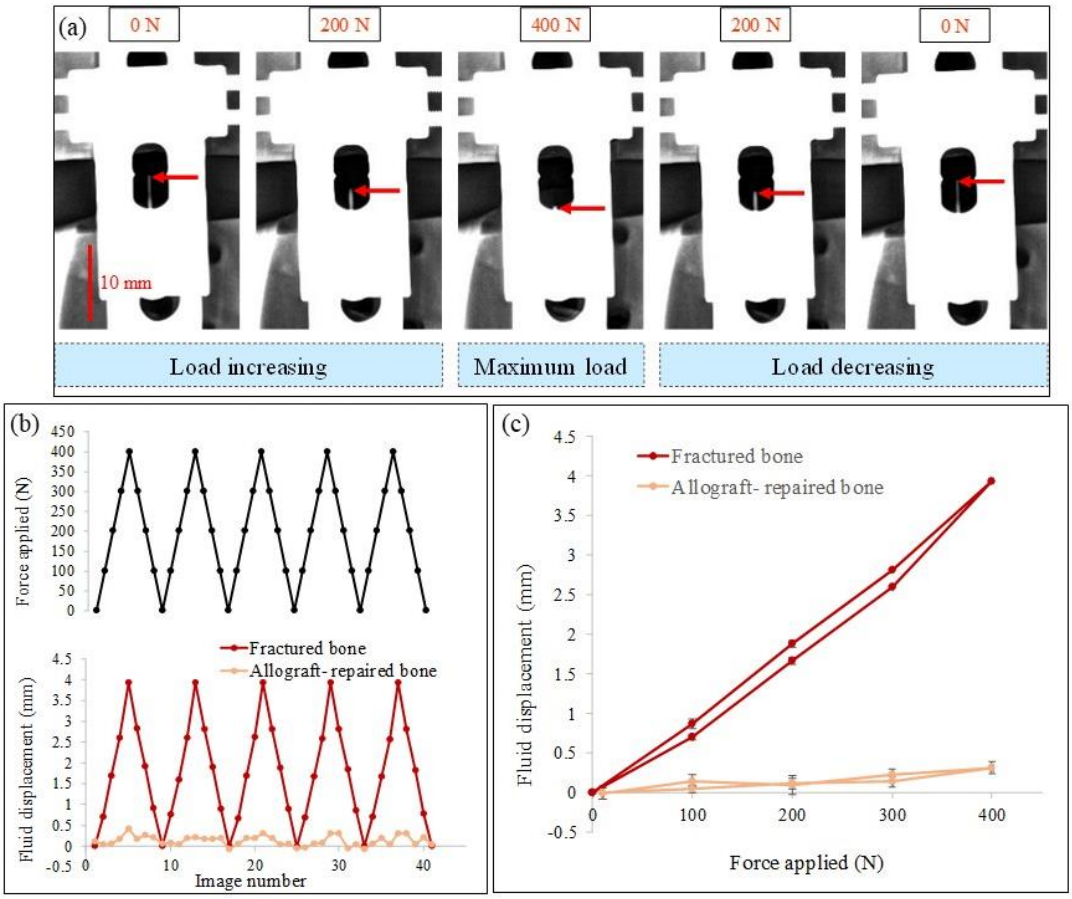

Figure 4.3: Sensor reading during five load cycles for a plated cadaveric tibia with an unstable fracture. a) Plain radiographs showing the fluid level changes with vs. applied load through one load cycle (red arrow shows fluid level). b) Force applied and fluid displacement vs. image number. c) Five-cycle-average fluid displacement vs. applied force. [Reproduced with the permission from **Rajamanthrilage A.C.** et al.: "Measuring Orthopedic Plate Strain to Track Bone Healing Using a Fluidic Sensor Read via Plain Radiography". IEEE Transactions in Biomedical Engineering. (June 2021)].

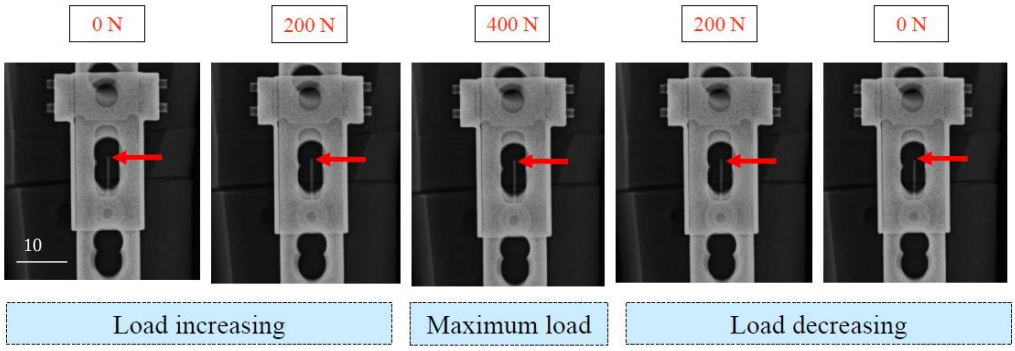

Figure 4.4: Plain radiographs showing the fluid level changes (little or no change) for allograft- repaired tibia with respect to applied load through one cycle. (Red arrow points to fluid level) [Reproduced with the permission from **Rajamanthrilage A.C.** et al.: "Measuring Orthopedic Plate Strain to Track Bone Healing Using a Fluidic Sensor Read via Plain Radiography". IEEE Transactions in Biomedical Engineering. (June 2021)].

4.7 Measuring fluid level under load in a fractured human cadaveric tibial specimen

The experiments were carried out according to the Clemson University Institutional Biosafety Committee (IBC) as well as following relevant guidelines and regulations. Human cadaveric specimens were obtained via the Hawkins Foundation (Greenville, SC) from Restore Life USA (Elizabethton, TN), a nonprofit donation program, and donors had consented their body to be used for medical education and research in accordance with the Uniform Anatomical Gift Act (UAGA). The fluidic sensor was filled with radiopaque fluid to visualize the fluid displacement via plain radiography. The sensor was later attached on

an orthopedic implant plate in human cadaver tibia model with an unstable proximal metaphyseal tibia fracture. The mechanical lever was attached over the fluidic sensor using screws on both sides of the plate. The loading and unloading cycles and the imaging procedure were carried out as in the Sawbones composite tibial specimen above. The fractured human cadaver tibia specimen was set up with the motorized tension/compression test stand for loading/unloading experiments as shown in the figure below (Figure 4.5). The tibia was loaded in compression from 10 through 400 N in 100 N increments for five consecutive loading/unloading cycles and the fluid level monitoring was done using plain radiography. Radiography was performed in Godley Snell Animal Research Center, Clemson University, Clemson, SC.

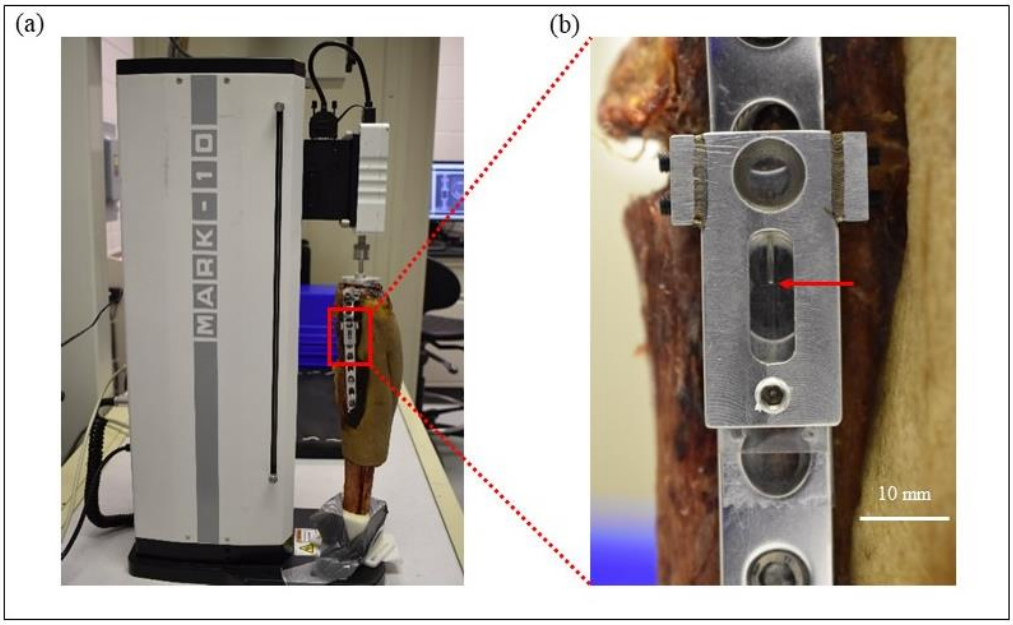

Figure 4.5: Photos of experimental setup for measuring plate strain on a cadaveric tibia with an unstable fracture. a) Fluidic sensor attached near the fracture gap. b) Zoomed-in view of the sensor (red arrow points to fluid level). [Reproduced with the permission from **Rajamanthrilage A.C.** et al.: "Measuring Orthopedic Plate Strain to Track Bone Healing Using a Fluidic Sensor Read via Plain Radiography". IEEE Transactions in Biomedical Engineering. (June 2021)].

The radiopaque fluid level changes of the fluidic sensor integrated on a fractured human cadaver tibia with an unstable fracture were monitored measured easily via plain radiography. While application of the increasing compressive loads, consistent decrease in the fluid level changes were observed. The fluid level also returned to the initial level while decreasing the compressive load. During cyclic loading, 0.9 mm of fluid displacement for 100 N was observed. Figure 4.6 (a) shows the series of plain radiographs obtained at each load Figure.4.6 (b) and 4.6 (c) are graphs showing the reproducibility of the fluid level

changes for five continuous cycles. The maximum hysteresis was 0.9 mm (or ~100 N). This was larger than in the Sawbones composite due to the more complex biomechanics of the fracture, including fibula and soft tissue. During loading and unloading cycles, average displacements were ranged from 0.04 ± 0.07 mm at 0 N through 3.43 ± 0.07 mm at 400 N. The overall slope was 0.084 mm/kg (comparable to 0.96 mm/kg for the unstable Sawbones model). The mean noise level was 0.08 mm (corresponding to 1. kg), and maximum was 0.16 mm (2 kg). The average noise level was higher in the cadaveric specimen than the composite, likely due to the presence of soft tissue and more radio dense bone. However, noise was still relatively low, ~2% of displacement at 400 N.

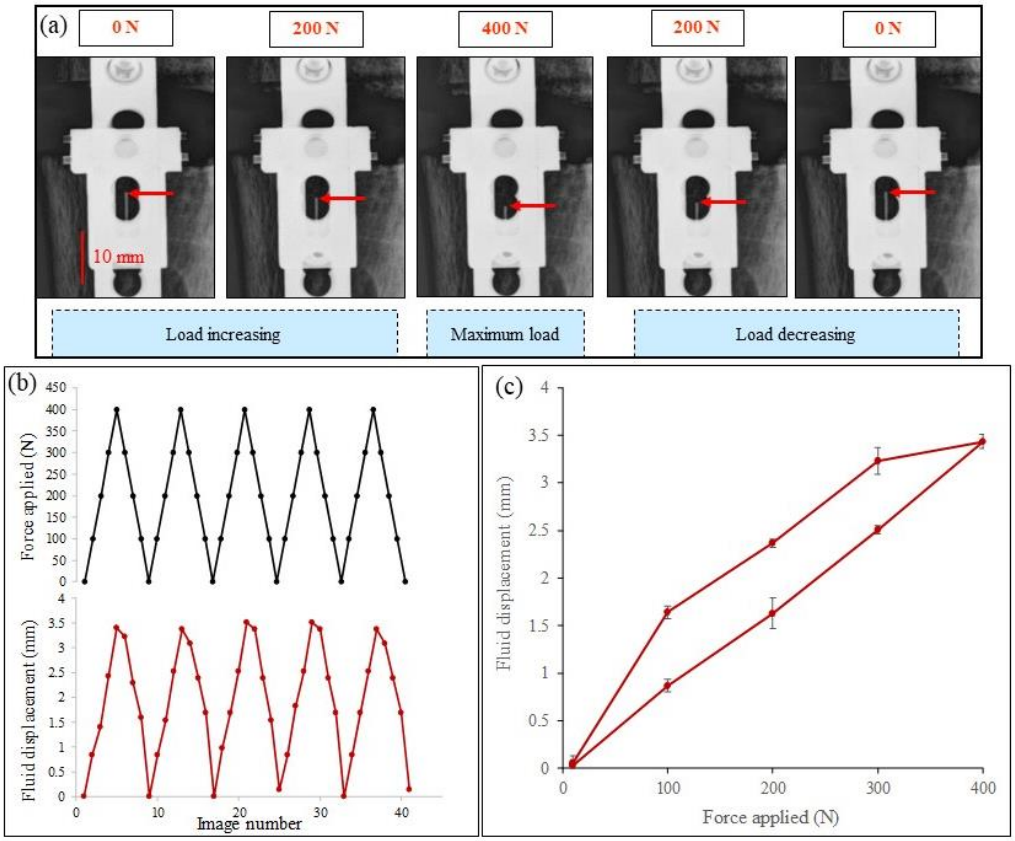

Figure 4.6: Sensor reading during five load cycles for a plated cadaveric tibia with an unstable fracture. a) Plain radiographs showing the fluid level changes with vs. applied load through one load cycle (red arrow shows fluid level). b) Force applied and fluid displacement vs. image number. c) Five-cycle-average fluid displacement vs. applied force. [Reproduced with the permission from **Rajamanthrilage A.C.** et al.: "Measuring Orthopedic Plate Strain to Track Bone Healing Using a Fluidic Sensor Read via Plain Radiography". IEEE Transactions in Biomedical Engineering. (June 2021)].

Table 4.3: Average displacements at different loads for Human cadaver tibia with an unstable fracture

Loading		Unloading	
Load applied (N)	Displacement (mm)	Load applied (N)	Displacement (mm)
0	0.03 ± 0.06	400	3.43 ± 0.07
100	0.87 ± 0.06	300	3.23 ± 0.14
200	1.63 ± 0.16	200	2.37 ± 0.04
300	2.51 ± 0.04	100	1.64 ± 0.07
400	3.43 ± 0.07	0	0.05 ± 0.07

4.8 Measuring fluid level at different angles and different magnifications

We conducted an experiment to see the effect of expected clinical variation in acquisition in angles and positions. We measured the fluid level at a series of different angles and positions/magnifications on a fractured *Sawbones*® tibia. Although variation in angle and position did not have a noticeable effect, the average fluid level in the angle study differed by 0.34 mm from the average in the position studies when no difference was expected (Figure 4.7 and 4.8). To make absolute measurements more reproducible, we added two radiopaque tantalum beads to serve as reference scale to measure fluid level against. The beads were placed on the plane of the fluid sensor and separated by 5 mm. The Ta bead incorporated sensor was only utilized in this experiment to determine angle and magnification dependence and not in prior cyclic loading experiments. The initial fluid level of the sensor was set to unloaded position and the X-ray source and detector were placed at constant positions. The sensor mounted fractured *Sawbones*® tibia was positioned at 6 different angles and X-ray imaging was done at each angle.

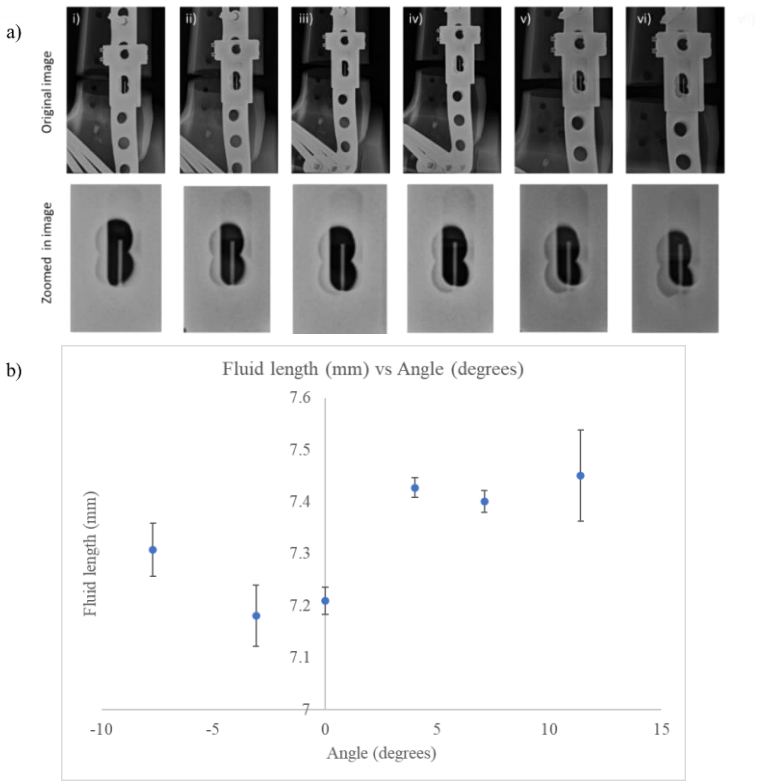

Figure 4.7: Fluid level measured at different angles of fractured Sawbones® tibia (fluidic sensor without Ta bead reference). a) Radiographs taken at different X-ray source angles i) through vi) respectively 7.7°, 3.1°, 0°, -4.1°, -7.1°, -11.4°. b) Measured fluid level (from top of bulb) vs angle. [Reproduced with the permission from **Rajamanthrilage A.C.** et al.: "Measuring Orthopedic Plate Strain to Track Bone Healing Using a Fluidic Sensor Read via Plain Radiography". IEEE Transactions in Biomedical Engineering. (June 2021)].

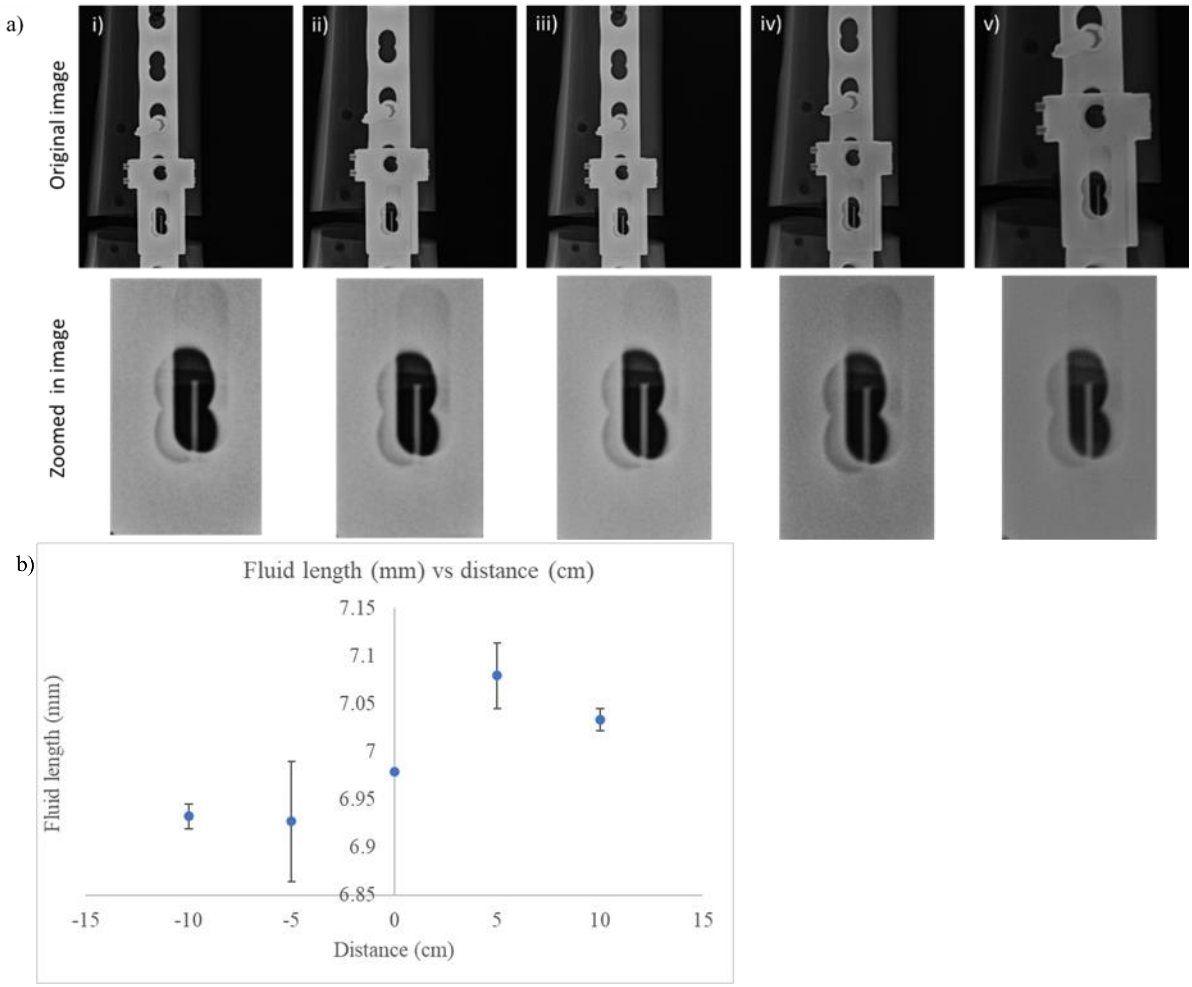

Figure 4.8: Fluid level measured at different positions and effective magnifications of fractured Sawbones® tibia (fluidic sensor without Ta bead reference). a) Radiographs of specimen positioned at different distances i) through v) respectively -10, -5, 0, 5, 10 cm. b) Measured fluid level vs specimen distance. [Reproduced with the permission from **Rajamanthrilage A.C.** et al.: "Measuring Orthopedic Plate Strain to Track Bone Healing Using a Fluidic Sensor Read via Plain Radiography". IEEE Transactions in Biomedical Engineering. (June 2021)].

To examine the fluid level at different magnifications, X-ray imaging was done at five different distances from the X-ray source to the *Sawbones*® tibia by keeping the detector and the X-ray source at the same position. To change the specimen angle, we placed absorbent rolls under the potted tibia, and measured the new angle relative to vertical (set as 0°). At each angle and position 3 radiographs were taken. In the specimens without a tantalum bead reference scale, fluid level was the fluid distance to the top of the bulb, normalized to the 33 cm lever length. With the tantalum bead scale, fluid level was fluid distance to the top Ta bead, normalized to the 5 cm spacing between the beads.

We studied how variation in tibia angle and magnification within clinical ranges would affect measurements on a fractured *Sawbones*® tibia specimen. Since patients can generally keep the tibial angle consistent within several degrees, and certainly within 15°, we measured a constant fluid level within 15° from vertical. We also compared radiographs at fixed 0° angle with varying distances from the X-ray source, resulting in a ~1.5x variation in magnification. When we measured fluid level relative to the top of the bulb, and using the 33 cm lever length to normalize for length, we saw minimal effect from angle or magnification (standard deviations were 0.1 and 0.07 mm respectively), Figure. 4.7 and 4.8. However, it was difficult to see the top of the bulb, especially at low angles. We also observed a 0.34 mm systematic difference between angle and position measurements because the origin position (top of the bulb) was judged differently for readings on different days. To account for these differences and improve the measurement facility, we placed two 0.4 mm Ta beads as markers 5 mm apart from each other, next to the fluid channel and at the fluid channel level. As shown in Figure 4.9 and Figure 4.10, we observed minimal

standard deviations of 0.03 mm (corresponds to 3 N) & 0.02 mm (corresponds to 2 N) respectively for fluid level measurements at different magnification and angles. These uncertainties are consistent with other measurements.

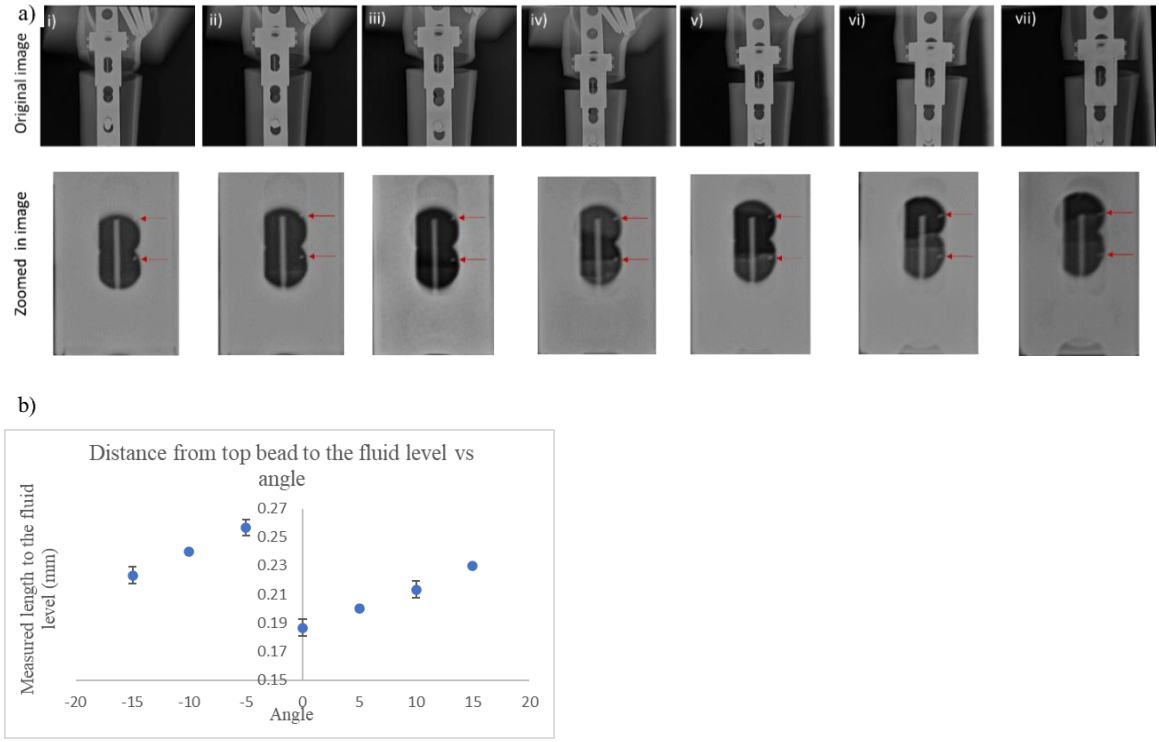

Figure 4.9: Fluid level measured at different angles of fractured Sawbones® tibia (fluidic sensor with embedded Ta bead references). a) Radiographs taken at different X-ray source angles i) through vii) respectively 15°, 10°, 5°, 0°, -5°, -10°, -15°. Red arrows point to the Ta beads. b) Measured fluid level with respect to top bead vs. X-ray source angle. [Reproduced with the permission from **Rajamanthrilage A.C.** et al.: "Measuring Orthopedic Plate Strain to Track Bone Healing Using a Fluidic Sensor Read via Plain Radiography". IEEE Transactions in Biomedical Engineering. (June 2021)].

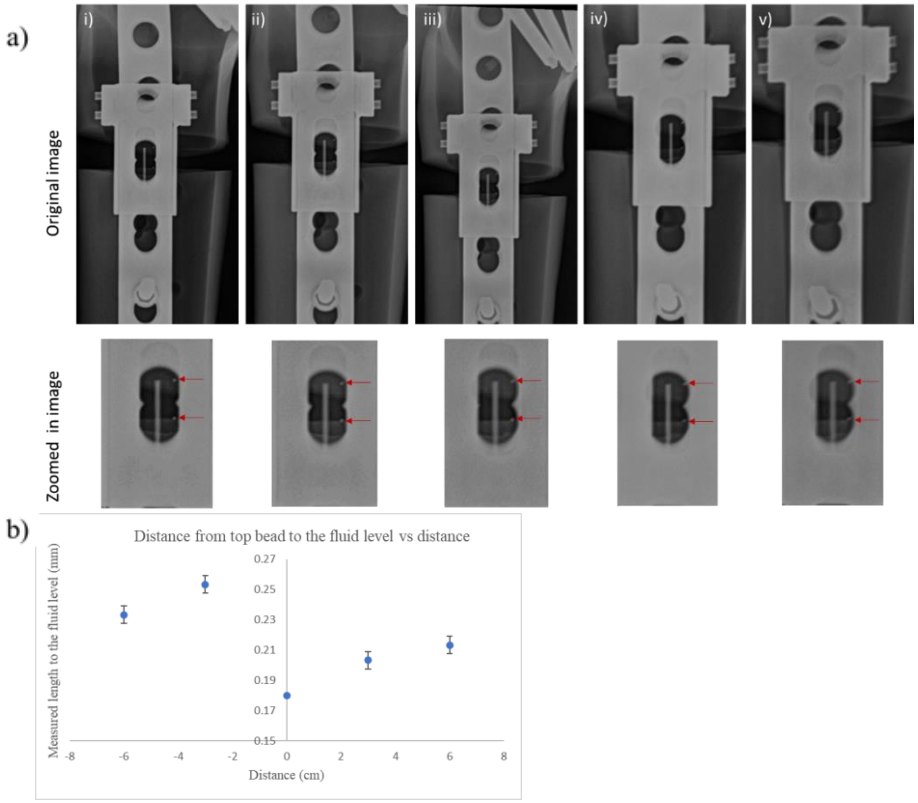

Figure 4.10: Fluid level measured at different positions and effective magnifications of fractured Sawbones® tibia (fluidic sensor with embedded Ta bead references) a) Radiographs of specimen positioned at different distances i) through v) respectively -6, -3, 0, 3, 6 cm. Red arrows show the tantalum beads. b) Measured fluid level vs. position [Reproduced with the permission from **Rajamanthrilage A.C.** et al.: "Measuring Orthopedic Plate Strain to Track Bone Healing Using a Fluidic Sensor Read via Plain Radiography". IEEE Transactions in Biomedical Engineering. (June 2021)].

4.9 Discussion

4.9.1 Sensor range and precision

To be clinically useful, the sensor must be able to track strain from 0 to a maximum of bending under an unstable fracture with 1 body weight (BW), with sufficient precision to identify safe weight bearing. In the cadaver model, our sensor was able to detect displacement over the range of BW with a noise level of 80 μm, 2% of the displacement at 400 N (~½BW for 80 kg patient). This is over an order of magnitude better than measurements taken with standard radiography which has a typical precision of about 2-5 mm on a fracture gap, due to difficulty in identifying edges of the fracture during fracture closing, especially if there is some change in soft tissue and angle.[16,19] Although there is no universally accepted plate strain threshold for safe weight bearing, several lines of reasoning given below suggest it should be roughly around $1/5^{th}$ -$1/10^{th}$ of the initial bending during an unstable fracture, and our observed precision of 2% of the range should thus be adequate for tracking fracture healing, and readily measured the displacement for the 13x stiffer allograft-repaired model.[20,21] More sophisticated estimates may be developed including factors relating to plate construct, healing rate, and expected activity/load, however, 2% precision will likely remain adequate. Indeed, clinically used sensors for tracking stiffness in external fixation devices reportedly have 3% accuracy.[22] In principle, if the range and precision are not adequate, they are adjustable in the design. The range is adjustable by the read capillary length, and the sensitivity is adjustable by controlling the length of the lever arm and ratio of chamber diameter to capillary diameter. For an unstable fracture, we observed that when the inter-fragmentary gap closed by 3 mm,

the plate bending generated 4 mm of fluid displacement, which provides 1.33 of gain in inter-fragmentary motion. As the fracture heals, it would also be possible to use full BW instead of ½ which would double the fluid displacement. Needed range and precision based on clinical studies with external fixation devices

Clinical studies of safe hardware removal for external fixation devices (where stiffness can be directly assessed), have used several different thresholds, although they all fall in the same range. Some clinical studies have used $1/10^{th}$ initial bending as a threshold for device safe removal.[20] Other studies have used tibial stiffness between 8.5 – 20 Nm/°, with 15 Nm/° most common, which is about 25% of the stiffness of intact bone. Indeed, Richardson found that exclusive use of this threshold to decide about when to remove hardware allowed removal of external fixation allowed patients to remove devices 2.3 weeks earlier on average compared to traditional assessment without strain measurements, while longer retention of the fixation in slowly healing patients decreased re-fracture rates from 7% to 0%.[21] The 15 Nm/° threshold would correspond to $1/5^{th}$ of the bending we observe for our unstable plated fracture in Sawbones and cadaveric models. If external fixation hardware can safely be removed when it is carrying $1/5^{th}$ to $1/10^{th}$ of the load applied to the tibia, logically we expect at these thresholds (or perhaps even earlier) it would be safe to bear weight for internally fixed fractures where the hardware is retained.

4.9.1.1 Needed range and precision based on animal and clinical studies with instrumented internal fixation devices

Several animal and human studies have measured strain during healing. In a sheep study with instrumented plates (rosettes of strain gauges) read using percutaneous wires show increase of the total plate surface strain under bending for different gait speeds (2- 5 km/h) found that the strain decreased by a factor of about 7-8 as the fracture heals in the first 6 weeks, and stabilized for the last two weeks.[23] Similarly, in a clinical study of 27 human patients with a titanium femur plate instrumented with a strain gauge and wireless telemetry, Seide and co-workers found a wide range of healing rates (as measured by decrease in relative elasticity), and strong correlations between mechanical and CT analysis of callus healing.[24] Stiffness of 30% corresponded to bridging bone up to the intramedullary canal by CT, and ~10% of initial correlated to bridging throughout the femur by CT. For all these reasons, a stiffness of $1/5^{th}$ to $1/10^{th}$ of initial unstable fixation is likely to be indicative of safe weight bearing, and a noise level of 1-3% of 400 N (½ BW) as observed in our fluidic sensor should be comfortably able to measure this stiffness level.

4.9.1.2 Needed range and precision based on plate fatigue

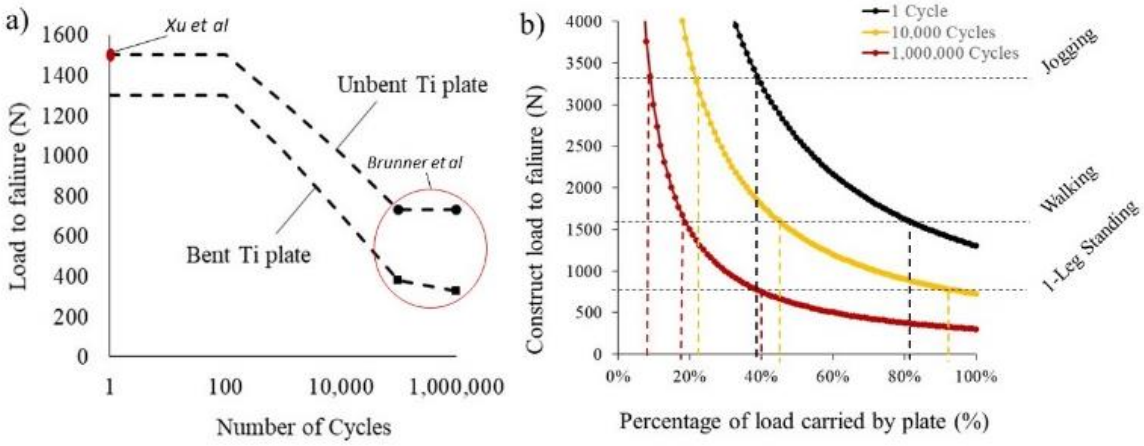

Figure 4.11: Plate load to failure for different activity levels. a) Estimated load (N) to failure vs. number of cycles for bent and unbent plates. b) Construct load to failure (N) and associated activity vs. percentage of load carried by plate assuming bent plate from part(a) and 80 kg patient. [Reproduced with the permission from **Rajamanthrilage A.C.** et al.: "Measuring Orthopedic Plate Strain to Track Bone Healing Using a Fluidic Sensor Read via Plain Radiography". IEEE Transactions in Biomedical Engineering. (June 2021)].

An analysis based on fatigue of plates gives a similar $1/10^{th}$ to $1/5^{th}$ threshold, although it suggests that thresholds could be modified based on activity level, implant fatigue, implant placement, and initial bending. Although no single study presents the entire applied load vs. average or probable cycles to failure, from prior studies at low and high cycle number we can estimate its shape for bent and unbent plates based on three studies.[25–27] Plates are designed to align bone fragments and limit interfragmentary motion,

but allow some bending to encourage callus formation.[28] Tibial plates support short term weight bearing above 1×BW, but will fail under larger loads and eventually fatigue under repetitive cycling of 1×BW. For a single cycle, Lindeque et al. found that proximal locking compression plates (LCP) failed under loads of 1720 N for Synthes plates, and Xu et al. found Zimmer plates and 1500 N for mid-tibial shaft LCP, averaging to around 2x BW for an 80 kg person.[25,26] Additionally, Brunner et al. studied high cycle fatigue failure for normal and bent titanium plates (plate bending is sometimes done deliberately to better fit the bone contour and also can occur naturally during the fixation process). At 10^6 cycles in NaCl solution they report 7 Nm for unbent plates and 3 Nm for plates that were bent prior to fixation.[27] Assuming that the load was axial and that the fracture was treated midshaft where the tibia radius is ~18.2 mm[29], these correspond to 732N, and 323N, respectively. Figure 4.11 (a) plots these values, and further assumes that the curve looks approximately s-shaped with constant failure at low cycle-number (1-100), followed by high cycle fatigue characteristics between 10^3 and 10^6 cycles from Bunner. The ratio of low single cycle yield strength to the endurance limit for high cycles with the unbent plate is ~1.8, and is similar to ASM value of ~1.9.[30] From Brunner's work, the bent plate appears to have ~200 N lower strength at low cycle number, and around twice as much at high cycle number. While these are rough estimates, and more sophisticated studies can be performed for specific plates, amount of pre-bending, and position on the bone, they capture the general characteristics of fatigue.

Using the average load vs. cycles curve Figure 4.11a, we can estimate how much load would be tolerated for a given number of cycles and fraction of load is carried by the

implant (with rest shared by the fracture callus). Figure 4.11b shows this analysis for three loads: 1 cycle, 10,000 cycles (typically accepted as initial postop rehabilitation period[31–33], and 10^6 cycles (close to the endurance limit). A bent plate from figure 4.11a was chosen to be conservative and because plates often bend upon implantation; an analysis based on the unbent curve is shown in Figure 4.11. For single cycles (black curve), orthopedic plates can comfortably support the load from a 80 kg person standing on one leg with a completely unstable fracture (~784 N) but will probably fail during normal walking (2.5-2.8 ×BW) or jogging at 5 mph (4.2×BW).[34] As the fracture callus stiffens, it shares an increasing fraction of the load, and when it carries 50% of the load, peak loads from short term walking would be safe; however, a normally active person takes over 10^6 steps/year, and after 10^6 steps, the load to failure for many plates decreases to about 25% of failure load for a single cycle.[35] For safe weight bearing after 10^6 walking steps one would need the load on the plate to be around $1/5^{th}$ to $1/6^{th}$ of 1 BW, with the callus taking the rest, and $1/8^{th}$ to $1/9^{th}$ for jogging. This line of reasoning suggests that a heavier and more active patient may have a more conservative threshold (or be fitted with a stiffer plate), or that a rapidly healing patient with less fatigue may allow earlier activity.

4.9.2 Comparison to other loaded X-ray techniques

Our sensor design improves upon existing techniques to measure fracture displacement load using X-ray imaging which are either not sufficiently precise or not readily adaptable to clinical application. Although X-ray images can show the hardware and fracture callus, they do not measure the mechanical properties of the fracture.[5,6] With certain fracture types, X-ray images are taken with and without weight-bearing to measure the relative motion of

bones in order to assess fracture stability. However, this procedure has proven insufficiently sensitive, even in cases such as spine fusion, where spinous processes are clearly evident and can move millimeters.[7–9] For example, Song et al. found interobserver variation in measuring spinal process motion to be 1.5 mm (95% confidence interval), an order of magnitude greater than our fluid level precision.[36] Quantitative motion analysis (QMA) software of the intervertebral motion only slightly improves upon manual radiograph analysis.[3] Lower extremity fracture gap movement is even more difficult to access (e.g., ±5 mm for acetabular fractures),[10–12,37] and the fragments move less.

Use of clear markers dramatically improves precision. For example, in radiostereometric analysis (RSA) several tantalum beads are surgically inserted near the fracture site and X-ray images are simultaneous taken at two angles to triangulate the bead position. Precision is typically within ~20-50 μm and bead motion under a load is then used to track fracture stiffness and healing.[38] However, RSA is clinically cumbersome as it needs specialized instruments, increased surgical time/cost to introduce tantalum beads, expertise to perform procedure and analyze results, and the analysis can potentially be confounded by bead placement and migration.[38]

Our hydraulic sensor precision is high compared to direct measurements of fracture gap displacement due to a combination of the hydraulic gain and measuring a clear and unambiguous sensor fluid level. In our experiments, we found average cycle-to-cycle fluid levels variation of 20-70 μm in sawbones, and 80 μm in cadaveric models. This variation could come from a combination of changes in mechanical loading conditions (e.g. settling), and from uncertainty in reading the radiographs (noise). Since the readings do not appear

to systematically drift in time, noise is likely the main source of variation, and assuming the variation is noise sets an upper limit to the noise level. A precision of 80 μm is similar to the 100 μm interobserver variation we found in measuring displacement of radiopaque tungsten wires in a pH sensor based on pH-responsive hydrogels swelling[39]. It is somewhat worse than RSA analysis of tantalum beads (20-50 μm), but an order of magnitude better than direct fracture gap motion analysis with plain film X-rays.

The fluidic sensor can be easily attached to orthopedic plates during surgery, preop (or eventually integrated into plates). Our group previously developed a pin indicator attached to the side of the plate which moving against a scale to provide quantitative readings of plate bending.[17] The gain (pin motion/maximum interfragmentary motion) was approximately the ratio of the pin length to the bone diameter. However, the pin length was 12 cm which was cumbersome. In contrast, the fluidic sensor has hydro-mechanical gain (fluid level displacement/lever displacement during plate bending) almost equal to the fluid reservoir area divided by the capillary channel cross sectional area. In our case, the diameter of the reservoir is 7 mm (area 49 mm^2) and the fluid channel diameter is 0.75 mm (area 0.56 mm^2) providing a gain of somewhat less than 87.5 (less because the lever pushes on the edges of the reservoir less than the center). This gain allowed us to use a much shorter sensor (2.5 cm instead of 12 cm), which gives it a smaller profile, makes it easier to use, and measures bending of the specific section of the implant.

The sensor attaches to the implant using simple screws to grip the side of the plate and could be mounted prior to or after fixing the plate to the bone. In future, simpler attachments could be used, or sensors could be integrated into the plate. A screw attached

to the lever was used to adjust the initial fluid level to account for any plate bending during implantation; in future, longer fluid channels along the side of the plate could be used to increase the maximum sensor range. Overall, the fluid displacements provide straightforward quantitative measurements of the plate strain, thus adding more information to the plain radiographs which are already been used in routine patient workups.

4.9.3 Fluidic length changes at different angles and magnifications

Fluid levels were measured at different angles and magnifications on a fractured *Sawbones*® tibia both relative to the top of the bulb (Figures. 4.7 and 4.8) and, after adding tanatlum bead reference scales, relative to the topmost Ta (Figures4.9, 4.10). Although one would not expect significant differences in angle and magnification from loaded and unloaded X-ray images acquired to measure load sharing, some differences, from session to session may be expected, especially if radiographs are acquired in different locations. While our focus has been on measuring the difference in fluid level before and after applying load, the absolute value may have some relavence for detecting absolute plate bending and subsidence. In principle, variation in leg angle toward/away from the detector could affect apparent abosolute level, partly due to parallax if the liquid level is measured against a scale not in plane, and partly due to changes in magnification with angle. Additionally, variation in magnification could affect measurement if not properly normalized. However, when the fluid level was measured against a scale at the same plane, we found that they were unaffected by angle and magnification, within the measurement

noise level of 0.03 mm (which corresponds to 3 N) & 0.02 mm (2 N), respectively. The tantalum beads scale simplified the measurements and improved consistency.

4.10 Conclusions and future work

While these studies have shown the principle of a fluidic X-VISUAL sensor, much work remains before it can be clinically applied. First, the design size and shape need to be optimized. The thickness of fluidic sensor together with mechanical lever add height over the orthopedic plate which could be inconvenient for the patient. Thus, in future, the fluidic sensor and the mechanical lever may be miniaturized and placed along the side of the plate, where there is more room. Third, we estimated the threshold for safe weight bearing would likely be between $1/5^{th}$ and $1/10^{th}$ initial unstable bending, however, this would need to be verified and patient specific variables may need to be considered. In addition, the sensor was tested only on a tibial plate, and translation to other plates and devices would require site-specific optimization of the sensor size, shape, and gain. Finally, unlike devices using wireless radiotelemetry, our device is read by X-ray imaging, which would permit only periodic measurements during visits to a medical facility where loaded/unloaded radiographs are acquired.

The fluidic sensor enables monitoring orthopedic plate bending directly and quantitatively with higher resolution compared to the common methods available today. Noise levels of 80 μm or less (corresponding ~1 kg of body weight passing through the plate) which is likely sufficient to help physicians quantify the plate bending therefore

callus stiffness during fracture healing. Such information would help physicians determine when the patient is safe to start weight bearing to better communicate rehabilitation protocols with patients and their medical team.

4.11 References

(1) Einhorn, T. A. Enhancement of Fracture-Healing.: *J. Bone Jt. Surg.* **1995**, *77* (6), 940–956. https://doi.org/10.2106/00004623-199506000-00016.

(2) Morshed, S. Current Options for Determining Fracture Union. *Adv. Med.* **2014**, *2014*, 1–12. https://doi.org/10.1155/2014/708574.

(3) Hak, D. J.; Fitzpatrick, D.; Bishop, J. A.; Marsh, J. L.; Tilp, S.; Schnettler, R.; Simpson, H.; Alt, V. Delayed Union and Nonunions: Epidemiology, Clinical Issues, and Financial Aspects. *Injury* **2014**, *45*, S3–S7. https://doi.org/10.1016/j.injury.2014.04.002.

(4) Bishop, J. A.; Palanca, A. A.; Bellino, M. J.; Lowenberg, D. W. Assessment of Compromised Fracture Healing. *JAAOS-J. Am. Acad. Orthop. Surg.* **2012**, *20* (5), 273–282.

(5) Buza III, J. A.; Einhorn, T. Bone Healing in 2016. *Clin. Cases Miner. Bone Metab.* **2016**, *13* (2), 101.

(6) Papakostidis, C.; Kanakaris, N. K.; Pretel, J.; Faour, O.; Morell, D. J.; Giannoudis, P. V. Prevalence of Complications of Open Tibial Shaft Fractures Stratified as per the Gustilo-Anderson Classification. *Injury* **2011**, *42* (12), 1408–1415. https://doi.org/10.1016/j.injury.2011.10.015.

(7) Mody, R. M.; Zapor, M.; Hartzell, J. D.; Robben, P. M.; Waterman, P.; Wood-Morris, R.; Trotta, R.; Andersen, R. C.; Wortmann, G. Infectious Complications of Damage Control Orthopedics in War Trauma. *J. Trauma* **2009**, *67* (4), 758–761. https://doi.org/10.1097/TA.0b013e3181af6aa6.

(8) Schmidt, A. H.; Finkemeier, C. G.; Tornetta, P. Treatment of Closed Tibial Fractures. *J. Bone Jt. Surg.-Am. Vol.* **2003**, *85* (2), 352–368. https://doi.org/10.2106/00004623-200302000-00027.

(9) Cipriano, C. A.; Issack, P. S.; Shindle, L.; Werner, C. M. L.; Helfet, D. L.; Lane, J. M. Recent Advances Toward the Clinical Application of PTH (1-34) in Fracture Healing. *HSS J.* **2009**, *5* (2), 149–153. https://doi.org/10.1007/s11420-009-9109-8.

(10) Biomechanics Laboratory, Department of Orthopaedic Surgery; Chao, E.; Inoue, N. Biophysical Stimulation of Bone Fracture Repair, Regeneration and Remodelling. *Eur. Cell. Mater.* **2003**, *6*, 72–85. https://doi.org/10.22203/eCM.v006a07.

(11) Kuzyk, P. R.; Schemitsch, E. H. The Science of Electrical Stimulation Therapy for Fracture Healing. *Indian J. Orthop.* **2009**, *43* (2), 127.

(12) Griffin, X. L.; Parsons, N.; Costa, M. L.; Metcalfe, D. Ultrasound and Shockwave Therapy for Acute Fractures in Adults. *Cochrane Database Syst. Rev.* **2014**. https://doi.org/10.1002/14651858.CD008579.pub3.

(13) Hammer, R. R.; Hammerby, S.; Lindholm, B. Accuracy of Radiologic Assessment of Tibial Shaft Fracture Union in Humans. *Clin. Orthop.* **1985**, No. 199, 233–238.

(14) Panjabi, M. M.; Lindsey, R. W.; Walter, S. D. The Clinician's Ability to Evaluate the Strength of Healing Fractures from Plain Radiographs. *J. Orthop. Trauma* **1989**, *3* (1), 29–32.

(15) Richardson, J. B.; Kenwright, J.; Cunningham, J. L. Fracture Stiffness Measurement in the Assessment and Management of Tibial Fractures. *Clin. Biomech.* **1992**, *7* (2), 75–79. https://doi.org/10.1016/0268-0033(92)90018-Y.

(16) Blokhuis, T. J.; de Bruine, J. H. D.; Bramer, J. A. M.; den Boer, F. C.; Bakker, F. C.; Patka, P.; Haarman, H. J. Th. M.; Manoliu, R. A. The Reliability of Plain Radiography in Experimental Fracture Healing. *Skeletal Radiol.* **2001**, *30* (3), 151–156. https://doi.org/10.1007/s002560000317.

(17) Pelham, H.; Benza, D.; Millhouse, P. W.; Carrington, N.; Arifuzzaman, M.; Behrend, C. J.; Anker, J. N.; DesJardins, J. D. Implantable Strain Sensor to Monitor Fracture Healing with Standard Radiography. *Sci. Rep.* **2017**, *7* (1), 1489. https://doi.org/10.1038/s41598-017-01009-7.

(18) Melnikov, P.; Zanoni, L. Z. Clinical Effects of Cesium Intake. *Biol. Trace Elem. Res.* **2010**, *135* (1–3), 1–9. https://doi.org/10.1007/s12011-009-8486-7.

(19) Corrales, L. A.; Morshed, S.; Bhandari, M.; Miclau, T. Variability in the Assessment of Fracture-Healing in Orthopaedic Trauma Studies: *J. Bone Jt. Surg.-Am. Vol.* **2008**, *90* (9), 1862–1868. https://doi.org/10.2106/JBJS.G.01580.

(20) Claes, L.; Grass, R.; Schmickal, T.; Kisse, B.; Eggers, C.; Gerngro, H.; Mutschler, W.; Arand, M.; Wintermeyer, T.; Wentzensen, A. Monitoring and Healing Analysis

of 100 Tibial Shaft Fractures. *Langenbecks Arch. Surg.* **2002**, *387* (3–4), 146–152. https://doi.org/10.1007/s00423-002-0306-x.

(21) Richardson, J. B.; Cunningham, J. L.; Goodship, A. E.; O'connor, B. T.; Kenwright, J. Measuring Stiffness Can Define Healing of Tibial Fractures. *J. Bone Joint Surg. Br.* **1994**, *76* (3), 389–394.

(22) Wade, R.; Richardson, J. Outcome in Fracture Healing: A Review. *Injury* **2001**, *32* (2), 109–114. https://doi.org/10.1016/S0020-1383(00)00126-1.

(23) Stoffel, K.; Klaue, K.; Perren, S. M. Functional Load of Plates in Fracture Fixation in Vivo and Its Correlate in Bone Healing. *Injury* **2000**, *31*, 37–86. https://doi.org/10.1016/S0020-1383(00)80042-X.

(24) Seide, K.; Aljudaibi, M.; Weinrich, N.; Kowald, B.; Jürgens, C.; Müller, J.; Faschingbauer, M. Telemetric Assessment of Bone Healing with an Instrumented Internal Fixator: A Preliminary Study. *J. Bone Joint Surg. Br.* **2012**, *94-B* (3), 398–404. https://doi.org/10.1302/0301-620X.94B3.27550.

(25) Xu, G.; Liu, B.; Zhang, Q.; Wang, J.; Chen, W.; Liu, Y.; Peng, A.; Zhang, Y. Biomechanical Comparison of Gourd-Shaped LCP versus LCP for Fixation of Comminuted Tibial Shaft Fracture. *J. Huazhong Univ. Sci. Technolog. Med. Sci.* **2013**, *33* (2), 250–257. https://doi.org/10.1007/s11596-013-1106-y.

(26) Lindeque, B.; Baldini, T. A Biomechanical Comparison of Three Different Lateral Tibia Locking Plates. *Orthopedics* **2010**, *33* (1), 18–21. https://doi.org/10.3928/01477447-20091124-25.

(27) Brunner, H.; Simpson, J. P. Fatigue Fracture of Bone Plates. *Injury* **1980**, *11* (3), 203–207. https://doi.org/10.1016/S0020-1383(80)80044-1.

(28) Ehlinger, M.; Rahme, M.; Moor, B.-K.; Di Marco, A.; Brinkert, D.; Adam, P.; Bonnomet, F. Reliability of Locked Plating in Tibial Plateau Fractures with a Medial Component. *Orthop. Traumatol. Surg. Res.* **2012**, *98* (2), 173–179. https://doi.org/10.1016/j.otsr.2011.10.009.

(29) Bokariya, P.; Sontakke, B.; Waghmare, J.; Tarnekar, A.; Tirpude, B.; Shende, M. The Anthropometric Measurements of Tibia. **2012**, *34* (4), 3.

(30) *ASM Aerospace Specification Metals Inc.* ASM Aerospace Specification Metals Inc. http://asm.matweb.com/search/SpecificMaterial.asp?bassnum=MTP641 (accessed 2020-07-26).

(31) Rupprecht, M.; Grossterlinden, L.; Ruecker, A. H.; De Oliveira, A. N.; Sellenschloh, K.; Nüchtern, J.; Püschel, K.; Morlock, M.; Rueger, J. M.; Lehmann, W. A Comparative Biomechanical Analysis of Fixation Devices for Unstable Femoral Neck Fractures: The Intertan versus Cannulated Screws or a Dynamic Hip Screw. *J. Trauma - Inj. Infect. Crit. Care* **2011**, *71* (3), 625–634. https://doi.org/10.1097/TA.0b013e31820e86e6.

(32) Kubiak, E. N.; Bong, M.; Park, S. S.; Kummer, F.; Egol, K.; Koval, K. J. Intramedullary Fixation of Unstable Intertrochanteric Hip Fractures: One or Two Lag Screws. *J. Orthop. Trauma* **2004**, *18* (1), 12–17. https://doi.org/10.1097/00005131-200401000-00003.

(33) Springer, E. R.; Lachiewicz, P. F.; Gilbert, J. A. Internal Fixation of Femoral Neck Fractures. A Comparative Biomechanical Study of Knowles Pins and 6.5-Mm Cancellous Screws. *Clin. Orthop.* **1991**.

(34) D'Lima, D. D.; Fregly, B. J.; Colwell, C. W. Implantable Sensor Technology: Measuring Bone and Joint Biomechanics of Daily Life in Vivo. *Arthritis Res. Ther.* **2013**, *15* (1), 203. https://doi.org/10.1186/ar4138.

(35) Naderi, M.; Hoseini, S. H.; Khonsari, M. M. Probabilistic Simulation of Fatigue Damage and Life Scatter of Metallic Components. *Int. J. Plast.* **2013**, *43*, 101–115. https://doi.org/10.1016/j.ijplas.2012.11.001.

(36) Song, K.-S.; Piyaskulkaew, C.; Chuntarapas, T.; Buchowski, J. M.; Kim, H. J.; Park, M. S.; Kang, H.; Riew, K. D. Dynamic Radiographic Criteria for Detecting Pseudarthrosis Following Anterior Cervical Arthrodesis: *J. Bone Jt. Surg.-Am. Vol.* **2014**, *96* (7), 557–563. https://doi.org/10.2106/JBJS.M.00167.

(37) Agarwal, A. Principles of Nonunions. In *Nonunions*; Springer, Boston, MA, 2018; pp 1–43. https://doi.org/10.1007/978-1-4939-7178-7_1.

(38) Augat, P.; Simon, U.; Liedert, A.; Claes, L. Mechanics and Mechano-Biology of Fracture Healing in Normal and Osteoporotic Bone. *Osteoporos. Int.* **2005**, *16* (S02), S36–S43. https://doi.org/10.1007/s00198-004-1728-9.

(39) Arifuzzaman, Md.; Millhouse, P. W.; Raval, Y.; Pace, T. B.; Behrend, C. J.; Beladi Behbahani, S.; DesJardins, J. D.; Tzeng, T.-R. J.; Anker, J. N. An Implanted PH Sensor Read Using Radiography. *The Analyst* **2019**. https://doi.org/10.1039/C8AN02337A.

CHAPTER 5

CONCLUSIONS AND FUTURE WORK

The studies in this dissertation addressed two significant concerns in fracture healing: monitoring implanted medical device-associated infections and measuring fracture stiffness to avoid early weight-bearing or related complications.[1] Both implantable sensors use X-rays for signal detection as well as can reveal important information regarding fracture healing and orthopedic implant associated infections. I will discuss these two topics sequentially in 5.1 and 5.2 respectively.

5.1 X-ray interrogated implantable biochemical sensor for monitoring implant associated infections

A novel intramedullary rod pH sensor was developed to map the pH inside the medullary cavity of a rabbit tibia via XELCI imaging. We observed pH changes during implant associated infection through both bone and tissue (~1 -1.5 cm of thickness). Our group has previously used XELCI for imaging the implant associated infections on the bone surface, but this dissertation introduces imaging through the bone with the sensor in the medullary cavity. This will allow us to investigate the local environment of the sensor inside the medullary cavity during an infection via XELCI. The XELCI imaging system provides implant surface-specific chemical information with high spatial resolution imaging.[2–4] With the acquired spatial resolution of the XELCI system, we will be able to

image heterogenic pH microenvironment inside the bone cavity. Furthermore, it will allow us to monitor pH changes associated with normal healing curve vs the local environment of the implant surface after antibiotic treatments or after the eradication treatments. None of the currently available methods can provide high resolution pH imaging in situ.

The sensor provides chemical specificity from the optical indicator dyes with the implant specificity from the coating. As the imaging technique uses X-ray as an excitation source, it provides a unique, low background and higher resolution for imaging through thick tissue. The intramedullary rod pH sensor consists of a pH-sensitive optical dye incorporated acrylamide polymer film coated over Gd_2O_2S: Eu scintillator layer (prominent emissions at ~620 nm and ~700 nm). The Bromothymol blue indicator dye has absorbance which overlaps with the emission of the scintillator particles, mostly at ~620 nm. As we monitor the variation of total transmitted light at 620 nm, the 700 nm light which is having a smaller change in the absorbance with respect to pH will act as a spectral reference. Considering the ratio between 620 nm and 700 nm light will accounts for the variation in intensity at either wavelength due to changes in scintillator concentration, X-ray power and attenuation in tissue and optical collection efficiency. As 700 nm light can pass higher penetration depths through tissue (at 700 nm tissue has lower effective attenuation coefficients), compared to 600 nm light, we always accompany a reference region with no pH sensitive dye film to account for spectral distortion assuming tissue above the reference region causes a similar degree of spectral distortion. The sensors were characterized in vitro before carrying out the in vivo animal experiments for pH changes and signal detection. A preliminary study was carried out with a reamed rabbit cadaveric

tibia using an intramedullary rod sensor with two distinct pH regions (acidic and basic pHs). As expected, we were able to observe clearly distinct pH regions once imaged with XELCI. It confirmed the ability of the XELCI imaging system to be used in vitro pH imaging through tissue.

The pre-pilot rabbit study was carried out with the conformally coated stainless steel rod sensor using three rabbit models (two infected models and one control animal). One of the infected models were implanted with pre-biofilm grown rod sensor while the other model was inoculated at the time of surgery after inserting the rod sensor. Both exhibited decrease in pH during the 10-11 days of imaging; by contrast the control rabbit showed no change in the pH until euthanasia. The postmortem studies showed well-established infection at the tibia of both infected rabbits but not the control. It confirmed the bacterial concentration we inoculated was able to establish an infection in the intramedullary cavity and the acidic environment can be imaged/map with the coated rod sensor. Moreover, it showed that during a normal healing curve the pH of the intramedullary cavity local environment stayed constant. As this study was carried out to test the surgery procedures, imaging protocols and sensor behaviors prior to a full-scale study, we could conclude that our test methods are working accordingly, and we can image/map the intramedullary rod associated pH changes with high spatial resolution.

The intramedullary rod design was modified for the second pre-pilot studies to accompany the pH-sensitive gel films. The modified version will allow us to investigate different hypotheses compared to the previous studies carried out in our lab. Implant plates with layered sensor films were studied for monitoring implant associated infections on the

bone surface. With this modified rod sensor, we will be able to study a more enclosed, different environment. Also, the sensor can be compared to the intramedullary rod sensor with thinner pH sensitive films vs the thicker film. The second pre-pilot rabbit studies to investigate the pH variations in bone cavity was carried out by using three rabbit models. The same procedure was followed as mentioned in the Chapter 3 of this dissertation other than the design of the pointed intramedullary rod sensor with the pH sensitive gel layer over a scintillator layer and pH variation was studied. One of the sensors (neutral) was inserted to reamed tibia of the control animal with sterile saline. The XELCI imaging was carried out for 10 days until euthanasia, and a postmortem image was also taken after sensor extraction. As shown in the analyzed ratio images of the sensor, a significant change in the pH is not observed. Also, for Day 0, 1 and 3 images, the intensities were very low to identify the regions of the sensor to determine pH variation. This majorly depends on how the animal was positioned under the detector as wells as the sensor placement inside the tibia during the surgery. As the images suggest, the light is only coming from one angle and sensor is not facing the detector. But the pre-surgery and postmortem imaging suggest that the sensor was remaining neutral during the whole imaging period.

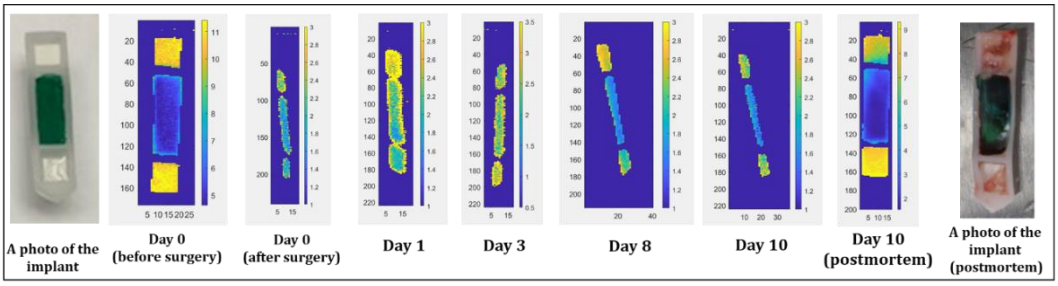

Figure 5.1: Control rabbit (Rabbit 4). XELCI ratio images of the rod sensor during the imaging days.

For the first infected model, the sensor was inserted into the tibial intramedullary cavity and injected a bacterial inoculum at the surgery. The imaging on the sensor was carried out for 10 days. The ratio images of the sensor are shown in the figure below. The sensor started as a neutral sensor from Day 0 and continued to stay neutral since Day 10. Although we expect the pH to drop and see signs of infection, the tibial cavity remains uninfected during this study. It can be due to the flush out of bacterial load with blood while reaming the tibia at the surgery.

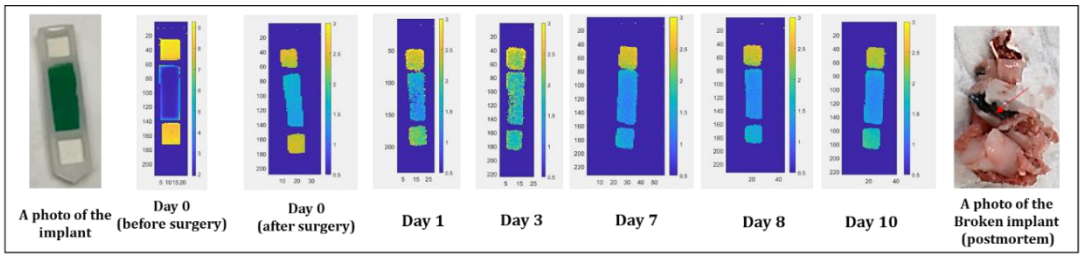

Figure 5.2: Infected rabbit-I (Rabbit 6). XELCI Ratio images of the rod sensor during the imaging days. (Red arrow is pointed to the broken gel layer extracted with the sensor)

The second infected model was created using the biofilm grown sensor. As shown in the figure below, the sensor implanted with acidic color at the start. Also, the ratio image shows the acidic nature of the sensor in XELCI imaging. The ratio images in Day 1, 3, 7 do not show sufficient intensity to conclude about the infection. But the postmortem observation also shows no signs of infection inside the tibial cavity or top of the tibia (the spot where reaming the tibia has begun). Also, the postmortem XELCI imaging shows the sensor has neutralized.

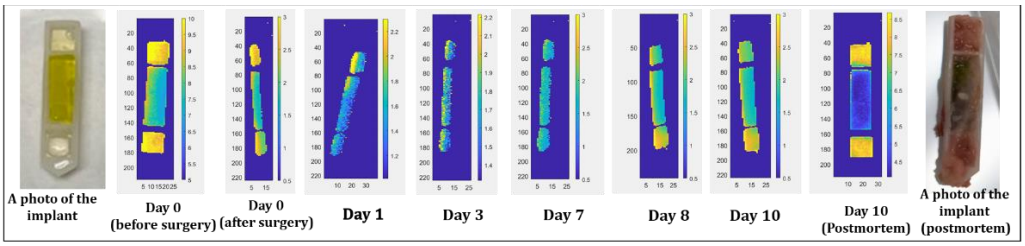

Figure 5.3: Infected rabbit II (Rabbit 7). XELCI Ratio images of the rod sensor during the imaging days.

Therefore, these studies in the future can be carried out with modifications to the method. We should pay attention to the position we implant the sensor at the surgery because it can essentially hinder the light intensity produced by the scintillator films. If the sensor is not properly placed inside the bone cavity, the sensor angle can block the luminescence light reaching the detector as this is a flat sensor compared to the other

intramedullary rod sensor which is cylindrical. As previously mentioned, the advantage of this sensor modification is the presence of two reference regions in both sides to account for the difference in light intensities due to the tissue thickness.

In the future the thickness of the pH sensitive hydrogel layer can be reduced to improve the sensitivity of the pH detection. If the thickness of the gel is reduced, we can detect minute changes in the pH. As a thinner gel layer allow faster detection rates than the thicker films, we can detect the pH changes more efficiently. The decrease in absorbance due to reducing the thickness can be addressed by increasing the dye concentration. Also, the pH sensitive dye can be bound to the gel covalently to minimize the leaching. Currently the two layers of Gd_2O_2S:Eu incorporated PDMS and polymer hydrogel are placed on top of each other in the chambers of the implants. To provide more mechanical stability to the sensor layers, the PDMS layer can be chemically bound to the pH sensitive hydrogel layer.

The Chromoionophore III films were also investigated as a possible pH sensitive dye for making thinner coatings on the implants. As Chromionophore III has a pH dependent absorbance which overlaps with the emission of the Gd_2O_2S: Eu scintillator particles it can be used for monitoring implant associated infections with XELCI.

A second motivation for using Chromionophore III is that researchers use it in conjunction with ionophores in a hydrophobic matrix to detect specific ions as described in optode literature.[5–7] For example, complexation between a cation and ionophore would cause release of H^+ from the Chromionophore III to maintain charge neutrality of the film causing a color change. Here we investigated the pH dependence of a Chromionophore III film both as a simple way to coat a thin pH-sensitive film on an implant and as a way to

facilitate future research on ions near during bone healing and infection, including nitrite, calcium ions, and others.[8]

Table 5.1 shows the composition of the cocktail mixture used to prepare the film. The reagents were mixed in a scintillator vial (Figure 5.4). pH-responsive films were prepared by drop coating the cocktail onto a filter paper substrate (VWR Filter paper qualitative, 413); similarly, cut-glass slides were dipped coated with Chromoionophore III mixture. Extinction for the films different pHs were recorded using aqueous buffers from pH 4 to 7.5 (Figure 5.5). In our experiments to generate a calibration curve for the sensor, we observed an effective pK_a value of ~6 for a dip coated thin film in equilibrium with the aqeous buffer solutions. While this is somewhat lower than reported values, the literature shows that the pK_a for Chromionophore III depneds very strongly on its host matrix environment (this is generally true of most dyes, but especially when they are placed in hydrophobic matricies). This variation may also be due to the variation impurities present in the samples and the ion concentrations in the buffers we used for the experiment. Although Chromionophore III was reported to have a pK_a of 13.4 by estimating based on the potentiometric measurements with cation-membranes in [DOS-PVC (2:1)] matrix ,[9] Linder et al found that a consistent few percent of a hydrophilic impurity in the commercial Fluka product which dramatically altered its behavior.[10] Eric Bakker's group has also done extensive studies, and found the pK_a was 8.0 in PVC/DOS and 9.6 in PVC-NPOE and this agreed with potentiometric titrations[11]; in nanospheres formed with a combination of DOS/F127 pluronics gel, they found a stretched curve indicating a range of pK_a values with an average effective value of 9.2.[12] Our effective pK_a of 6 and range of ~5-7 has some

advantages for looking at low pH, or for looking at cations in neutral or physiological pH after adding ionophores.

Table 5.1: The composition for the Chromoionophore III films

Chemical substance	Amount
Chromoionophore III	3 mg
PVC (Poly vinyl Chloride)	~31.9 mg
DOS (Bis(2 ethyl hexyl) sebacate)	~65.2 mg
THF (Tetra Hydro Furan)	1.5 ml

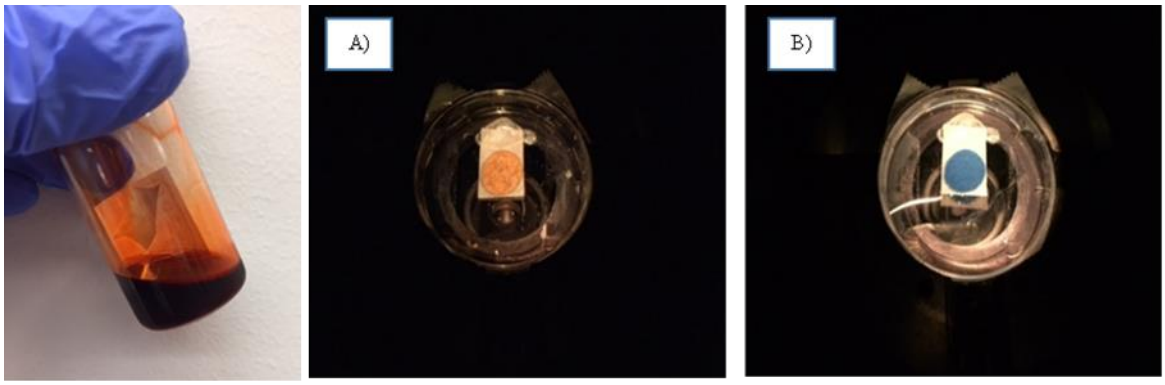

Figure 5.4: Photos of chromoionophore mixture and drop coated on filter paper. A) Red colored sensor in acidic solution. B) Blue colored sensor in basic solution.

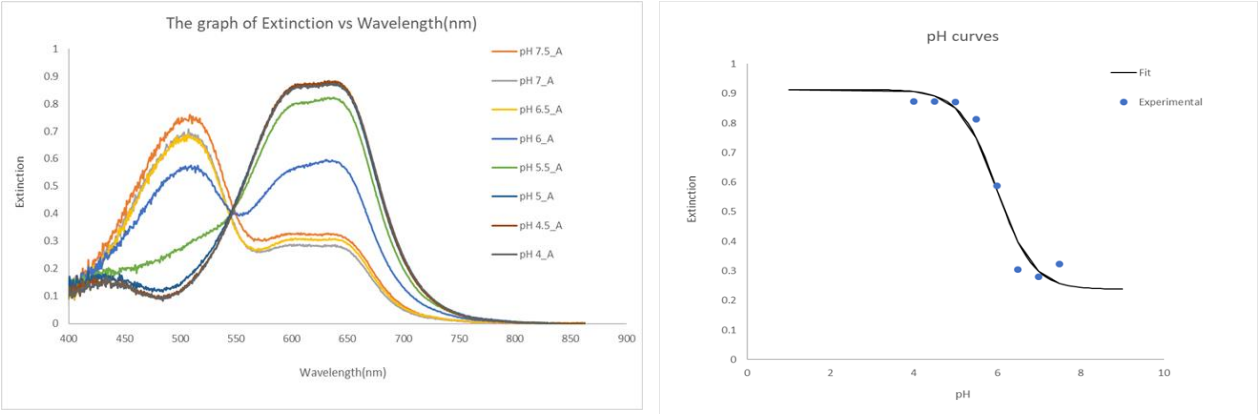

Figure 5.5: The extinction spectra and pH curves. A) The extinction spectra for Chromoionophore film coated filter paper in different pHs. B) The pH response curve and least squares fit to simulated protonated and deprotonated indicator dye concentration assuming two state system (acid and base) with species distributed according to Henderson-Hasselbalch equation.

Importantly, our design with filter paper was a highly flexible and robust substrate which showed negligible leaching in solution, and rapid response (within 10-15min). These are useful features for XELCI and may also have applications in simple paper-based sensors. But Chromoionophore dye would be a better approach for monitoring pH and other analytes once the pK_a could be altered. It will also allow us to dip coat thinner pH sensitive films.

5.2 X-ray interrogated implantable biomechanical sensor for monitoring fracture healing

Because of orthopedic implant associated infections, fractured bones will not heal normally resulting in construct fatigue and failure eventually. Moreover, there are several other reasons contributing to slow healing or no healing including early weight bearing. In Chapter 4, we introduced a hydromechanical sensor to measure fracture healing read via plain radiography (X-VISUAL sensor) and inform the patient of any adjunctive therapies are needed or if it's safe to bear weight.

The X-VISUAL fluidic sensor can be introduced as a promising way of monitoring the stiffness of fractured healing bone. It can be read by plain radiography compared to other wireless radiotelemetry during periodic visits to medical facility where loaded/unloaded radiographs are acquired. But there can be several modifications that can be done before it can be applied clinically. The major problem will be the dimensions of the sensor. The current design of the sensor adds more than 5 mm of height above the orthopedic plate, which will be uncomfortable for the patient. In future studies, the fluidic sensor and the mechanical lever should be miniaturized. At least, the thickness could be reduced by half to add only 2.5 mm over the implant plate. Alternatively, the sensor can also be designed to attach from the side of the plate. Moreover, the sensor can be tested on other types of orthopedic plates. It might require site-specific optimization of the sensor size, shape and gain.

All in all, this dissertation mainly discusses X-ray interrogated biochemical sensor and a biomechanical sensor for monitoring implant associated infections and stiffness during fracture healing. The fluidic sensor demonstrated stiffness dependent amplified signal (fluid levels) while experimenting with cyclic loading on fractured tibia mimic and human cadaveric models. The miniaturized sensor allowed us to monitor the fracture healing process non-invasively via plain radiography. With the biochemical sensor, we were able to successfully image/map pH variations associated with implant infection in the pre-pilot rabbit study. The modified XELCI imaging system allowed detection of the pH dependent luminescent signal through both bone and tissue for the first time. Thus, we demonstrated new types and uses of X-ray based imaging to elucidate biochemical and biomechanical processes during fracture healing and infection.

5.3 References

(1) Rajamanthrilage, A.; Arifuzzaman, Md.; Millhouse, P.; Pace, T.; Behrend, C.; DesJardins, J.; Anker, J. Measuring Orthopedic Plate Strain to Track Bone Healing Using a Fluidic Sensor Read via Plain Radiography. *IEEE Trans. Biomed. Eng.* **2022**, *69* (1), 278–285. https://doi.org/10.1109/TBME.2021.3092291.

(2) Wang, F.; Raval, Y.; Tzeng, T. J.; Anker, J. N. X-Ray Excited Luminescence Chemical Imaging of Bacterial Growth on Surfaces Implanted in Tissue. *Adv. Healthc. Mater.* **2015**, *4* (6), 903–910.

(3) Uzair, U.; Benza, D.; Behrend, C. J.; Anker, J. N. Noninvasively Imaging PH at the Surface of Implanted Orthopedic Devices with X-Ray Excited Luminescence Chemical Imaging. *ACS Sens.* **2019**, *4* (9), 2367–2374. https://doi.org/10.1021/acssensors.9b00962.

(4) Uzair, U.; Johnson, C.; Beladi-Behbahani, S.; Rajamanthrilage, A. C.; Raval, Y. S.; Benza, D.; Ranasinghe, M.; Schober, G.; Tzeng, T.-R. J.; Anker, J. N. Conformal Coating of Orthopedic Plates with X-Ray Scintillators and PH Indicators for X-Ray Excited Luminescence Chemical Imaging through Tissue. *ACS Appl. Mater. Interfaces* **2020**, *12* (47), 52343–52353. https://doi.org/10.1021/acsami.0c13707.

(5) Dubach, J. M.; Lim, E.; Zhang, N.; Francis, K. P.; Clark, H. In Vivo Sodium Concentration Continuously Monitored with Fluorescent Sensors. *Integr. Biol.* **2011**, *3* (2), 142–148.

(6) Mistlberger, G.; Crespo, G. A.; Bakker, E. Ionophore-Based Optical Sensors. *Annu. Rev. Anal. Chem.* **2014**, *7* (1), 483–512. https://doi.org/10.1146/annurev-anchem-071213-020307.

(7) Tsagkatakis, I.; Peper, S.; Bakker, E. Spatial and Spectral Imaging of Single Micrometer-Sized Solvent Cast Fluorescent Plasticized Poly(Vinyl Chloride) Sensing Particles. *Anal. Chem.* **2001**, *73* (2), 315–320. https://doi.org/10.1021/ac000832f.

(8) Bühlmann, P.; Pretsch, E.; Bakker, E. Carrier-Based Ion-Selective Electrodes and Bulk Optodes. 2. Ionophores for Potentiometric and Optical Sensors. *Chem. Rev.* **1998**, *98* (4), 1593–1688. https://doi.org/10.1021/cr970113+.

(9) Bakker, E.; Lerchi, M.; Rosatzin, T.; Rusterholz, B.; Simon, W. Synthesis and Characterization of Neutral Hydrogen Ion-Selective Chromoionophores for Use in Bulk Optodes. *Anal. Chim. Acta* **1993**, *278* (2), 211–225. https://doi.org/10.1016/0003-2670(93)85102-P.

(10) Lindner, E.; Rosatzin, T.; Jeney, J.; Cosofret, V. V.; Simon, W.; Buck, R. P. The Potentiometric PH Response of Chromoionophores Used in Optical Sensors. *J. Electroanal. Chem.* **1993**, *352* (1–2), 309–312.

(11) Qin, Y.; Bakker, E. Quantitive Binding Constants of H+-Selective Chromoionophores and Anion Ionophores in Solvent Polymeric Sensing Membranes. *Talanta* **2002**, *58* (5), 909–918.

(12) Xie, X.; Zhai, J.; Jarolímová, Z.; Bakker, E. Determination of p K_a Values of Hydrophobic Colorimetric PH Sensitive Probes in Nanospheres. *Anal. Chem.* **2016**, *88* (6), 3015–3018. https://doi.org/10.1021/acs.analchem.5b04671.

Appendix A

Matlab code for XELCI data analysis

```
function [I6t,I7t,R,Pixeldwelltime, I6, I7] = motimit2(allmotorpositions,rawintensity1,
rawintensity2, stepsize,alltimings,bg6,bg7,thr6,thr7)
%This script ...  still to do: get histogram of I6 and I7 and pick
%bg&threhold based on low end of histogram.
%A check of whether the script is working properly is to compare
%sum(rawI1) to sum(I7) for each row, if the signal is allocated properly,
%the sums should be identical (except for signal collected after motor moves to end).

rawintensity2=rawintensity2-rawintensity1;  %I6 = Itotal - I7. Previous code had I6 and
I7 acquired separately.

if nargin<4,
   stepsize=0.5;
end;
[Max, Ind]= max(allmotorpositions'); %Max(k) is the maximum value of row k; Ind(k) is
the column this maximum value is found.
Cols=ceil(Max(1)/stepsize); %number of columns (pixels) in each row = max motor
position/stepsize. Assuming min motorposition = 0.
Rows=size(Max,2); %number of rows (pixels) in the final image
I6=zeros([Rows Cols]); %Initialize image at 600nm
I7=zeros([Rows Cols]); %Initialize image at 700nm
Pixeldwelltime=zeros([Rows Cols]); %Initialize dwell time array

for k=1:Rows, %
   j=1;
   for i=1:Ind(k),
      if rawintensity1(k,i)>1000000 || rawintensity2(k,i)>1000000
         display('unexpectedly high signal rawintensity'); display(rawintensity1(k,i));
display(rawintensity2(k,i)); display([k i j]);
         rawintensity1(k,i)=0; rawintensity2(k,i)=0; alltimings(k,i)=0;
      end;

      if allmotorpositions(k,i)<=j*stepsize, %motor position still within pixel, alot signal
to that pixel
         I7(k,j)=I7(k,j)+rawintensity1(k,i);
         I6(k,j)=I6(k,j)+rawintensity2(k,i);
         Pixeldwelltime(k,j)=Pixeldwelltime(k,j)+alltimings(k,i);
      elseif allmotorpositions(k,i)>j*stepsize, %moved past the end of pixel
```

```
        if i==1,      %beginning of row
           j=ceil(allmotorpositions(k,i)/stepsize);
           I7(k,j)=rawintensity1(k,i);
           I6(k,j)=rawintensity2(k,i);
           Pixeldwelltime(k,j)=alltimings(k,i);

           %display(I6(k,j));
           %display([k j i]);
        else         %moved past end of pixel, not the beginning of row
          dtrav=allmotorpositions(k,i)-allmotorpositions(k,i-1);
          if allmotorpositions(k,i)<=(j+1)*stepsize,   %moved past the end of first pixel
but not past end of second: alot signal to the first and second pixel in proportion to
distance travelled
              I7(k,j)=I7(k,j)+rawintensity1(k,i)*(j*stepsize-allmotorpositions(k,i-1))/dtrav;
              I7(k,j+1)=rawintensity1(k,i)*(allmotorpositions(k,i)-j*stepsize)/dtrav;
              I6(k,j)=I6(k,j)+rawintensity2(k,i)*(j*stepsize-allmotorpositions(k,i-1))/dtrav;
              I6(k,j+1)=rawintensity2(k,i)*(allmotorpositions(k,i)-j*stepsize)/dtrav;
              Pixeldwelltime(k,j)=Pixeldwelltime(k,j) + alltimings(k,i)*(j*stepsize-
allmotorpositions(k,i-1))/dtrav;
              Pixeldwelltime(k,j+1)=alltimings(k,i)*(allmotorpositions(k,i)-
j*stepsize)/dtrav;

              j=j+1;

          else   %moved past the end of first and second pixel, i.e. alot signal to more than
two pixels
              display('large distance travelled compared to pixel size... interpolating');
              display([k i j]);

              I7(k,j)=I7(k,j)+rawintensity1(k,i)*(j*stepsize-allmotorpositions(k,i-1))/dtrav;
%alot signal to end of first pixel in proportion to distance travelled
              I6(k,j)=I6(k,j)+rawintensity2(k,i)*(j*stepsize-allmotorpositions(k,i-1))/dtrav;
              Pixeldwelltime(k,j)=Pixeldwelltime(k,j)+alltimings(k,i)*(j*stepsize-
allmotorpositions(k,i-1))/dtrav;
              dtravrem=allmotorpositions(k,i)-j*stepsize;  %distance travelled past end of
pixel
              stepsleft=dtravrem/stepsize; %steps past end of first pixel
              I6rem=rawintensity2(k,i)*dtravrem/dtrav; %signal remaining to alot
              I7rem=rawintensity1(k,i)*dtravrem/dtrav;
              Pixeldwellrem=alltimings(k,i)*dtravrem/dtrav;
                for l=1:floor(stepsleft),
                   I6(k,j+l)=I6rem/stepsleft;
                   I7(k,j+l)=I7rem/stepsleft;
                   Pixeldwelltime(k,j+l)=Pixeldwellrem/stepsleft;
```

```
                end;
            j=j+l;
            I6remlastpx=I6rem*(stepsleft-floor(stepsleft))/stepsleft; %distance into the
last pixel
            I7remlastpx=I7rem*(stepsleft-floor(stepsleft))/stepsleft;
            Pdwelllastpx=Pixeldwellrem*(stepsleft-floor(stepsleft))/stepsleft;
            I6(k,j+1)=I6remlastpx;
            I7(k,j+1)=I7remlastpx;
            Pixeldwelltime(k,j+1)=Pdwelllastpx;
            j=j+1;
          end; %if allmotorpositions(k,i)>(j+1)*stepsize
        end; %i=1
      end; %if allmotorpositins <j*stepsize
   end; %for i=1:Ind(k)
end; %for k=1:Rows
%I6=flipud(fliplr(I6)); %Invert rows and columns to match photo. We could also reverse
in the save labview code, or rotate motors.
%I7=flipud(fliplr(I7)); %Invert rows and columns to match photo.
%Pixeldwelltime=flipud(fliplr(Pixeldwelltime));
I6=rot90(I6,3); %Rotate rows and columns 270 degrees (90 * 3) to match photo. We
could also reverse in the save labview code, or rotate motors.
I7=rot90(I7,3); %Rotate rows and columns to match photo.
Pixeldwelltime=rot90(Pixeldwelltime,3);

 I6t=I6./Pixeldwelltime*1000;  %counts/ms
I6t(isnan(I6t))=0;
I7t=I7./Pixeldwelltime*1000;    %counts/ms
I7t(isnan(I7t))=0;

figure; imagescp(I6t,0.01,0.99); colorbar; axis('equal', 'tight');
figure; imagescp(I7t,0.01,0.99); colorbar; axis('equal', 'tight');
if nargin<9,
   if nargin == 6, Cp=bg6;
   else
      Cp=0.5 %cutoff percentile assume that intensities above this percentile are data, and
below are background.
   end;
   s6=sort(I6t(:));
   s7=sort(I7t(:));
   bg6=s6(floor(size(s6,1)*Cp*.5))
   bg7=s7(floor(size(s7,1)*Cp*.5))
   thr6=s6(floor(size(s6,1)*Cp))
   thr7=s7(floor(size(s7,1)*Cp))
end;
```

```
R=Ratio(I6t,I7t, bg6, bg7, thr6, thr7); colorbar; axis('equal', 'tight');
```

Appendix B

Permission requested for reproduction of the materials

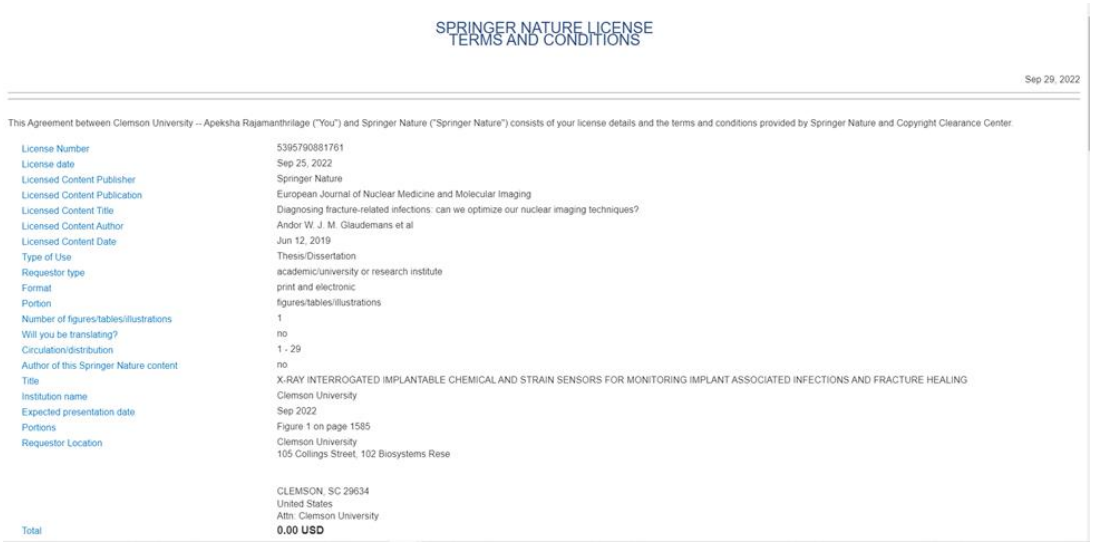

SPRINGER NATURE LICENSE
TERMS AND CONDITIONS

Sep 29, 2022

This Agreement between Clemson University -- Apeksha Rajamanthrilage ("You") and Springer Nature ("Springer Nature") consists of your license details and the terms and conditions provided by Springer Nature and Copyright Clearance Center.

License Number	5395790881761
License date	Sep 25, 2022
Licensed Content Publisher	Springer Nature
Licensed Content Publication	European Journal of Nuclear Medicine and Molecular Imaging
Licensed Content Title	Diagnosing fracture-related infections: can we optimize our nuclear imaging techniques?
Licensed Content Author	Andor W. J. M. Glaudemans et al
Licensed Content Date	Jun 12, 2019
Type of Use	Thesis/Dissertation
Requestor type	academic/university or research institute
Format	print and electronic
Portion	figures/tables/illustrations
Number of figures/tables/illustrations	1
Will you be translating?	no
Circulation/distribution	1 - 29
Author of this Springer Nature content	no
Title	X-RAY INTERROGATED IMPLANTABLE CHEMICAL AND STRAIN SENSORS FOR MONITORING IMPLANT ASSOCIATED INFECTIONS AND FRACTURE HEALING
Institution name	Clemson University
Expected presentation date	Sep 2022
Portions	Figure 1 on page 1585
Requestor Location	Clemson University 105 Collings Street, 102 Biosystems Rese CLEMSON, SC 29634 United States Attn: Clemson University
Total	**0.00 USD**

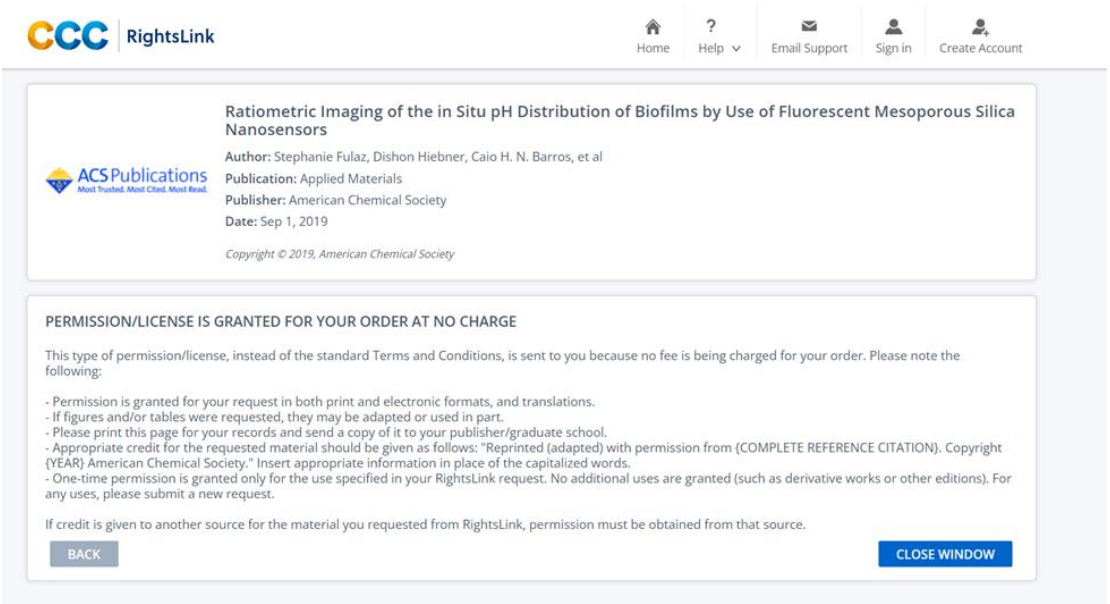

CCC RightsLink

Home | Help | Email Support | Sign in | Create Account

ACS Publications
Most Trusted. Most Cited. Most Read.

Ratiometric Imaging of the in Situ pH Distribution of Biofilms by Use of Fluorescent Mesoporous Silica Nanosensors

Author: Stephanie Fulaz, Dishon Hiebner, Caio H. N. Barros, et al
Publication: Applied Materials
Publisher: American Chemical Society
Date: Sep 1, 2019

Copyright © 2019, American Chemical Society

PERMISSION/LICENSE IS GRANTED FOR YOUR ORDER AT NO CHARGE

This type of permission/license, instead of the standard Terms and Conditions, is sent to you because no fee is being charged for your order. Please note the following:

- Permission is granted for your request in both print and electronic formats, and translations.
- If figures and/or tables were requested, they may be adapted or used in part.
- Please print this page for your records and send a copy of it to your publisher/graduate school.
- Appropriate credit for the requested material should be given as follows: "Reprinted (adapted) with permission from {COMPLETE REFERENCE CITATION}. Copyright {YEAR} American Chemical Society." Insert appropriate information in place of the capitalized words.
- One-time permission is granted only for the use specified in your RightsLink request. No additional uses are granted (such as derivative works or other editions). For any uses, please submit a new request.

If credit is given to another source for the material you requested from RightsLink, permission must be obtained from that source.

BACK CLOSE WINDOW

SPRINGER NATURE LICENSE
TERMS AND CONDITIONS

Sep 29, 2022

This Agreement between Clemson University -- Apeksha Rajamanthrilage ("You") and Springer Nature ("Springer Nature") consists of your license details and the terms and conditions provided by Springer Nature and Copyright Clearance Center.

License Number	5398251184369
License date	Sep 29, 2022
Licensed Content Publisher	Springer Nature
Licensed Content Publication	Photochemical & Photobiological Sciences
Licensed Content Title	In vivo absorption and scattering spectroscopy of biological tissues
Licensed Content Author	Paola Taroni et al
Licensed Content Date	Feb 1, 2003
Type of Use	Thesis/Dissertation
Requestor type	academic/university or research institute
Format	print and electronic
Portion	figures/tables/illustrations
Number of figures/tables/illustrations	2
Will you be translating?	no
Circulation/distribution	500 - 999
Author of this Springer Nature content	no
Title	X-RAY INTERROGATED IMPLANTABLE CHEMICAL AND STRAIN SENSORS FOR MONITORING IMPLANT ASSOCIATED INFECTIONS AND FRACTURE HEALING
Institution name	Clemson University
Expected presentation date	Sep 2022
Portions	Figures 4 & 5
Requestor Location	Clemson University 105 Collings Street, 102 Biosystems Rese CLEMSON, SC 29634 United States Attn: Clemson University
Total	**0.00 USD**

9/29/22, 2:11 PM Clemson University Mail - Requesting permission to include in the dissertation

CLEMSON UNIVERSITY

Apeksha Rajamanthrilage <apekshr@g.clemson.edu>

Requesting permission to include in the dissertation

9 messages

Apeksha Rajamanthrilage <apekshr@g.clemson.edu> Sun, Sep 25, 2022 at 2:47 AM
To: Amit Krishnan <amit.krishnan@jove.com>

Hi Dr. Amit,

I would like to know whether I will be able to use material in our article "High Spatial Resolution Chemical Imaging of Implant-Associated Infections with X-ray Excited Luminescence Chemical Imaging through Tissue" in my dissertation. Please let me know.

Thank you
Apeksha Rajamanthrilage

Amit Krishnan <amit.krishnan@jove.com> Mon, Sep 26, 2022 at 8:25 AM
To: Apeksha Rajamanthrilage <apekshr@g.clemson.edu>

Dear Apeksha,
Thank you for your email.

Please consider this explicit permission to reuse the JoVE content in your dissertation.

Please let me know if you have any questions.

Regards,
Amit
Amit G Krishnan, Ph.D.
Review Editor
JoVE
617.674.1888
Follow us: Facebook | Twitter | LinkedIn
About JoVE

[Quoted text hidden]

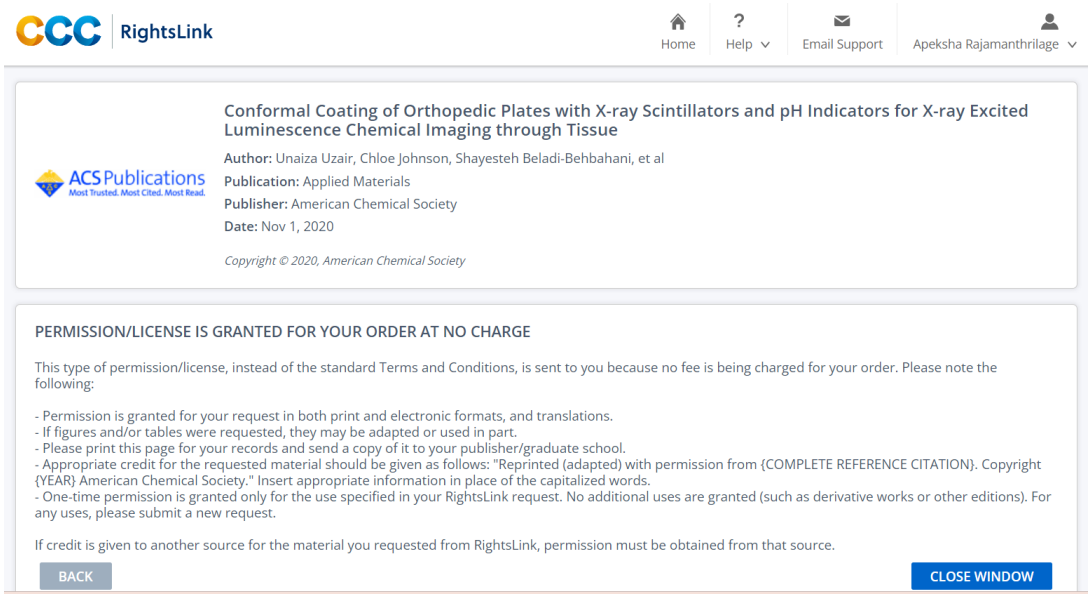

RightsLink

Home | Help | Email Support | Apeksha Rajamanthrilage

ACS Publications
Most Trusted. Most Cited. Most Read.

Conformal Coating of Orthopedic Plates with X-ray Scintillators and pH Indicators for X-ray Excited Luminescence Chemical Imaging through Tissue

Author: Unaiza Uzair, Chloe Johnson, Shayesteh Beladi-Behbahani, et al
Publication: Applied Materials
Publisher: American Chemical Society
Date: Nov 1, 2020

Copyright © 2020, American Chemical Society

PERMISSION/LICENSE IS GRANTED FOR YOUR ORDER AT NO CHARGE

This type of permission/license, instead of the standard Terms and Conditions, is sent to you because no fee is being charged for your order. Please note the following:

- Permission is granted for your request in both print and electronic formats, and translations.
- If figures and/or tables were requested, they may be adapted or used in part.
- Please print this page for your records and send a copy of it to your publisher/graduate school.
- Appropriate credit for the requested material should be given as follows: "Reprinted (adapted) with permission from {COMPLETE REFERENCE CITATION}. Copyright {YEAR} American Chemical Society." Insert appropriate information in place of the capitalized words.
- One-time permission is granted only for the use specified in your RightsLink request. No additional uses are granted (such as derivative works or other editions). For any uses, please submit a new request.

If credit is given to another source for the material you requested from RightsLink, permission must be obtained from that source.

BACK | CLOSE WINDOW

6/28/22, 6:03 PM Clemson University Mail - Requesting permission for including in the thesis

CLEMSON UNIVERSITY

Apeksha Rajamanthrilage <apekshr@g.clemson.edu>

Requesting permission for including in the thesis
2 messages

Apeksha Rajamanthrilage <apekshr@g.clemson.edu> Thu, Mar 10, 2022 at 2:16 PM
To: sidky@uchicago.edu

Dear Editor,

I am Apeksha Rajamanthrialge, a graduate student who has published in your IEEE TBME journal. I was wondering whether I need to request your permission to include the published material in the paper in my dissertation.

Thank you
Apeksha Rajamanthrilage

Emil Sidky <sidky@uchicago.edu> Thu, Mar 10, 2022 at 8:01 PM
To: Apeksha Rajamanthrilage <apekshr@g.clemson.edu>

Dear Apeksha,
You can go ahead and use the material from your TBME article in your thesis.
Thanks for checking!
Best,
Emil

From: Apeksha Rajamanthrilage <apekshr@g.clemson.edu>
Sent: Thursday, March 10, 2022 1:16 PM
To: Emil Sidky <sidky@uchicago.edu>
Subject: Requesting permission for including in the thesis

[Quoted text hidden]